Development of a Wall Climbing Robot and Ground Penetrating Radar System for Non-Destructive Testing of Vertical Safety Critical Concrete Structures

MD Omar Faruq Howlader

London South Bank University

London South Bank University

August, 2016

This thesis is submitted for the degree of Doctor of Philosophy

Abstract

This research aims to develop a unique adhesion mechanism for wall climbing robot to automate the technology of non-destructive testing (NDT) of large safety critical reinforced concrete structures such as nuclear power plants, bridge columns, dams etc. This research work investigates the effect of key design parameters involved in optimizing the adhesion force achieved from rare earth neodymium magnets. In order to penetrate a nominal concrete cover to achieve magnetic coupling with buried rebar and generate high enough adhesion force by using minimum number of permanent magnets, criteria such as distance between multiple magnets, thickness of flux concentrator are evaluated by implementing finite element analysis (FEA).

The proposed adhesion module consists of three N42 grade neodymium magnets arranged in a unique arrangement on a flux concentrator called yoke. The preliminary FEA results suggest that, using two yoke modules with minimum distance between them generate 82 N higher adhesion force compared to a single module system with higher force-to-weight ratio of 4.36. Presence of multiple rebars in a dense mesh setting can assist the adhesion module to concentrate the magnetic flux along separate rebars. This extended concentration area has led to higher adhesion force of 135.73 N as well as enabling the robot to take turns. Results suggest that, having a 50×50 mm rebar meshing can sustain steep robot rotational movement along it's centre of gravity where the adhesion force can fall as low as 150 N. A small, mobile prototype robot with on-board force sensor is built that exhibited 360^0 of manoeuvrability on a 50×50 mm meshed rebars test rig with maximum adhesion force of 108 N at 35 mm air gap. Both experiment and simulation

results prove that the magnetic adhesion mechanism can generate efficient adhesion force for the climbing robot to operate on vertical reinforced concrete structures.

In terms of the NDT sensor, an in-depth analysis of the ground penetrating radar (GPR) is carried out to develop a low cost operational laboratory prototype. A one-dimensional numerical framework based on finite difference time domain (FDTD) method is developed to model response behaviour of a GPR. The effects of electrical properties such as dielectric constant, conductivity of the media are evaluated. A Gaussian shaped pulse is used as source which propagates through the 1D array grid, and the pulse interactions at different media interfaces are investigated. A real life application of GPR to detect a buried steel bar in 1 m thick concrete block is modelled, and the results present 100% accurate detection of the steel bar along with measured depth of the concrete cover. The developed framework could be implemented to model multi-layer dielectric blocks with detection capability of various buried objects. Experimental models are built by utilizing a proposed antenna miniaturization technique of dipole antenna with additional radiating arms. The resultant reflection coefficient values indicate a reduction of 55% and 44% in length reduction compared to a conventional 100 MHz and 200 MHz dipole antenna respectively. The GPR transmitting pulse generator features an enhanced tuneable feature to make the GPR system more adaptable to various environmental conditions. The prototype pulse generator circuit can produce pulses with variable width from 750 ps to 10 ns. The final assembled robotic GPR system's performance is validated by its capability of detecting and localizing an aluminium sheet and a rebar of 12 mm diameter buried under a test rig built of wood to mimic the concrete structure environment. The final calculations reveal a depth error of +0.1 m. However, the key focus of this work is to prove the design concept and the error in measurement can be addressed by utilizing narrower bandwidth pulse that the proposed pulse generator is capable of generating. In general, the proposed robotic GPR system developed in this research proves the concept of feasibility of undertaking inspection procedure on large concrete structures in hazardous environments that may not be accessible to human inspectors.

Table of contents

List of figures

List of tables

Glossary of abbreviations

ABC	Absorbing Boundary Condition
ADC	Analogue-to-Digital Converter
BINDT	British Institute of Non-Destructive Testing
BJT	Bipolar Junction Transistor
DoF	Degrees of Freedom
ECL	Emitter Coupled Logic
EM	Electromagnetic
FBTA	Folded Bow-Tie Antenna
FDTD	Finite Difference Time Domain
FEA	Finite Element Analysis
FEM	Finite Element Method
FFT	Fast Fourier Transform
FWHM	Full Width Half Maximum
GPR	Ground Penetrating Radar
LNA	Low Noise Amplifier
MoM	Method of Moment
NDT	Non Destructive Testing
PDL	Programmable Delay Line
PRF	Pulse Repetition Frequency
PSD	Power Spectral Density
Rebar	Reinforcement bar
Rx	Receiver
SRD	Step Recovery Diode
TF/SF	Total Field/Scattered Field
TNA	Thermal Neutron Activation
ToF	Time of Flight
TVG	Time Varying Gain
Tx	Transmitter
US	Ultra-Sound
UWB	Ultra-Wide Band
VCO	Voltage Controlled Oscillator
VSWR	Voltage Standing Wave Ratio

Chapter 1. Introduction

This chapter describes the background and motivations of this research, defines the aims and objectives, contributions to knowledge. The chapter is organized as follows:

1.1 Overview

This research is directed at developing a reinforced concrete surface climbing robot with on-board ground penetrating radar (GPR) to carry out non-destructive testing (NDT) of vertical safety critical concrete structures. The research emphasizes on investigating techniques of developing a novel permanent magnet based adhesion mechanism for reinforced concrete wall climbing robots. NDT techniques have found their application in the regular inspection of large safety critical infrastructures to determine the structural integrity and planned maintenance schedules. The fields of application reach from large fixed welded structures such as oil storage tanks, ship hulls to petrochemical and food processing industry [1]. Meanwhile, many of the other safety critical structures such as cooling towers of power plants, bridge columns, dams, complex nuclear power plants etc. are constructed using concrete. Even though concrete can offer higher strength and durability compared to other building materials [2], atmospheric moisture and chlorides cause the concrete structures to lose their strength. To avoid total structural damage, an extensive structural assessment must be carried out. Therefore, from a civil engineering perspective, NDT plays a critical role in detecting induced structural faults like reinforcement bar corrosion, cracking, and delamination of the concrete surface [3].

1.2 Rationale of the research

Considering the critical impact that NDT methods have in determining the structural integrity and planned maintenance schedules, there is a serious issue about the efficiency of present methods of carrying out NDT process. Currently, the deployment of NDT in concrete structure scenario is mostly manual and the primary challenge of carrying out the procedure on a vertical concrete structure is to gain access to the inspection area which is normally located at a high altitude. This current practice has major drawbacks. Firstly, before carrying out the intended inspection process, the operators have to meet the terms of numerous health and safety regulations laid out by the governmental bodies to deploy temporary platform to gain access to the target area [4]. Moreover, operators deal with hazardous environments such as nuclear or chemical industrial environments, working at high altitude, heavy workload, and limited manoeuvrability [5]. This is a complex and time-consuming process and more often the cost of gaining access is greater than the cost of performing the actual NDT.

The challenges faced by the current process of carrying out NDT of vertical concrete structures must be addressed by ensuring both public safety measurements and high resource efficiency. Considering the limiting factors of manual NDT process, the process can be improved by implementing automated robotic systems and as a result, climbing robots in the field of vertical structures are of increasing importance for inspections and maintenance tasks. Until now, a considerable amount of research has been devoted to developing various types of experimental models and application of special climbing robots has been seen in fields such as steel oil tank inspection, weld line inspection, steel pipe structure inspection, and rescue operations [6]. However, the desired tasks and field of application mostly dictate the design aspects of climbing robots.

1.2.1 Current practice of climbing

The current practice in carrying out NDT of safety critical vertical structure is manual and the biggest task is easier accessibility as mentioned earlier. Access to test sites on these structures is mostly obtained by constructing scaffolding. The scaffoldings used are of two main types, fixed type or abseiling type. A fixed type scaffolding can offer stable access of the target area to the NDT operator, however, this type of scaffolding is expensive and time consuming to erect and disassemble. The abseiling type is most commonly used for inspection purposes and less complex than its fixed counterpart. But they are more vulnerable to wind gusts and bad weather. Figure 1-1 shows a scenario of manual NDT of a 192 m concrete cooling tower, which confirms the complexity of erecting fixed scaffolding around the structure [7].

Figure 1-1. Manual NDT of tall concrete cooling tower by eracting scaffolding [7].

However, for more complex structures such as bridge columns, decks, and concrete storage tanks etc. scaffolding is not a feasible option. In those cases, access devices like cranes and gondolas are deployed to the desired position as shown in Figure 1-2.

Sometimes professional climbers, called ‘spider workers’ are involved in the process if the structure cannot be accessed otherwise [8].

Figure 1-2. Access devices used for vertical structure inspection [8].

Other than the complexity, safety of the NDT operators and the cost of preparations are the two main issues that must be considered. Here the operators deal with hazardous working environments with limited manoeuvrability [9]. More often than not, it’s the environment that causes the most concern than the altitude. In the nuclear industry for example, the spider-workers are exposed to radioactive air while inspecting concrete reactor tanks. Even though the nuclear regulatory commission determined 50 mSv of radiation exposure in a year as a safe limit [10], it is the cyclic exposure to radiation that proves fatal. In 2015, a report in the British Medical Journal stated that, a total of 17, 957 workers in the nuclear industry from France, the United Kingdom, and the United States died from solid cancers caused by low level but cyclic radioactive exposure in the last 72 years [11].

Likewise, in the chemical industry, the operators have to deal with high temperature as a boiler tube is shut down for inspection, it requires 2-3 days before it reaches a safe level [12]. Figure 1-3 illustrates the process of a petroleum storage tank inspection using rope technique. The freedom of movement and speed of mobility is very much restricted in these discussed scenarios that the end result of the NDT inspection is of poor quality.

Figure 1-3. Petrolium storage tank inspection using abseiling technique [12].

Therefore, the interest in the development of climbing robots has grown significantly as robotic solutions can offer reliable performance, increased operational efficiency, reduced cost and greater health and safety protection to the human operators.

1.2.2 NDT metods for safety critical structures

NDT methods clearly have a role in the evaluation and testing of civil engineering structures, particularly in the site investigation process for construction. Many of the methods that are widely used in the NDT of civil engineering structures are also used in applications such as geophysics and archaeology due to having the same physical parameters that control the effective use of inspection methods [13]. Variations in NDT techniques are based on different theoretical principles and they produce different sets of information regarding the physical properties of the structure such as compressional and shear wave velocities, electrical resistivity etc. Furthermore, reliability of a particular NDT method depends upon the physical properties of the construction materials. The most prominent and sophisticated methods that provide easier, effective and economical alternatives are discussed in the following sections.

1.2.2.1 Ultrasonic pulse velocity method

The sonic method refers to the transmission and reflection of mechanical stress waves through a medium at sonic and ultrasonic frequencies and have been used for the past thirty years in the assessment of civil engineering structures and materials [14]. The impact-echo test method is the most recent development of this technique that can be used to measure concrete thickness and integrity from one surface. The method is performed by hitting the surface of a structure at a given point and recording the reflected energy with an accelerometer mounted adjacent to the impact location. A small instrumented impulse hammer is used for hitting and the recorded time domain signal is converted to frequency domain by using a fast fourier transform (FFT) algorithm [15]. The reflected signals from the back wall and voids are easily identifiable in the frequency domain as can be seen in Figure 1-4. The focus of impact-echo testing is centred on identifying voids in ducts of post-tensioned concrete such as finite element analysis (FEA) of a laboratory experiment at the University of Edinburgh showed that defects can be identified provided a sufficiently high frequency is used [16].

Another form of sonic method implements ultrasonic pulses generated by a piezoelectric transducer at frequencies above 20 kHz. The rebound stress level of the primary pulse is measured by a receiver and the total travel time is determined. For a known length of concrete surface, the velocity of the pulse wave is measured which is

always a constant. A reduced value of pulse velocity verifies the presence of faults on the concrete surface and this form of testing is used successfully at ultrasonic frequencies for the detection of flaws in metal castings and concrete [17]. With the more advanced model of ultrasound testing, probes are connected individually in a phased array configuration. The focal point and angle of the sound source from each probe can be individually modified for rapid scanning of larger area [18].

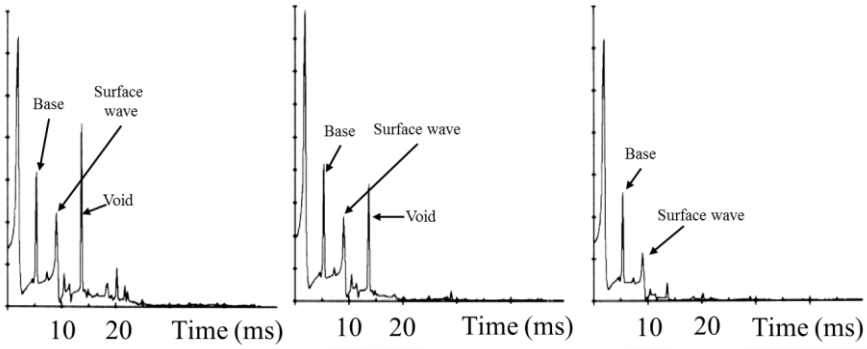

Figure 1-4. Frequency domian spectrum of a impect-eco signal [15].

However, the efficient application of ultrasonic technologies is limited by the fact that ultrasonic probes require effective coupling agent, such as grease or petroleum jelly, to temporarily adhere the transmitter and receiver to the surface [19]. As a result, the inspection process becomes slow and achieving sufficient coupling on uneven surfaces sometimes becomes troublesome. Besides, scattering of the wave due to material heterogeneity limits the propagation through the material. This makes it difficult to differentiate defects amongst the noise. Nonetheless, ultrasound systems are typically lightweight and are well adoptable to robotic applications and therefore, further developments in signal generation, detection and data processing may lead to a practical tool once the limitations mentioned above are overcome.

1.2.2.2 Infra-red thermography

The process of infra-red thermography involves converting the heat at any temperature into a thermal image using specialised scanning cameras. It has been observed that, a concrete surface without any defects appears quite uniform in infra-red camera. However, with any cracks or delamination within the concrete the surface retains more heat than uniform surface under solar irradiation. The areas with irregular variance of heat are observed as hot spots in the thermal record. This method has proved to be most effective for the rapid assessment of large buildings particularly high rise apartment blocks that offer close examination on the structure for identification and future investigation [20]. For the inspection of composite structures, thermography has

an advantage over ultrasound as ultrasound is a point-to-point testing system while thermal imaging can cover a larger area in a single viewpoint. Moreover, as composite structures are made of two adjacent layers with a small air gap between them, the application of ultrasonic inspection is limited in this case as ultrasound cannot travel through air without any coupling [19].

1.2.2.3 Radiography

More advanced and complex NDT methods involve very short wavelength electromagnetic (EM) radiation such as x-rays, gamma-rays or neutron rays that can penetrate through solid media [21]. While propagating, a portion of the wave energy is absorbed depending on the density and thickness of the medium of propagation. Radiography is capable of detecting any feature in a material that has sufficient differences in thickness and density within the test piece provided. The success rate of radiography relies on void size as large voids are more readily detected than smaller ones. However, the radiographic methods require protective shielding for safe application and also high payload capacity. Therefore, these technologies are not feasible for robotic automation.

1.2.2.4 Concrete cover meter

Concrete cover meter is an EM system that can determine the location and thickness of the steel reinforcement bars (rebars) embedded in the concrete. The cover meter consists of two coils positioned on an iron-cored inductor that detects the presence of the rebar within the concrete by measuring the variation of the electromagnetic field within the inductors. The relationship between the induced current and the thickness of the concrete is non-linear. The diameter of the rebar also has an effect on the induced current. Moreover, the presence of saline water in the concrete increases the electrical conductivity above the rebers that can cause inaccuracy in the measurements. Modern cover meters are designed and calibrated to mitigate this non-linearity and with careful application, excellent results can be achieved. More recent and specialised cover meters can measure the diameter of the rebars using a calibrated model [22].

1.2.2.5 Ground penetrating radar

GPR is an EM technique based on the propagation, reflection and scattering of high frequency (10MHz–2.5GHz) waves in the subsurface. High resolution imaging of shallow subsurface can be achieved by using GPR. GPR’s non-invasive technique to identify and classify subsurface features have been implemented in application fields such as oil and gas exploration, buried pipeline localization [23], locating potential

buried hazards such as mine shafts and voids in the mining industry [24], [25], investigating Glaciers structure and formation [26], investigating geological sites [27]. GPR operation can be categorized into two main modes: (1) time-of-flight (ToF) based surveying where the transmitter and receiver antennas are located on the surface of the earth, and the imaging is done based on changes in electrical properties of the subsurface layers, and (2) borehole surveying, where one or both antennas are located in boreholes, and topographical subsurface properties are estimated [28]. A key performance factor of any GPR application is the penetration depth achieved or the lack of it which depends on the electrical characteristics of the object and of the material in which the object is buried.

A higher frequency GPR system emits narrower pulses in picosecond region, yielding a higher time and depth resolution. However, the depth penetration of high frequency signal is low as signal attenuation increases with frequency [29]. Whereas a low frequency system has a lower depth resolution but higher depth penetration as given in Table 1-1 [30]. Moreover, high frequency GPR can be best implemented in dry subsurface sand, gravel and pit, but, the presence of moisture in the media can cause minor signal attenuation. As in [31], severe signal attenuation problems were found in slit, clay with moist saline conditions. Therefore, low frequency (< 500 MHz) GPR systems are ideally suited for outdoor geotechnical, archaeological and environmental applications where moisture is a regular occurrence and high depth penetration is highly desired.

Table 1-1. Depth penetration and resolution of GPR with different frequencies [30].

Antenna frequency (MHz)	**Resolution (m)**	**Penetration depth (m)**	**Blind zone (m)**
300	1	7 – 10	0.5 – 1.0
500	0.5	7 – 10	0.25 – 0.5
900	0.2	3 – 5	0.1 – 0.2
2000	0.04 – 0.08	1.5 – 2	0.06

Table 1-2 illustrates a summary of comparison between available state-of-the art NDT technologies. Considering all the evidences, GPR provides easier and accurate subsurface mapping of concrete structures and most suited to robotic applications. Therefore, detailed investigation of GPR technology including numerical modelling of GPR and hardware design are carried out in this research.

Table 1-2. Comparison of different NDT methods for concrete structures.

Inspection method	Parameter measured	Advantages	Disadvantages	Cost
Visual	Outer surface condition	Quick, superficial inspection	Not thorough	Low
Sonics	Wave velocity	Provides information on major elements such as cracks, voids	Moderately slow	Moderate
Ultrasonic NDT	Wave propagation through structure	Detects voids, measure material thickness	Slow, point-to-point system	Moderately high
Cover-meter	Electrical induction	Quick measurement of concrete cover and rebar detection	Less accurate in outdoor scenarios	Low
GPR	EM wave velocity	Good depth penetration and resolution, provides subsurface mapping	Requires skill to interpret data	High

1.3 Aims and objectives

The focus of this research is to mitigate the challenges set out by the traditional NDT method. The proposed solution will ensure both public safety measurements and high resource efficiency. The design of climbing robots depends on the application field. However, the primary common requirement of all climbing robots is the need to maintain secure and sufficient attachment to the climbing surface. An adhesion mechanism that does not meet this requirement can cause the robot to slip or roll-over. Moreover, adhesion mechanism with low energy consumption can pave the way to a compact and lightweight robotic system. This feature may allow an on-board power system or a thinner and lighter umbilical power cable to be used for off-board power. Moreover, GPR as an emerging NDT method can provide in-depth inspection of concrete subsurface.

Considering all the design constrains and facilities available, the overall aims of this research are as follows:

- Design and develop a novel permanent magnet based adhesion mechanism for reinforced concrete climbing robot.
- Design and develop a low-cost GPR hardware to be incorporated with the climbing robot to carry out NDT.

The individual objectives required to achieve the research aims include:

- Investigate the properties and flux concentration techniques of rare earth magnets. This investigation will identify the practicability and technique of implementing the permanent magnets as the means of adhesion for the wall climbing robot on concrete surface. The main challenge when adhering to a concrete surface using permanent magnets is to concentrate and magnify the magnetic flux to flow into the concrete as deeply as possible to couple with rebars buried under the concrete. This study is carried out by using FEA suite 'Comsol Multiphysics'.
- Study the construction methods of concrete structures according to industrial standards such as Eurocode 2 and the British standard BS850. This study will provide clear understanding of buried rebars arrangements and determine the minimum concrete cover of various structures. These results can help to determine the design parameters of the adhesion module.
- Implement finite difference time domain (FDTD) method of numerical modelling to develop a universal framework of GPR signal response in complex media such as nonhomogeneous, lossy, dispersive and non-linear media.
- Investigate GPR hardware system to design miniaturized antennas and improve portability of low frequency GPR system. A reduction in antenna length can significantly make the system mountable on a mobile robot.

1.4 Research contribution

The main contribution to knowledge arising from this research is a novel adhesion mechanism. A permanent magnet based mechanism is proposed here. Permanent magnet based systems have already been implemented in developing climbing robots for ferrous surfaces. However, the arrangements of permanent magnets on a flux concentrator in a unique technique makes this mechanism applicable for reinforced concrete environment. The prototype robot exhibits significant advancement in climbing robot technology as this proposed mechanism is the first of its kind to be reported in the literature. A systematic study of the magnetic system identifies different parameters affecting the resultant adhesion force.

Another major contribution made is the development of a universal numerical framework of GPR using FDTD method. A considerable amount of research has been

devoted to FDTD for material dispersion behaviour, complex geometrical shapes, and antenna design. However, most of those works are limited to specific media and their behaviour with very specific problem dimensions. Also, many of those only emphasise on the obtained results rather than comprehensive discussion of the algorithm. This research breaks down the building block of the FDTD algorithm and proposes a framework for collective application of the system. Here only one framework can be implemented to model a variety of media by alternating the electric and magnetic property variables in the framework. This can help researchers simplify their research questions and gather data from a wide range of materials and media. Moreover, results acquired from this framework can provide an overview of the total problem scenario of real life GPR application. These results are vital to establish the responses expected from the physical GPR application. Furthermore, the subsequent stages of designing an antenna and transceiver system for the GPR could be fine-tuned for better accuracy by following those results.

Furthermore, better portability and feasibility of combining with robot have been achieved in this research by investigating GPR antenna technology. A technique of implementing additional radiating arms with primary dipole antenna described in this research has reported a 55% reduction in antenna length compared to a conventional dipole antenna of same resonant frequency.

All the major contributions of this research have been reported in scholarly publications listed below:

Book chapter

1. M. O. Howlader and T. P. Sattar, “Design and Optimization of Permanent Magnet Based Adhesion Module for Reinforced Concrete Surface Climbing Robots,” in Intelligent Systems and Applications, vol. 650, pp. 153-171, Springer Link, 2016.

Journal papers:

1. M. O. Howlader and T. P Sattar, “Miniaturization of Dipole Antenna for Low Frequency Ground Penetrating Radar,” Progress In Electromagnetics Research C (PIER C), vol. 61, pp. 161-170, 2016.
2. M. O. Howlader and T. P. Sattar, “Finite Element Analysis Based Optimization of Magnetic Adhesion Module for Concrete Wall Climbing

Robot," International Journal of Advanced Computer Science and Applications (IJACSA), vol. 6, no. 8, pp. 8-18, 2015.

3. M. O. Howlader and T. P. Sattar, "FDTD Based Numerical Framework for Ground Penetrating Radar Simulation," Progress In Electromagnetics Research M (PIER M), vol. 44, pp. 127-138, 2015.

Conference papers:

1. M. O. Howlader, T. P. Sattar and S. Dudley, "Development of a Wall Climbing Robotic Ground Penetrating Radar System for Inspection of Vertical Concrete Structures," in 18th International Conference on Control, Dynamic Systems, and Robotics, Amsterdam, The Netherlands, 2016.
2. M. O. Howlader and T. P. Sattar, "Miniaturized Dipole Antenna Development for Low Frequency Ground Penetrating Radar (GPR) System," in 4th IET Colloquium on Antennas, Wireless and Electromagnetics, Glasgow, UK, 2016.
3. T. P. Sattar, P. Hilton and M. O. Howlader, "Deployment of Laser Cutting Head with Wall Climbing Robot for Nuclear Decommissioning", in 19th International Conference on Climbing and Walking Robots and Support Technologies for Mobile Machines (CLAWAR), London, UK, 2016.
4. M. O. Howlader and T. P. Sattar, "Novel Adhesion Mechanism and Design Parameters for Concrete Wall-Climbing Robot," in SAI Intelligent Systems Conference, London, UK, 2015.
5. M. O. Howlader and T. P. Sattar, "Development of Magnetic Adhesion Based Climbing Robot for Non-Destructive Testing," in 7th Computer Science & Electronic Engineering Conference, Essex, UK, 2015.

1.5 Thesis outline

This thesis consists of nine chapters including the introduction in this chapter. The remainder layout of the thesis is as follows:

Chapter 2 presents a design review of wall climbing robots. The review is carried out from robot locomotion and adhesion mechanism point of view. It also discusses design of robots based on biological model. The chapter concludes with a comparison between those designs and their limitations.

Chapter 3 discusses the design parameters that affect the adhesion force achievable from the proposed mechanism. This chapter looks into the effects of distance between magnets, magnets arrangement layout etc. using FEA based parametric studies.

Chapter 4 validates the results obtained from the FEA simulations experimentally. The development of a prototype climbing robot with on-board force measurement unit is presented. The design of an experimental rig that emulates rebars buried under concrete is also discussed here that demonstrates manoeuvring capability of the robot on a vertical surface.

Chapter 5 contains the theory and operation of GPR. It explains important terminologies as well as elements of a GPR system. This chapter also reviews the existing robotic GPR systems and identifies the gap in the field of application.

Chapter 6 describes the background of FDTD algorithm. A numerical framework of GPR simulation is developed in this chapter. The building blocks and components of the framework are discussed in detail.

Chapter 7 presents the development process of a low frequency GPR hardware. This highlights the method of designing a low-cost pulse generator built from off the shelve components. Moreover, the miniaturization technique of conventional dipole antenna is another section of this chapter. A test rig is used to validate the performance of the climbing robotic GPR module. The chapter proves the design concept and demonstrates rebar detection capability of the GPR at 40 mm depth.

Chapter 8 concludes the thesis with summary of key features achieved in this research. It recommends the optimum design parameters for successful deployment of the robotic GPR platform. This chapter also identifies the potential of future works to advance this research.

1.6 Chapter summary

This chapter has outlined the motivation of this research. The research rationale has been justified by an overview of current practice of climbing process for concrete structure inspection. The chapter has identified the gap in climbing robotic technology and the proposal of integrating GPR technology with climbing robots has made the research aims and objectives a significant prospect of advancement. Finally, this chapter elaborates contributions to knowledge as well as a defined scope of this thesis.

Chapter 2. Design review of climbing robots

In this chapter a design review of climbing robots based on locomotion and adhesion principles is carried out. It sets the design requirements and identifies the limitations of current designs. The chapter is organized as follows:

2.1 Overview

NDT robots are robotic platform of conducting inspection tasks on walls, ceilings, roofs as well as more complex geometric structures such as aircraft wings and wind turbine blade. The climbing platforms are largely deployed in applications where direct access by a human operator is very expensive because of the need for scaffolding. In addition to that, robots can negate the effects of hostile working environments. The main motivations are to increase the operation efficiency by reducing cost and lead time but most importantly, to ensure health and safety aspect in hazardous tasks. Climbing robots have the ability to carry appropriate tools and sensors to scan. However, as the workplace of climbing robots is on the vertical plane they require special adhesion mechanism to carry their payload along the vertical surface. Hence, the most significant criterion for designing a climbing robot is to adopt an appropriate adhesion mechanism for adapting to the given environmental requirements.

In general, design criteria of climbing robots depend significantly on the desired tasks and field of application. Several review studies have been carried out in the field of wall climbing robots [32], [33], [34]. As the field is comprehensively discussed in the literature, it will not be discussed here in detail. This chapter will present a brief review of design aspects related to climbing robots suitable for inspection and maintenance applications. It will compile a classification of climbing robots with considerations of the locomotive and adhesion mechanisms. A comparison between the different technologies and their limitations are presented at the end of this chapter.

2.2 Design requirements

Research in climbing robots has become more intense in the scientific society over the last two decades because of their potential. At the beginning, the developed systems have been implemented to fit exactly one application or object like a steel bridge or a nuclear power plant [35]. Advancements in the technology saw the applications of these robots grow with their ability to handle different surfaces and to perform faster and more accurate navigation. These advancements have been brought about by new locomotion types and adhesion mechanisms during the recent years [6].

Climbing robots as well as other supporting technologies must fulfil certain requirements in order to execute the desired tasks. Even though the requirements and their importance depend on the application type, a general set of requirements can be

suggested suitable for nearly all climbing robots in the range of inspection and maintenance:

- Payload capacity is the most important factor of climbing robot technology as the robot is required to support its own body as well as carry a certain payload while climbing. The payload may vary depending on the application field. For example, impact – echo, cover meter or wenner probe used in concrete inspection are heavy systems and a payload capacity of no less than 10 kg is desired for successful deployment. In contrast, systems equipped with thermal imaging camera can be small and payload capacity of several hundred grams is quite sufficient. Therefore, the dimension of the robot as well as its adhesion and motion components need to be adjusted according to the application.
- System mobility is another factor that decides the ability to move and steer in an acceptable speed on the surface area. The robot should move at a constant speed along the inspection area for thorough inspection but also at higher speed to travel to another inspection area to save time. The British Institute of Non-Destructive Testing (BINDT) recommends an ultrasound NDT scanning speed of 0.7 metre per second for steel surfaces for a 5 MHz ultrasonic probe and this scanning speed can be used as a reference [36]. The positioning capability of the robot may be another desirable feature that includes the precision of locomotion as well as its trajectory. This feature is useful if the inspection equipment such as cover meter need to be moved in a smooth and continuous way over the surface. Moreover, sideward movement and 360^0 turning capability can ensure better positioning of tools and sensors.
- Safety mechanism is an important non-functional design aspect. The robotic system should be agile and robust enough to minimize the damage from any case of failure. Should the robot fall from a height due to adhesion failure, the impact of a heavy robot would cause damage to plant equipment and surroundings. Therefore, there should be a safety mechanism in place in the form of robust hardware, optimal controllers and methods to detect and handle hazardous situations and to recover from them. It all comes down to the mechanical design of the robot to ensure minimum system mass and the use of umbilical cord can be implemented as a safeguard to eliminate the danger of a drop-off.
- Energy consumption can define the efficiency of the climbing robot. To bring a robotic system into application it has to be powerful, more efficient in terms

of adhesion and locomotion. An adhesion mechanism with low or zero energy consumption is always preferable to a higher consumption system. High energy requirement means bigger power supply unit and a failure in that could mean an event of system drop-off from an altitude

In addition to those important factors discussed above, issues like maintainability, easily replaceable faulty parts, faster and less complicated operation are few criteria that outline the design aspects of climbing robot. Based on the desired task, a design trade-off must be sought to select a suitable locomotion and adhesion principle.

2.3 Locomotion principles

A combination of different types of locomotion and adhesion techniques can be found in the literature. The main focus in selecting the correct locomotion principles should be given on the required task and the operation environment. In general, four main distinguishable forms of locomotion principles with respective advantages and drawbacks can be identified in the literature.

2.3.1 Arms and legs

The use of arms or legs is a common locomotion principle that is derived from the biological models of insects or geckos which can climb walls and ceilings [37]. Legged locomotion can have simpler two legged systems to more complex eight-legged one depending on the individual task and different degrees of freedom (DoF) required. The most common adhesion techniques used with legged locomotion are vacuum suction cups, grasping grippers, or magnetic devices that are easier to mount at the end of the feet. The additional number of legs provide increased payload capacity and safety of the system but increase the size and weight of the robot as a consequence [38]. To overcome this problem RAMR 1, a biped robot has been designed that consists of four joints and five links [39]. It uses suction adhesion mechanism at the ends of its legs as shown in Figure 2-1 and weighs only 335 g. Three motors are used to control the hip joint and one ankle joint to navigate the robot on a surface. Presently there are many biped robots with the ability of climbing over surfaces with different slopes [40], [41]. However, the main negative issue with this biped design is the lack of stable movement.

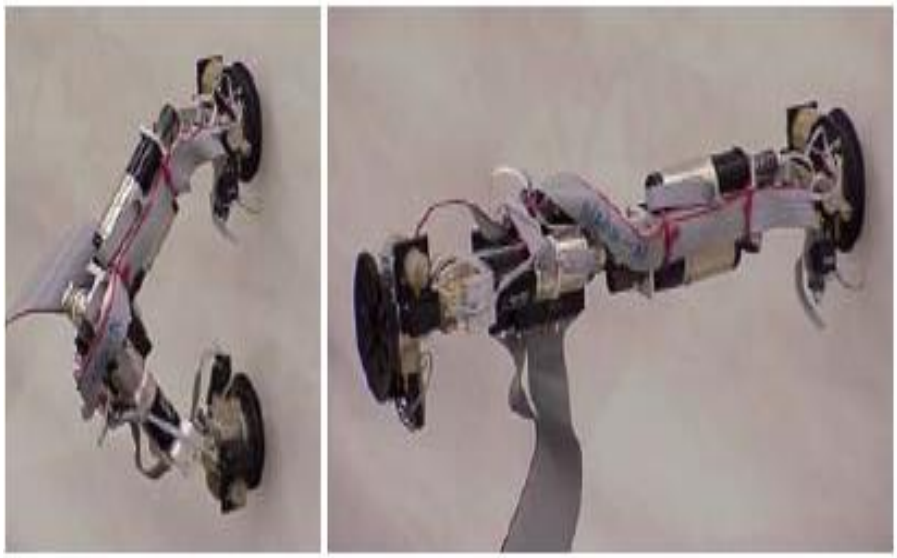

Figure 2-1. Walking procedure of RAMR 1 on a surface [39].

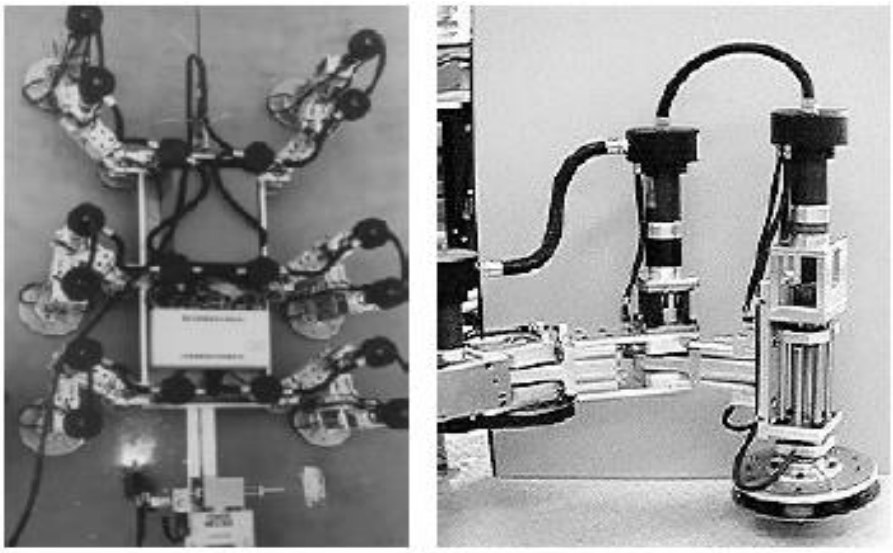

Figure 2-2. REST robot welding a ship hull and its electromagnetic gripper [42].

The REST 1 presented in Figure 2-2 can offer increased stability and payloads by using six reptile type legs. The robot is capable of carrying out inspection, cleaning, and welding tasks of a ship hull with 3 DoF [42]. This robot can climb any ferrous surface using electromagnetic attachment modules attached with its each foot. The total system weighs up to 250 kg and the design trade-off of its highly complex selective compliant leg kinematic operation and the increased stability and payload are the increased size, complexity, and weight.

Arms and leg based locomotion systems can adapt to complex surface structures as well as overcome obstacles due to the folding capacity of their limbs. Moreover, having a lot of degrees of freedom can ensure motion over rough surfaces and transition between surfaces of different planes.

2.3.2 Sliding frames

Sliding frame are common locomotion systems to be used in combination with pneumatic [43], [44] or magnetic [45] adhesive robots to keep the robot attached to the vertical surface. The operating principle of these systems are very simple and involves coordinated movements of two frames in a linear or rotational way against each other. One frame is attached to the surface carrying the entire body weight while the second frame is lifted and moved in the desired direction and the process is repeated for complete movement. Gekko III is a suitable example of such system which implements two planar tracks as the locomotive mechanism and a series of suction cups for attachment to glass walls for cleaning purpose [46]. It can reach a higher speed of 4 ms^{-1} and climb over obstacles as high as 4 cm. Figure 2-3 illustrates a frame walking robot proposed in [47], which consists of one external body that supports the frame for the transport of the body along with an internal body that is connected to the external one by guide rails. The advantage of this specific design is the ability to transverse longitudinally with respect to its centre of the body. While a conventional sliding frame based locomotion can deliver only forward and backward motion, robot SURFY can alter its heading by raising its external body from the surface by using pneumatic actuators while the internal body keeps the robot attached to the surface. This locomotion principle allows easy control of robot motion in combination with safe adhesion since the system can test its adhesion force prior to lifting the external body. Example of the same principle can also be found in [48], [49].

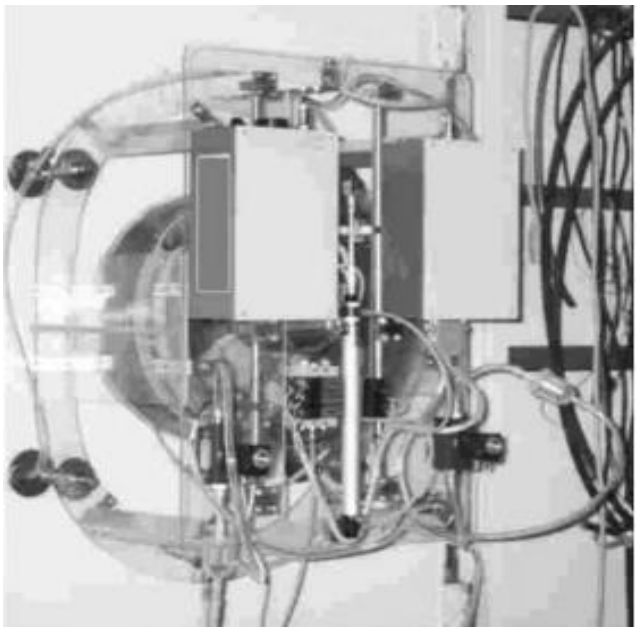

Figure 2-3. Physical structure of SURFY robot [42].

2.3.3 Wheels and tracks

Wheels and track driven locomotion are highly adaptable on relatively smooth terrain with simple and efficient operation. They can produce the highest top speed compared to any other principles discussed above. Wheels can be used as the primary drive along the surface such as in Alicia II [50] and Neptune [51] systems that can drive over obstacles that are small compared to the wheel radius. Alternatively, the wheels and tracks can combine both locomotion and adhesion system in the form of electro-adhesive or sticky tracks, tracks equipped with suction cups [52], [53] or by magnetic wheels [54].

Tracked robots have a similar mechanism as wheels although tracked climbing robots are better at driving over obstacles and adhere to the surface. As they occupy a long flat attraction area between the track and the climbing surface, tracked mechanism can exert higher adhesion force of 80 N. Cleanbot II is a good example of tracked system that can achieve continuous movement. The tracks are equipped with 52 suction cups that transform the tracks to both active locomotion and adhesion module [55]. Another miniature climbing robot, Tripillar [56] has tracks moulded in the form of caterpillars and magnets are fixed to the robot's frame. These caterpillar shape tracks provide the robot a two DoF that can cruise on planar ferromagnetic surfaces at any inclination to gravity. The procedure of surface transition is demonstrated in Figure 2-4.

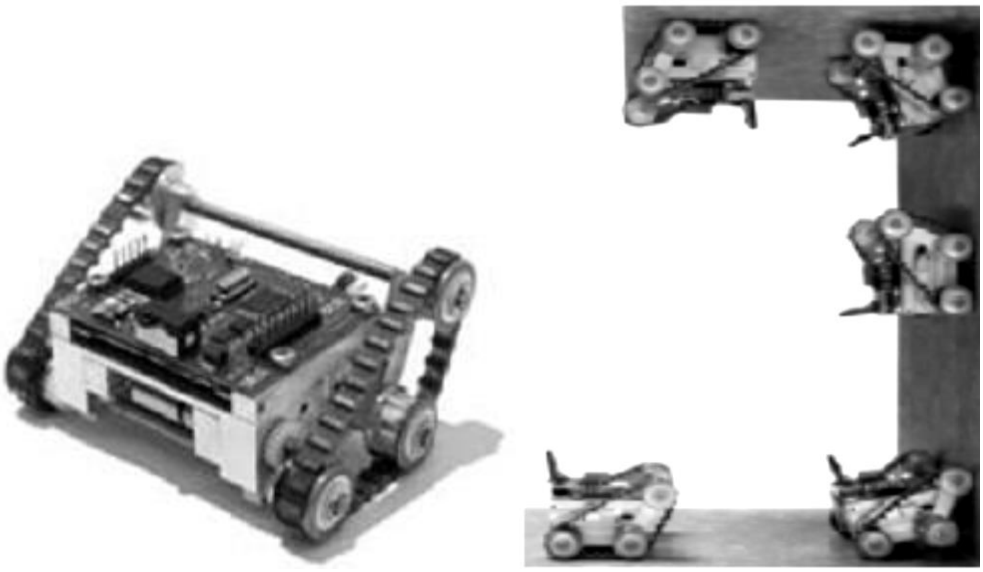

Figure 2-4. Tracked Tripillar robot and its surface transistion procedure [56].

2.3.4 Wires and rails

Wires and rail locomotion for some fixed applications like maintenance and cleaning of tall structures have been used that allow such simpler robot dynamics. A tile-wall robotic system [57] for the NDT of concrete buildings shown in Figure 2-5 is a good example of this category. This system consists of a portable module carrying the NDT devices, the ground and the roof platform connected together by a conveyor belt. The advantage of this mechanism is that the control system only has to position the NDT sensors at the point required and the additional payload is held by the conveyor belts. Even though this system allows much simpler robot dynamics, the system is still ineffective in the case of very tall structures as the conveyor belts need to be installed between the roof and the ground. Application of other wire driven locomotion can be found in [58], [59].

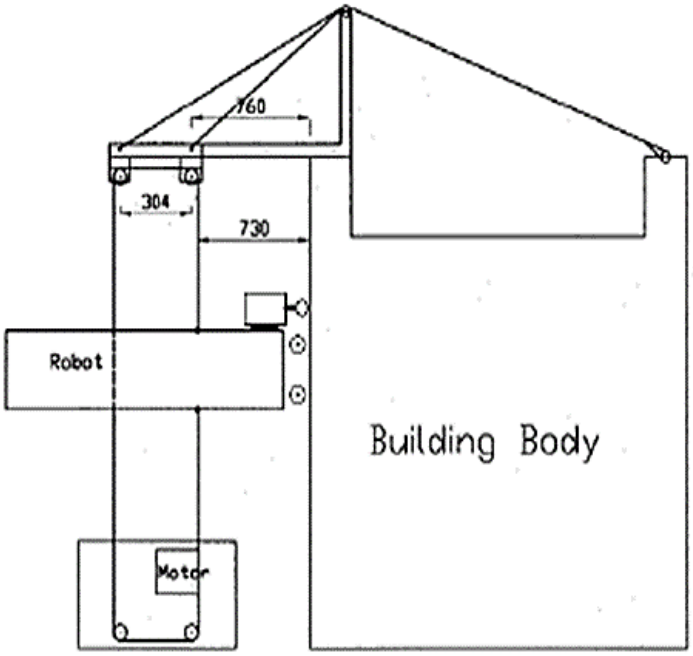

Figure 2-5. Block diagram of the Tile-Wall robot system [57].

2.3.5 Hybrid locomotion

Along with the main categories of locomotion principles discussed above, robotic systems with hybrid locomotion mechanisms exist that combine multiple locomotive mechanisms together to improve the climbing ability depending on the working environment. For instance, Alicia 1 and 2 that adapt two driving wheels to manoeuvre over small obstacles under 1cm and climb walls with irregular surfaces. Whereas, newer Alicia 3 [60] has merged wheel-driven locomotion and legged locomotion that enables the robot to move up and down to overcome obstacles of 10 – 12 cm [61]. The system illustrated in Figure 2-6 consists of three adhesion modules joined together using two rods and a special rotational joint that allows the system to detach the three

modules one by one to step over an obstacle. The combination of locomotion means Alicia 3 can overcome bigger obstacles with better manoeuvring capability compared to its predecessors. Another good illustration of hybrid locomotion is SIRIUSc [62] in Figure 2-7, a facade cleaning robot with wire and sliding frame locomotion. The wire rail is used to navigate the robot vertically and laterally from one panel of the facade to the next while its advanced linear transition sliding frames ensure constant adhesion between the robot and the facade through the use of vacuum suckers. The sliding frames also function as continuous alternating upwards and downwards driving mechanism.

Figure 2-6. Alicia 3's obstacle avoidance procedure [50].

Figure 2-7. Facade cleaning operation using the SIRIUSc robot and its base station on the roof of a high-rise building [62].

Table 2-1 shows a comparison of the main locomotion principles discussed in this section with their strengths and weaknesses. Depending on the application, the design requirements may be of different importance. Therefore, the locomotion method has to be selected depending on that basis.

Table 2-1. Summary of comparison between the main locomotion principles.

Design requirements	Arms and legs	Sliding frames	Wheels and tracks	Wires
Motion	Not continuous	Not continuous	Continuous and smooth	Continuous
Speed	Slow	Slow	Fast	Relatively fast
Movement	Multiple DoF based on number of legs	Two DoF	Multiple DoF	Two DoF
Payload capacity	Low	Moderate	Moderate	Very high
Adaptability	Suitable for rough and uneven surfaces	Suitable for even surfaces	Suitable for uneven porous surfaces	Any surfaces
Complexity	Highly complex control systems	Moderate complexity	Less complexity	Very simple

2.4 Adhesion principles

There are many adhesion mechanisms that range from the common methods of suction pads and permanent magnets to most recent biological models and chemical adhesives. The main focus in designing an adhesion module is to generate high holding force to avoid slipping and capsizing as well as carrying a reasonable amount of additional payload in the form of NDT equipment. This section describes the most researched adhesion principles, their advantages and disadvantages.

2.4.1 Magnetic adhesion

Permanent magnets have been used as the nominal adhesive method in designing robots that are able to climb ferrous surface for a long period. The “WCR System” [63] is an example of a wall climbing robot of such category developed by a team from Cambridge University. The application of the robot was to label the scale of steel oil storage tanks. Later a number of robots were developed and patented based on the same principle. A non-contact magnetic adhesion mechanism proposed in [64] implemented arrays of magnets under the chassis of the robot as shown in Figure 2-8 at constant gap of 5 mm between the magnet and the wall surface was maintained. However, the effect of multiple magnet layer and the distance between the magnets on total adhesion force are not investigated in that study. Another permanent magnet based tracked robot presented in [65] investigated the effect of air gap between multiple magnets and the steel surface. The robot consisted of an aluminium frame and track wheels with permanent magnets located on the steel channels. The track wheels and the magnet attachment are shown in Figure 2-8. However, the effect of distance between the

magnets, effect of magnet dimension on the overall adhesion force have not been investigated.

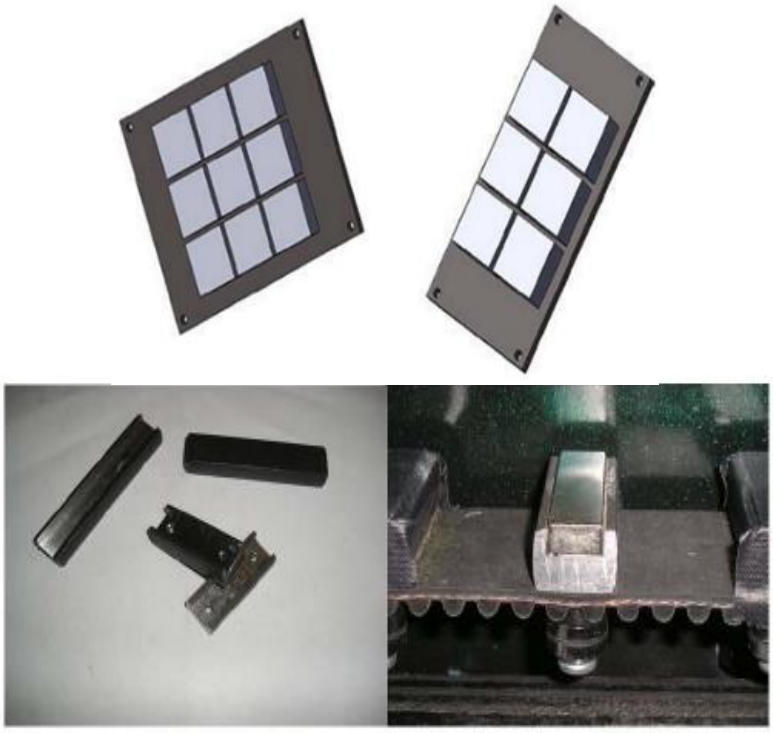

Figure 2-8. Arrays of rare earth permanent magnets mounted on a steel plate as proposed in [64] (top) and the tracked wheels and magnet spacing as in [65] (bottom).

Another robot was developed in [66] based on the magnetic wheel system. In this case the wheel was constructed of magnetic material and the effect of different wheel rim on the distribution of magnetic flux lines was investigated on both planer and curved surface. The robot could achieve 60 N of maximum adhesion force while climbing a ferrous surface. The CAD diagram and the components of the optimized wheel are given in Figure 2-9. Other notable magnetic wheel based climbing robot is Magnebike robot [67] that implements single magnetic layered disk that is sandwiched between two magnetic wheel plates of larger diameter. The entire wheel structure is covered by a thin rubber layer that provides friction along the climbing surface. The obstacle avoidance procedure is carried out by lifting the robot chassis using linear actuators.

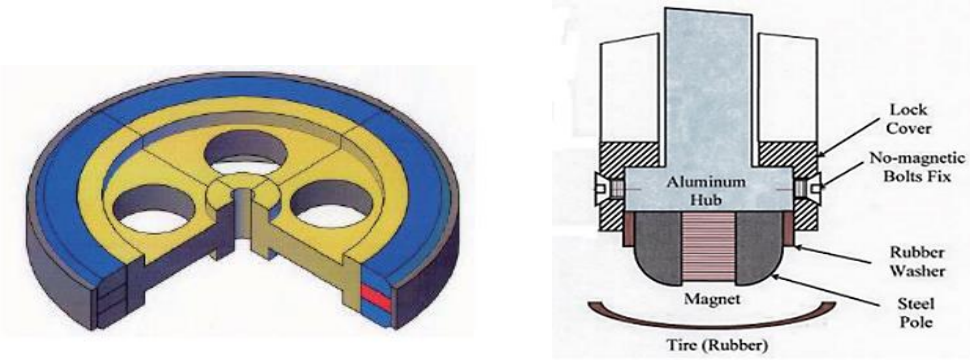

Figure 2-9. Optimized design of a magnetic wheel proposed in [67].

A non-contact adhesion mechanism has been proposed in [68]. Here magnets are arranged in a big area under the chassis with a gap between the wall and magnet surface. The attraction area is big enough to generate a big adhesion force of 1000 N at 15 mm air gap so the robot can carry a heavy load. The magnets are placed at 50 mm interval using aluminium holder as shown in Figure 2-10. However, the effect of multiple magnet layer and the distance between the magnets on total adhesion force are not investigated. Moreover, the total system mass is 80 kg that limits the system portability and it requires 30 mm thick ferrous surface to generate sufficient attraction force to carry its heavy body mass.

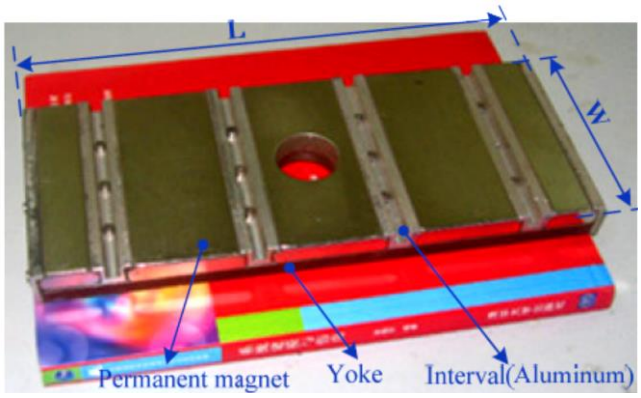

Figure 2-10. Design of the magnetic module designed in [68].

Most recently, versions of magnetic adhesion system using electromagnets have been reported in [69], [70]. The adhesion force generated by the electromagnets depend on the number of winding turns, the radius of the core and the amount of current passed through the windings. Electromagnets can generate high adhesion force but lacks the sufficient frictional force because both the electromagnet and the climbing surface are made of steel. Therefore, introducing a material with high friction coefficient between the climbing surface and the electromagnet increases the frictional force as the material is dragged onto the surface [70]. However, electromagnets require very high current to produce sufficient adhesion force for payloads. High energy requirements and the size of the windings make electromagnets an unlikely candidate in industrial applications.

2.4.2 Suction

The most frequent approach to adhesion on a surface is to implement suction and pneumatic adhesion. These systems are mainly used for non-ferromagnetic, non-porous, relatively smooth surfaces, and can be applied to a large suction area to increase the adhesion force. Robots using suction include climbing robot for inspecting nuclear power plants [71], a robot using tracked wheel mechanism with passive suction pads [72] and two other four limbed robots with suction pads attached [73]. Vacuum is an

active type suction mechanism that requires lightweight mechanics and provides easy controls. More often vacuum is generated by using vacuum pumps that produce a large adhesion force through flow volume or a high negative pressure depending on the robot's setup. Compared to passive suction cups techniques, active vacuum systems are able to operate also on more rough surfaces such as systems like WallWalker [74], BIT climber [75] etc. The initial limitation of the suction mechanism is that it requires time to develop enough vacuum to generate sufficient adhesion force and as a result, the speed of the robots using suction is relatively low [76]. Moreover, the use of vacuum pumps makes the system noisy and high in energy consumption.

To address this problem, [77] designed a vacuum rotor package called vortex to generate a low pressure zone enclosed by a chamber. The high speed rotor that consists of vacuum motor with impeller causes the air to be accelerated toward the outer perimeter of the rotor and away from the centre radially. The resulted air exhaust is directed towards the rear of the robot creating an adhesion towards the climbing surface. With the help of adequate sealing, this low pressure zone thrusts the robot body towards the climbing surface. The aerodynamic process of the rotor is given in Figure 2-11 below. However, the resultant adhesion force from vortex technology is not enough to support a reasonable payload. Moreover, as the gap between the climbing surface and the chamber is required to be absolutely minimized, robots using vortex technology cannot offer floor-to-wall transitions.

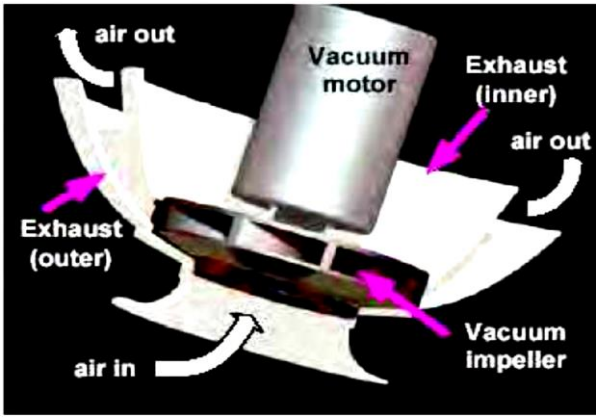

Figure 2-11. Vacuum rotor chamber with impeller used in Vortex generation [77].

2.4.3 Biological models

Researchers also investigated the application of biological agents in robot design. The Lemur II is an example of such design [78]. It can climb vertical rough vertical surface with the help of four limbs. The foothold locations are constrained to a set of discrete points which assists the robot to stick vertically. Another example of such design is the RiSE robot which imitates the movement of a Hexapod [79]. A special type of micro

spines is attached to its six feet for reliable attachment to uneven surfaces. It also uses about 20 different motors at different position for manoeuvring over large obstacles. A more advanced robot based on the same design principle is CLIBO [80]. It is structured in such a way that it poses the ability of high manoeuvrability and transfer (although not implemented yet) between angled surfaces using only 16 motors. A robot design derived from human climbing behaviour was developed named the ROCR [81]. It is a pendular module with two links. It has an actuated tail that thrusts sideways and propel the robot upwards on a rough vertical terrain. A serial chain is also used between its two pendular to create alternating handhold. Figure 2-12 illustrates robots using on numerous mechanical and biological model based adhesion system.

Lemur II [78] RiSE [79] CLIBO [80] ROCR [81]

Figure 2-12. Robots using mechanical and biological model based adhesion.

Another new adhesion technology based on electrostatic mechanism is emerging through the research in [82], [83]. This is a new discipline of research combining material science and robotics that investigate conductive electrodes and insulated substrates to generate electrostatic attraction between the climbing surface and the robot body. [82] reports 0.3 N/cm^2 of attraction on dry concrete and 4.24 N/cm^2 on steel surface using this method. The climbing process of those robots are presented in Figure 2-13. A comparison between all different adhesion principles based on the system requirements can be drawn as in Table 2-2 for better understanding of system viability.

Figure 2-13. Electroadhesive climbing robots by [82] and [83].

Table 2-2. Compariosn of adheison mechanisms based on system requirements.

Design requirements	Suction cups	Vacuum chamber	Electro magnet	Permanent magnet	Biological models and others
Surface type	Even, non-porous surfaces like glass, steel etc.	Porous and non-porous surface of any materials	Ferrous surface only	Ferrous surface only	Various even uneven surfaces
Payload	High	Relatively high	Moderate, depending on the electromagnet's size	Very high	Very low depending on the mechanical design
Reliability	Good	Moderates, needs proper sealing of the chamber	Unreliable due to high energy requirement	Highly reliable	Unreliable, not suitable for industrial applications

2.5 Research gaps in current climbing robotic technology

This literature review has identified numerous limitations in both locomotion and adhesion mechanism of climbing robots. A number of systems have adapted arms and legs for locomotion that offer manoeuvrability over rough surfaces and cracks with wide DoF. However, high number of limbs require complex harmonic gait control and mechanical design. Together with low speed of the system motion, this locomotion technique is not feasible to deploy on large area (> 1000 m^2) inspections. Likewise, sliding frames locomotion has discontinuous movements due to the stick-move-stick-move principle. Systems with sliding frames have comparably larger size to accommodate the frames and offer only two DoF. As a result, the systems have difficulty in crossing cracks and obstacles as well as limited motions in the plane.

Wire driven locomotion offers the simplest of locomotion that involves abseiling down from the roof using conveyor belts installed between the roof and the ground. Like frame structures, wire driven system can only move upwards and downwards. As sideways movement require repositioning the abseiling base, this method is ineffective for tall structures.

In terms of different adhesion mechanisms, the suction cup option is widely used for non-magnetic surface climbing robots. Traditionally, vacuum pumps, often in the form of suction cups, are used as vacuum producers. They can produce high vacuum and large suction force. Sealing is an important design factor of vacuum suction cups as a minute air gap or a hole on the vacuum chamber can cause deduction in adhesion force

and failure of the climbing process. On the other hand, very tight sealing generates frictional force that opposes the driving force. A robot using vacuum suction in [65] for example has an adhesion force of 250 N and 88 N of frictional force that opposes that adhesion. Therefore, a design trade-off must be sought to determine an optimum level. Moreover, when suction cups and vacuum pumps are applied to a wall climbing robot, some pneumatic components such as solenoid valves and regulating valves are also needed [79]. Therefore, the mass of the robot is high and not desirable especially when high flexibility of locomotion is required. Newer vortex adhesion can address few of the issues faced by the conventional suction mechanism. But only few systems have been developed so far as the researchers try to understand this adhesion principle and analyse the aerodynamic of these systems. Also vortex adhesion has high energy consumption rate because of high speed rotating impeller and provides comparably low payload capacity.

Magnetic adhesions, especially permanent magnet based systems can offer higher adhesion force at the cost of zero energy. Many research works have been conducted to increase magnetic adhesion force by simulations and experiments, however, configuration of different magnetic arrangements has not been investigated further. Moreover, adhesion principles of biological models and electro-adhesion are still in development stage and not completely understood. The adhesion force achieved from those systems is very low and their mechanical designs make this category less deployable in industrial environments. As a result, few practical products have been developed for reinforced concrete surfaces, though wall-climbing robots have been researched for many years.

2.6 Chapter summary

This chapter has highlighted the design aspects of climbing robots in terms of locomotion and adhesion. The main limitations found in sliding frames and legs are its low DoF as well as complicated mechanical structure. The largest gaps in the current level of research were identified in the adhesion mechanism where suction cups and vacuum generators have issues with sealing and heavier mechanical design. This research targets to identify opportunities to increase adhesion force achieved from using less number of permanent magnets by implementing methodical parametric study. Together with the wheel locomotion that offers fast and continuous movement and the simpler mechanical structure and control elements, the novel permanent magnet based adhesion can be the next breakthrough in climbing robotic technology.

Chapter 3. Parametric analysis of the adhesion module

This chapter presents the FEA based design optimization of the permanent magnet based adhesion module. The construction method of concrete structures is discussed in light of international regulations that specify the nominal concrete cover. This chapter also outlays the static and dynamic force analysis of the robot in order to determine the required adhesion force for safe climbing operation. The emphasis of this chapter is the optimization studies of different design variables such as magnet dimension, yoke design etc. This chapter is structured as follows:

3.1 Overview

The nominal workplace of climbing robots is on the vertical plane and the main design requirement is to have a strong adhesion system that can support the robot weight and the additional payloads depending on the field of application. In terms of concrete inspection task, the robot needs to carry on-board inspection equipment such as the cover-meter or the GPR. The typical system mass of those instruments can vary from 3 – 7 kg. Therefore, the desired payload capacity of the robot should be more than 7 kg depending on the robot's own mass. The main challenge in developing a permanent magnet based adhesion module applicable for reinforced concrete structure is to shape and concentrate magnetic flux to penetrate the concrete cover as deeply as possible. Deeper penetration can ensure maximized magnetic coupling between the adhesion module and the rebars in order to gain sufficient magnetic adhesion. Therefore, the importance of concrete cover is vital in determining the design parameters of the adhesion module. The dimension of concrete cover is dependent on the concrete structure category governed by the international regulatory boards. Furthermore, pinpointing the required adhesion force for successful climbing operation relies on the dynamic force analysis that takes into account different directional forces acting on the robot on a vertical plane.

In this chapter, the nominal concrete covers for different types of concrete structures are identified along with the dynamic force analysis. By taking these two measurements into consideration, an FEA based parametric analysis of design variables such as magnet dimension, geometry of the flux concentrator etc. is presented in this chapter. The effects of these design variables are carried out using Comsol Multiphysics suite and the results obtained from this analysis will outline the optimum design of the proposed adhesion module.

3.2 Measurement of the concrete cover

Reinforced concrete is integrated with various kinds of reinforcement such as ferromagnetic steel bars and aggregates with the concrete to increase the strength of the structure. Concrete is a brittle material. It has strong compression force but cannot withstand strong tensile stress [84]. As a consequent, cracking on a non-reinforced concrete plane could easily occur if excessive force is applied by external loading as shown in Figure 3-1. In most cases, the force is much greater than the optimum tensile

stress of the concrete plane that this disproportionate force will cause the concrete plane to bend and eventually crack.

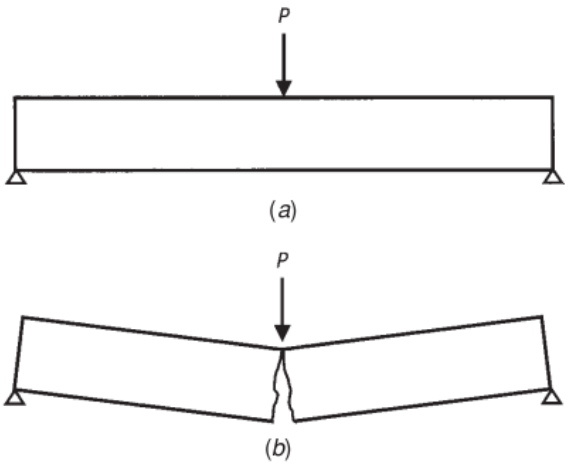

Figure 3-1. Cracks on a concrete plane (a) Bending Force < Tensile, (b) Bending Force > Tensile [84].

In order to increase the tensile strength, steel rebars are used as reinforcement with concrete. Nuclear and other safety critical structures are reinforced with the dense meshing of rebars using special techniques to distribute the concrete as it is poured [85]. Despite the fact that introducing rebar enhances the overall structural strength, a correct rebar positioning is critical. For instance, if rebars are located near the bottom surface of a concrete slab and if the surface is subjected to excessive force applied by the load then this will lead to appearance of cracks on the bottom plate which is shown in Figure 3-2.

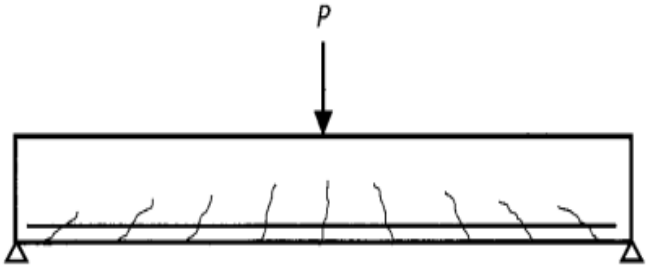

Figure 3-2. Cracks due to inaccurate rebar positioning [84].

Likewise, if rebar is located too close to the outer surface of concrete, it will expose easily to rain water and start to corrode. Excessive corrosion will lead to spalling and concrete delamination. Rebar corrosion weakens the building foundation and thus the total stability of the building. The process of rebar corrosion is demonstrated by the Figure 3-3.

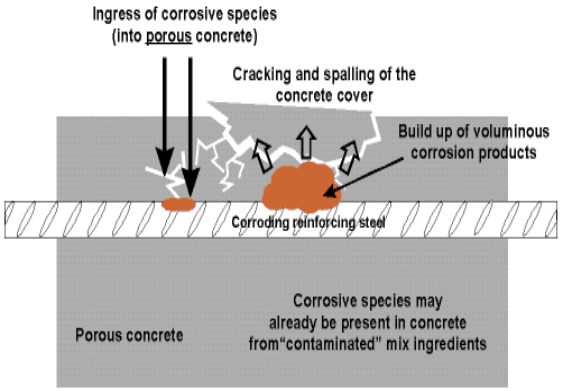

Figure 3-3. Rebar corrosion process [86].

Therefore, a correct rebar positioning is critical and must follow a standard for overall structural strength. The standards applicable in UK that determines the minimum concrete cover requirement is BS 850 and Eurocode 2. All member countries of European Union (EU) including the United Kingdom must follow those regulations. Eurocode 2 discusses about construction regulations of concrete structures. In this standard, the minimum concrete cover for different types of structures are defined. It also suggests on the recommended rebar size and diameter that could be used based on the structure types.

In Eurocode 2, different structures are categorized in different classes [87]. According to the guidelines described in chapter 4 of the Eurocode 2, buildings and power plants are XC3 and XC4 class structures as they are exposed to cyclic wet, dry and moderate humid conditions.

Bridge columns that are submerged in water are XC1 class. As roads and bridge decks react more often with snow and de-icing agents so they are classed as XF4 category. Dams are XC4 class constructions due to their regular contact with cyclic wet and dry conditions.

Based on the class identification of various structures, Eurocode 2 devised a formulation that determines the nominal cover for those structures. The equation follows as:

$$C_{nom} = C_{min} + \Delta C_{dev} \quad (3.1)$$

Here,

C_{nom} = Nominal concrete cover.

C_{min} = Minimum concrete cover.

ΔC_{dev} = Allowance in design deviation = 10mm.

Eurocode 2 also specifies the nominal concrete cover for different classes of structures. The nominal concrete cover is determined based on the type of environmental exposure, concrete quality, and intended working life of the structure. The nominal cover requirement for atmospheric exposure of 50 years working life extracted from Eurocode 2 is given in Table 3-1.

Table 3-1. Nominal concrete cover for different structures based on Eurocode 2.

Structures	**Environmental Exposure Class**	**Nominal cover for intended working life of 50 years (mm)**	**Nominal cover for intended working life of 100 years (mm)**
Buildings (Vertical elements exposed to rain and snow)	XC3/XC4	30-60	40 - 75
Bridge Columns	XC3	30 - 60	40 - 75
Dam	XC2	35 - 60	35 - 75
Nuclear Power Plant	XC4	30 - 60	40 - 75
Pavements	XD3	50 - 60	55 - 75
Car Park Slab	XD3	50 - 60	55 - 75

The target operating structures for the climbing robot proposed in this research will be tall buildings, dams, brides and power plants. Therefore, it can be established from the table that the range of nominal concrete cover of maximum 60 mm must be dealt with by the adhesion module to gain magnetic coupling with the rebars.

In addition to concrete cover, rebar diameter and gap between two rebars in concrete might also influence the magnetic flux concentration induced by permanent magnets. Therefore, the payload capacity of the robot might alter based on the rebar size and spacing. As mentioned in Eurocode 2, the length of the rebars could vary depending on the construction. However, the gap between two adjacent rebars is constant which

measures 20 mm. Table 3-2 has been reproduced from the Eurocode 2 below which details the recommended rebars diameter used in the construction process.

Table 3-2. Recommended radius and diameter of the rebars [87].

Nominal Rebar Diameter, d (mm)	**Minimum radius for scheduling, r (mm)**	**Minimum diameter of bending former, M (mm)**
6	12	24
8	16	32
10	20	40
12	24	48
16	32	64
20	70	140
25	87	175
32	112	224
40	140	280
50	175	350

However, in modern construction process, rebars having diameters less than 8 mm and more than 50 mm are not used. Hence, the experimental setup for this research is conducted using rebars of 8 – 50 mm diameters. Nonetheless, rebars of 50 mm diameter are still in use for constructing heavy duty nuclear power plants and motorway bridge columns.

3.3 Force requirement analysis

As the robot is operating on a vertical plane, the robot may experience capsizing, slipping or rolling-over. The adhesion force therefore must be strong enough to prevent those limitations and ensure system safety. Static and dynamic force analysis play crucial part in determining the required adhesion force. When the robot stands still on a vertical plane, it bears forces as the gravity, frictional etc. Consider the directional force acting on a robot resting on a plane as shown in Figure 3-4.

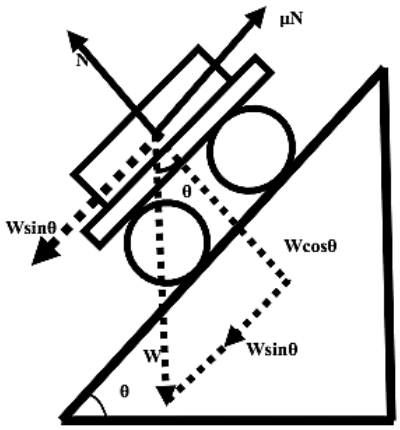

Figure 3-4. Free body diagram of a robot moving on a plane.

3.3.1 Sliding avoidance

The main parameters are robot weight (W), vertical plane's angle of inclination (θ) the wheel's coefficient of friction (μ), height of the centre of gravity from the climbing surface (h), distance between the front and back wheel (L), robot mass (m), acceleration (a). Then, the required adhesion force, F_a is,

$$\sum F_x = W \sin\theta - \mu N = 0 \tag{3.2}$$

$$N = \frac{W \sin\theta}{\mu}$$

$$\sum F_y = W \cos\theta + F_a - N = 0 \tag{3.3}$$

$$N = W \cos\theta + F_a$$

$$\frac{W \sin\theta}{\mu} = W \cos\theta + F_a$$

Therefore, for the robot to avoid slipping on a still position, the least required F_a is,

$$F_a > \frac{W \sin\theta}{\mu} - W \cos\theta \tag{3.4}$$

While the plane is totally vertical then, $\theta = 90^0$ and Equation ((3.4) becomes,

$$F_a > \frac{W}{\mu} \tag{3.5}$$

If the robot is in motion and accelerating on the plane then the required, F_a is,

$$F_a > \frac{W + ma}{\mu} \tag{3.6}$$

3.3.2 Capsizing avoidance

While the robot is stable on a totally vertical plane, rotation about the point *A* in Figure 3-5 will cause the robot to capsize. Therefore, the torque induced at the front end of the robot by the adhesion module should be larger than that induced by the weight, *W*. At the point *A*, the torque balance equation can be given as,

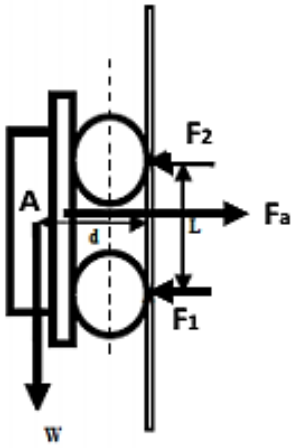

Figure 3-5. Free body diagram of the robot operating on a vertical plane.

$$\sum \tau = W\ d + \ F_a\ L = 0 \tag{3.7}$$

$$F_a > \frac{W\ d}{L} \tag{3.8}$$

Therefore, the adhesion module unit should satisfy Equation (3.8) so that the robot can absorb on the surface. In order to avoid capsizing, the height of the centre of gravity should be kept low while the distance between the two wheels is preferred to be large.

3.3.3 Roll-over avoidance

The motor used for the robot locomotion must be of high torque for the robot to propel forward on the vertical plane and avoid roll-over. Considering the free-body robot diagram as in Figure 3-5, if the wheel radius is *r* and the required rolling force is F_r, then the required motor torque, τ_m is,

$$\tau_m = W\ d + \ F_r\ r \tag{3.9}$$

As $F_r = \ \mu F_a$ therefore,

$$\tau_m = W\ d + \ \mu\ F_a\ r \tag{3.10}$$

If *x* number of wheels are used for locomotion, torque required by each wheel will be,

$$\tau_m = \frac{W\ d + \ \mu\ F_a\ r}{x} \tag{3.11}$$

3.4 Parametric optimization

A permanent magnet attracting any ferromagnetic material is a natural phenomenon. However, the objective of this section is to mathematically analyse the characteristics of permanent magnet. As established in the previous section that the optimum concrete cover varies from 25 – 60 mm depending on structure type. Therefore, the key research questions that will be investigated in this section are:

- How to shape the magnetic field to penetrate 25 – 60 mm deep into concrete surface to establish magnetic coupling?
- What are the key design parameters that affect the adhesion force?
- What should be the optimum size and weight of the adhesion module?

According to the theoretical model, magnets dimension and material, size of the concentrator (yoke), rebar arrangement layout influence the magnetic flux and its behaviour. Therefore, the key design parameters could be identified as:

- The distance between magnets,
- Yoke thickness,
- Yoke design,
- Arrangement of multiple magnets,
- Rebar meshing layout.

To understand the design criteria of an adhesion module for reinforced concrete structures, 3D model simulations are carried out using Comsol Multiphysics. Neodymium grade N42 magnets and grey cast iron DT4 are used as the yoke. The main properties of the materials are listed in Table 3-3.

The ratio between the achieved adhesion force, F_a and the system weight, W directs the performance of adhesion unit. Here, the ratio, η is,

$$\eta = \frac{F_a}{W} \tag{3.12}$$

Therefore, the optimized target is to achieve as large an adhesion force with lowest weight of the total robotic system possible.

Table 3-3. Material parameters used for Comol Miltiphysics simulations.

Properties	Value
Magnetic induction intensity, B_r (T)	1.31
Coercive force, H_{cb} (KA/m)	915
Intrinsic coercive force, H_{ci} (KA/m)	955
Magnetic energy product, HB (KJ/m^3)	318
Relative permeability of neodymium magnets (μ_r)	1.068 - 1.113
Relative permeability of steel rebars (μ_r)	1500
Relative permeability of yoke (μ_r)	5000

3.4.1 Effects of the distance between two magnets

To investigate the effects of distance between two magnets, models are built using two magnets attached on a yoke in opposite polarity as shown in Figure 3-6. In this simulation setup, used dimensions are rebar diameter, R_d=12 mm, yoke thickness, Y_t=15 mm; concrete cover, C_c=30 mm. Magnets of 50×50×10 mm and 100×100×10 mm dimensions have been used for better comparison. The distance between the magnets are varied from 10 mm to 150 mm and the magnetic flux density norms are observed from the simulations.

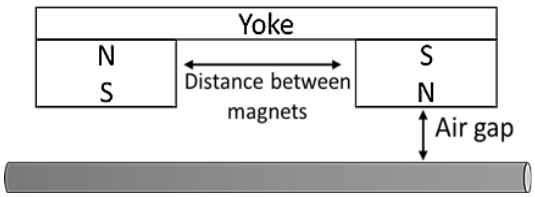

Figure 3-6. Block diagram of the magnetic circuit.

The heat maps in Figure 3-7 represent the magnetic flux concentration norm for magnets with 50 mm length along the rebar. It is observed that, as the distance between the magnets is increased from 10 mm, the flux concentration area increases which is shown by the red hotspot in the rebar. The area of red hotspot continues to increase until the distance between the magnets is 50 mm. At distance greater than 50 mm, magnetic flux concentration starts to decay as represented in yellow area. There are no interactions between two magnets at even higher gaps where the magnets attract the rebar independently. Same trend is observed for 100 mm long magnets, however, the

flux concentration reaches its peaks when the distance between two nearby magnets is 100 mm in this case.

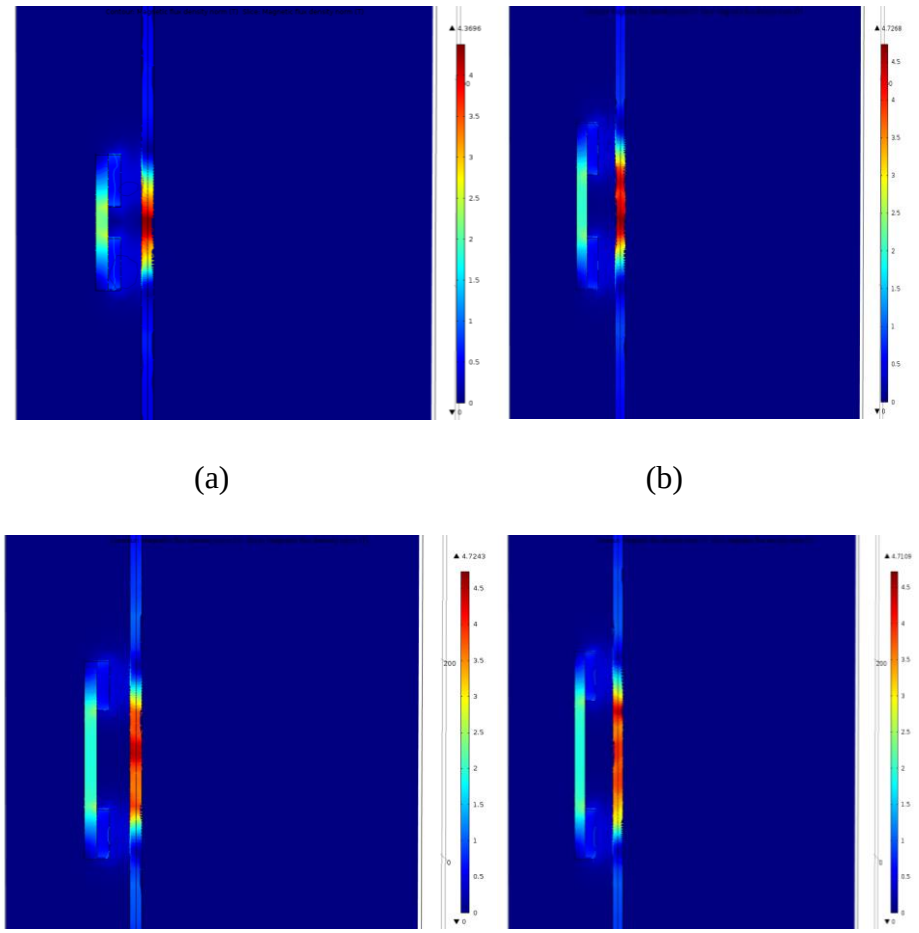

(a) (b)

(c) (d)

Figure 3-7. Magnetic flux concentration norm at different distances between magnets; (a) Distance: 10mm, (b) Distance: 30mm, (c) Distance: 50mm, (d) Distance: 100mm.

Effects of the magnetic flux concentration area is reflected on the simulated adhesion force as given in Figure 3-8. As the distance is varied from 10 mm to 150 mm, the adhesion force would increase greatly at the beginning from 47.5 N to its peak of 64.93 N at 50 mm distance. At distances greater than 50 mm, magnetic flux density along the rebar starts to deteriorate and in turn there is a gradual fall in the resultant adhesion force to 51.38 N at 150 mm distance between magnets. Therefore, based on the hotspot area and the adhesion force, 50 mm indicates the optimum distance between the magnets. Moreover, as the distance between the magnets is increased, the yoke length has to be increased in proportion to that. Therefore, as the distance continues to increase above 50 mm, the value of η shown in Figure 3-9 decreases from a maximum of 5.87 at a fast rate due to the added system weight.

Likewise, for 100 mm long magnets, the adhesion force increases by 45% to 151.81 N as the distance is increased from 10 mm to 100 mm. Then there is a gradual fall in adhesion force with the increase in the in-between distance.

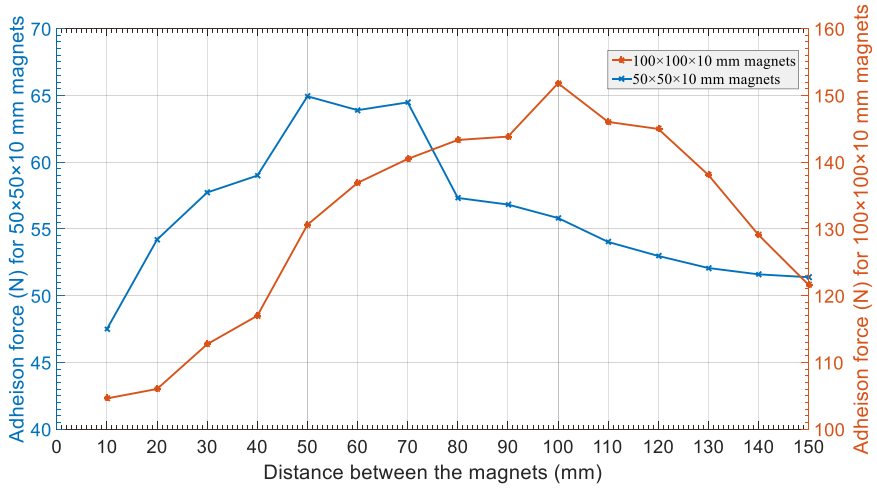

Figure 3-8. Simulated adhesion force measurements at different distances between the magnets.

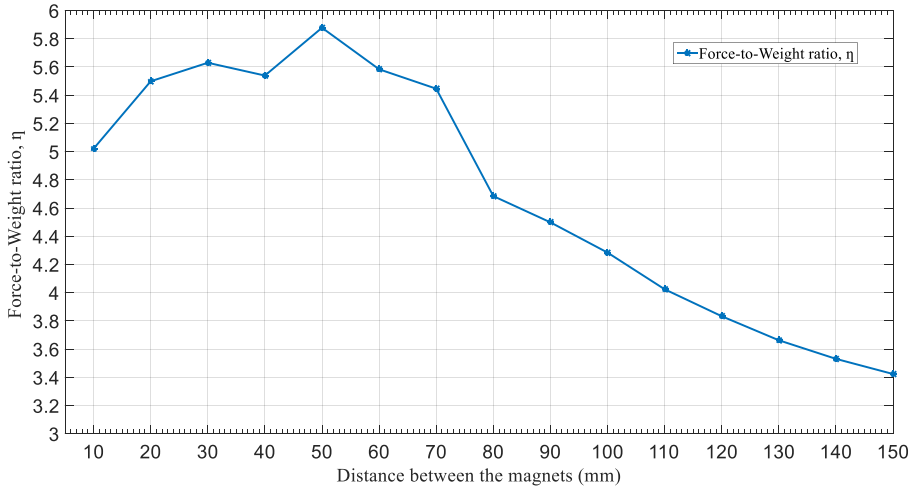

Figure 3-9. Relation between Force-to-Weight ratio, η and the distance between the magnets.

These simulation setups indicate that an optimum distance between the adjacent magnets is vital to create a balanced magnetic circuit. This optimum distance depends greatly on the magnet length used as seen from the simulation results where the maximum adhesion force is achieved at the distance of 50 mm and 100 mm for 50 mm long and 100 mm long magnets respectively. Therefore, the in-between distance should be equal to the magnet length. In final optimization, a smaller magnet length of 50 mm will be ideal is this will require smaller yoke size compared to a 100 mm long magnet. This smaller yoke size will result in better Force-to-Weight ratio, η.

3.4.2 Effects of the magnet dimension

As the optimum distance between the magnets has been recognized to be equal to the magnet length, emphasize should be given to identify the optimum size of the magnets. This parameter can provide clear indication of whether thicker magnets with short width or wider magnets with small thickness will be ideal. The dimension of the magnets directly affect the dimension of the yoke therefore, their optimization must be critically examined. In order to do so, separate sets of simulations are carried out using variable magnet width and thickness.

First the magnet thickness is varied from 5 mm to 20 mm and the length and the width are set constant to 50 mm and the yoke thickness to 20 mm. The resultant adhesion force graph illustrated in Figure 3-10 confirms that with increased thickness, the adhesion force increases sharply from 21.57 N to 144.11 N at 20 mm thickness. As the magnets thickness is doubled from 5 mm, the force experience a three times increase. Therefore, the rate of growth is very significant. Although the magnet thickness is varied, the yoke dimension stays the same throughout, there is minimal addition of weight and the ratio, η is also in proportional increase during each step.

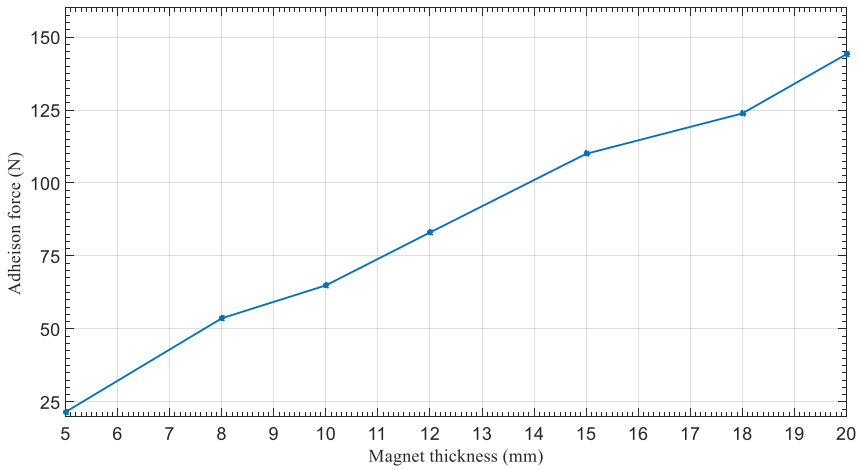

Figure 3-10. Adhesion force for different thickness of magnets used.

Effects of the magnet width is measured by varying the magnet width from 25 mm to 100 mm while setting the magnet length to 50 mm and the thickness to 10 mm. Results in Figure 3-11 show that increased width results in increased force. At 25 mm width, the force is 25.97 N that rises by 38.96 N as the width doubles. At four times the initial width, adhesion force has an increase of only four times. However, the width of

the yoke must also be increased to cover the entire magnet area. As a result, the ratio, η suffers greatly due to the magnet width increase.

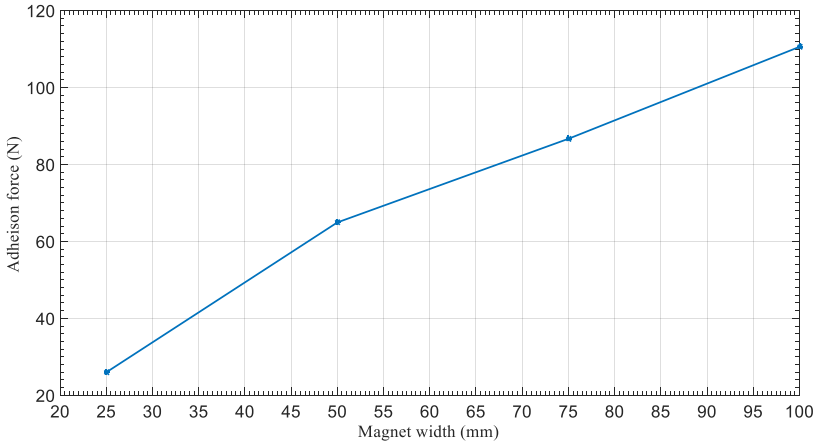

Figure 3-11. Adheison force for different width of magnets used.

In comparison of thickness increase and width increase, the growth rate of adhesion force is higher if the thickness is increased rather than the magnet width as confirmed in Figure 3-12. Furthermore, increased magnet thickness does not alter the yoke dimension therefore, it provides better η ratio compared to increase in the magnet width. As a result, a thicker magnet is ideal to be implemented in the final adhesion module design.

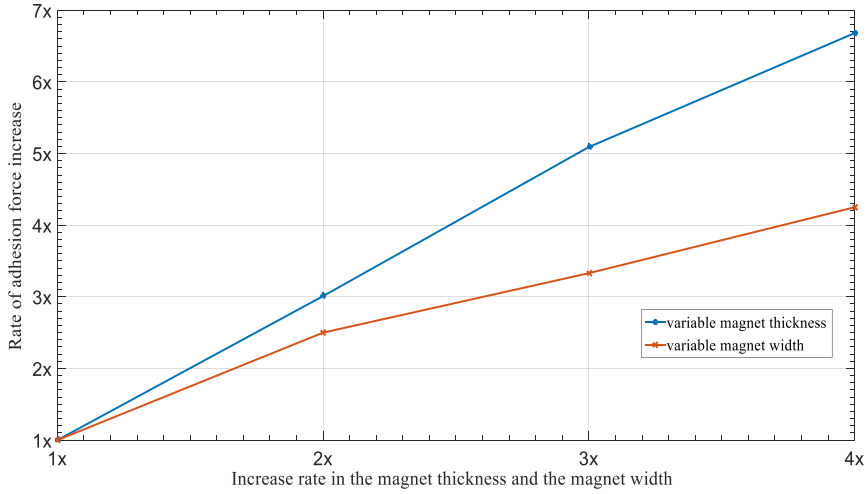

Figure 3-12. Compariosn of adheison force increase rate between the variable magnet thickness and width.

3.4.3 Effetcs of the yoke

Previous simulations show that the use of yoke significantly increases the adhesion force. Using only two magnets placed at 50 mm distance between them without any

yoke results in adhesion force of only 39.34 N for concrete cover of 30 mm. But implementing a yoke of 5 mm thickness increases the adhesion force significantly to 53.71 N. Therefore, the thickness of yoke plays a critical part to maximize adhesion force. To investigate this parameter further, models with varied yoke thickness from 1 mm to 40 mm are simulated using 50×50×10 mm sized magnets.

The adhesion force found to be increasing significantly when the yoke thickness is increased from 1 mm to 20 mm. A yoke of 1 mm thickness does not have any apparent effect on adhesion force as the flux leakage is higher in all directions as shown in magnetic flux density norm in Figure 3-13(a). Any influence of yoke thickness appears when the thickness is increased to 5 mm, the system achieves magnetic coupling with rebar. At 20 mm thickness, the flux concentration is at maximum and reaches maximum adhesion force of 64.93 N. Moreover, the magnetic flux leakage is lower on the yoke's opposite surface when the yoke thickness is significantly large such as 40 mm and more flux lines are concentrated toward the rebar shown as a red hotspot in Figure 3-13(b).

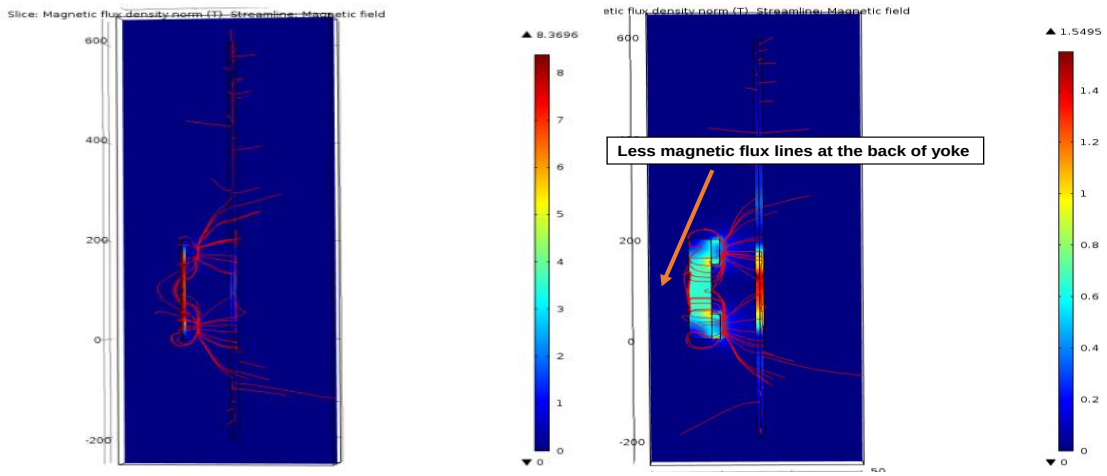

(a) (b)

Figure 3-13. Magnetic flux density norm at yoke thickness; (a) 1mm, (b) 40mm.

According to the adhesion force at different yoke thicknesses graphed in Figure 3-15, the adhesion force comes to a saturation level of approximately 62 N at 25 mm yoke thickness and further increase in yoke thickness would not have any significant influence on adhesion force. The primary reason for this is that, magnetic flux lines prefer to pass through the medium of high permeability. When the yoke thickness exceeds an optimum point (in this case 25 mm), the magnetic flux lines prefer to pass through the higher magnetic permeable yoke rather than air (magnetic permeability of 1) as illustrated Figure 3-14. Thus, the magnetic coupling with the rebar is minimum to influence the adhesion force when the yoke thickness is greater than its nominal value.

Furthermore, according to the force-to-weight ratio, η of the adhesion module in Figure 3-15 falls sharply because of the added weight of thicker yoke.

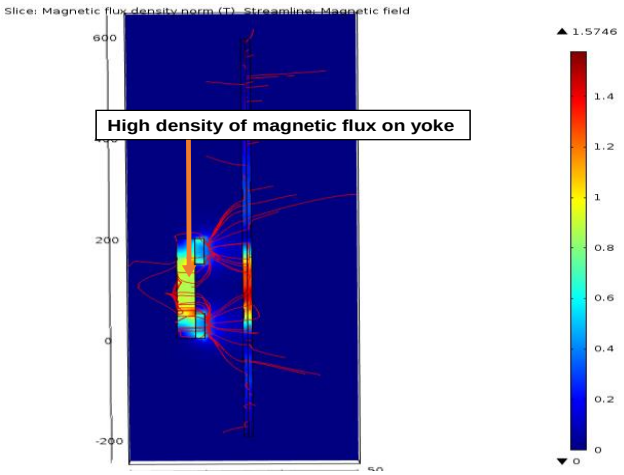

Figure 3-14. Density of magnetic flux on a 25 mm thick yoke.

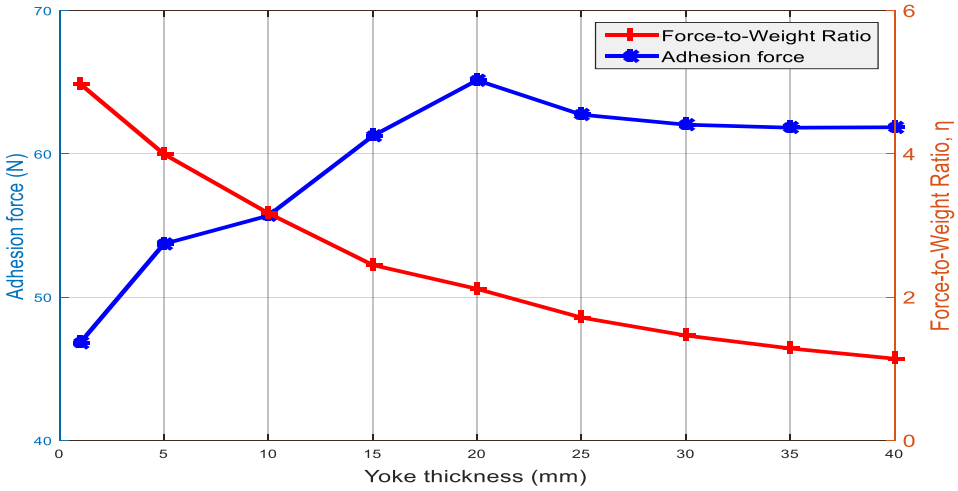

Figure 3-15. Adhesion forces and the values of η for yokes with different thicknesses.

While the built material of the yoke is taken into account, adhesion force measurements for 20 mm thick yokes of different materials in increasing permeability shows that the value of magnetic permeability has negligible influence on adhesion force as the graph shown in Figure 3-16.

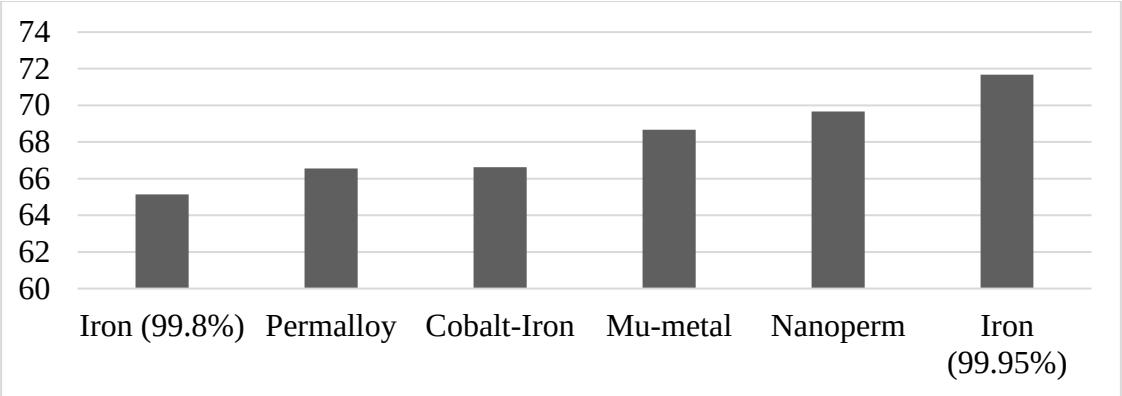

Figure 3-16. Adhesion force comparison for different yoke materials.

In this case, 102.5 N of adhesion force is achieved from iron (magnetic permeability 5000) yoke compared to 104 N from 50,000 permeable Mu-metal. 99.95% pure iron has a permeability value of 200,000 but offers only 104.5 N of adhesion force. Therefore, the yoke material plays an insignificant part in the achievable adhesion force.

3.4.4 Optimization of the yoke design

The main functionality of the yoke is to minimize the flux leakage and concentrate the magnetic flux towards the rebars. In order to establish the optimum yoke design, four categories of yoke designs as given in Figure 3-17 have been investigated. The thickness of the yokes is fixed at 20 mm. The adhesion force achieved from each yoke recorded in Table 3-4 shows that all four designs achieve approximately the same level of adhesion force.

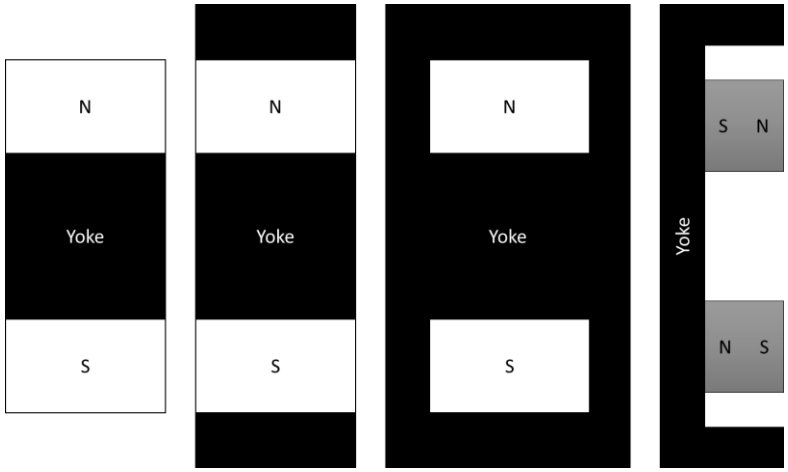

Figure 3-17. Different yoke designs under investigation.

Table 3-4. Adhesion force achieved from different yoke designs.

	Yoke 1	Yoke 2	Yoke 3	Yoke 4
Adhesion force (N)	64.93	60.96	56.18	70.68

However, the magnetic flux norm graphs reveal the effects of different designs to a greater extent. In case of design 1, the flux lines are concentrated towards the rebar and there is minimum flux leakage on the opposite side due to thick yoke. However, due to having an extended yoke area in case of design 2 and 3, the magnetic flux lines travel from the North Pole to the South Pole of the same magnet through the adjacent yoke extension. In terms of design 4, the presence of high permeability yoke sidebar in close vicinity of the magnets effectively creates additional magnetic circuits that help the flux lines to travel further and couple with the rebar. Further investigation of design 4 involves variable gap between the magnet and its nearby side extension. The resultant force from variable gap from 0 – 50 mm demonstrated in Figure 3-18 shows that the adhesion force increases steadily until 25 mm gap and decreases subsequently. At gaps bigger than 50 mm, the force achieved is equal to design 2. This denotes that gaps of over 50 mm, the additional magnetic circuits between the magnet and the nearby side extension disappear and the yoke design 4 behaves as the design 2. Although, design 4 provides the maximum adhesion force of 77.76 N out of all four designs, having the side extensions have reverse effect on the ratio of η. Due to that reason, yoke design 1 is considered for future designs.

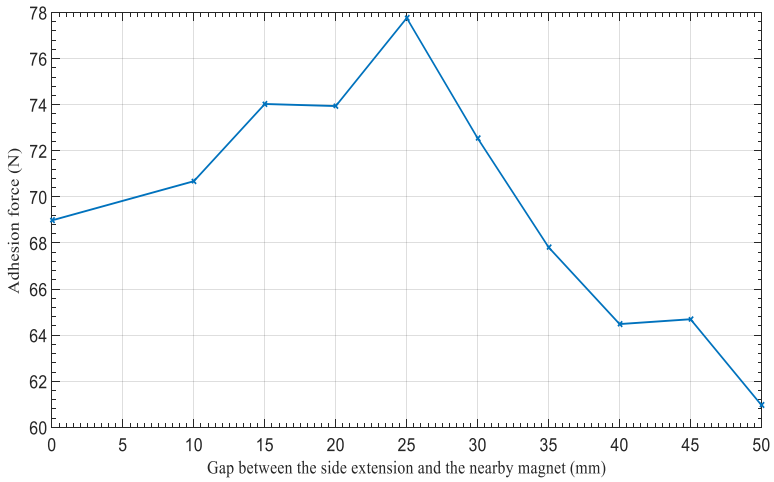

Figure 3-18. Adheison force pattern for the design 4.

3.4.5 Optimization of the magnetic circuit coupling

For the previous sets of simulation, North-South (NS) configuration using two magnets was implemented. Such configuration essentially creates one magnetic circuit travelling from the North Pole of one magnet to the South Pole of the other magnet. Yet

for deeper magnetic flux penetration and higher adhesion force, layouts built of more than two magnets could be considered. As multiple magnets are present in close proximity so, the coupling between them will influence the adhesion force performance. In order to identify the optimum magnets arrangement, several layouts as presented in Figure 3-19 were investigated. The yoke thickness was 20 mm and the magnets dimension used were 50×50×10 mm. The distance between the magnets was set to 50 mm which is the optimum level determined from the previous simulations. The measured adhesion forces for each layout at different concrete covers is illustrated in Figure 3-20.

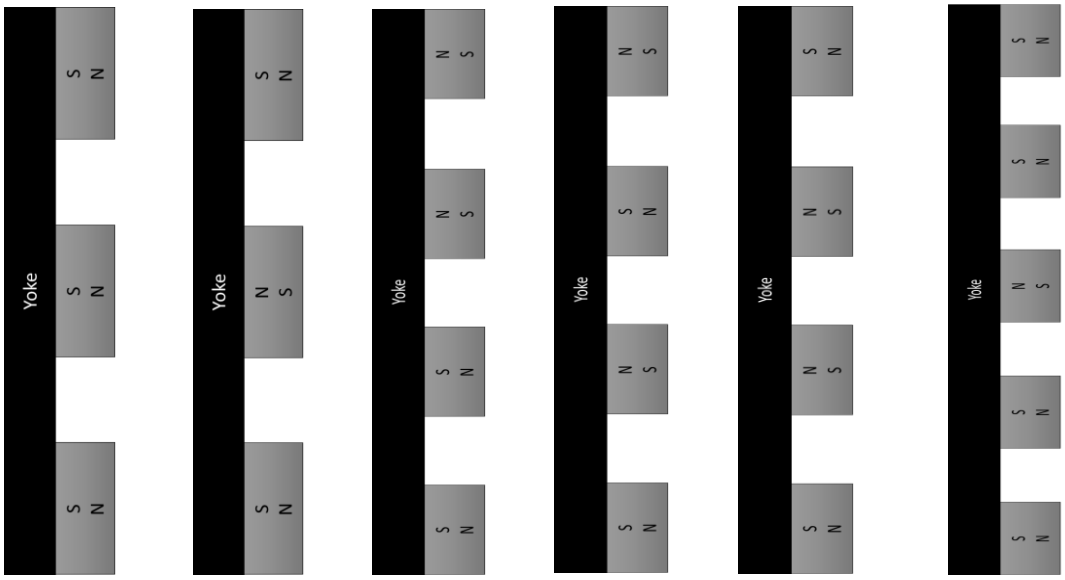

Layout 1 (NNN) | Layout 2 (NSN) | Layout 3 (NNSS) | Layout 4 (NSNS) | Layout 5 (NSSN) | Layout 6 (NNSNN)

Figure 3-19. Investigated magnets layouts.

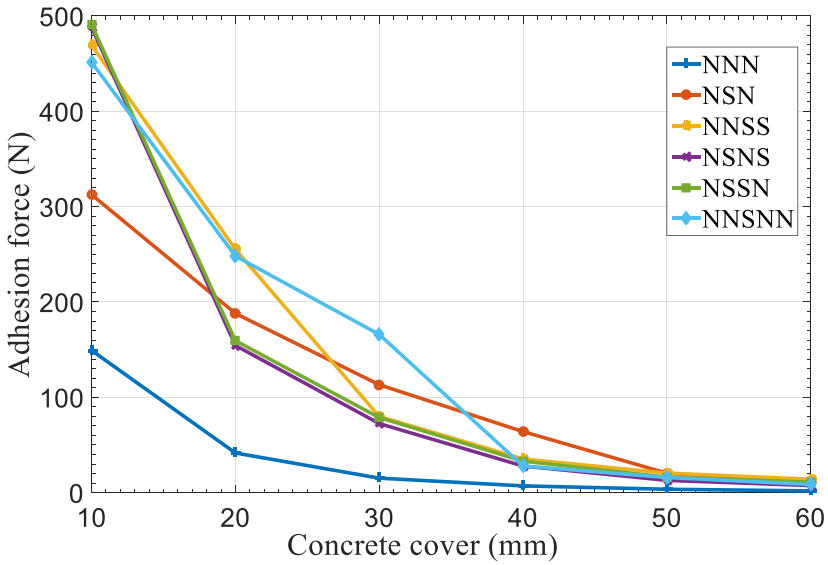

Figure 3-20. Simulated adheison force for different magnet layouts.

The results demonstrate that layout 4 (NSNS) and layout 5 (NSSN) produce the maximum adhesion force of 488.18 N at shorter concrete cover of 10 mm. However, they experience the highest rate of fall in force as the concrete cover increases to 20 mm. At 30 mm cover, layout 6 (NNSNN) achieves the peak force of 165.94 N which also suffers sharp force reduction of approximately 137 N as the concrete cover is increased to 40 mm. Moreover, the concrete cover of 30 mm and higher, layout 3, 4 and 5 yield the same level of adhesion force. Out of all the arrangements, layout 1 (NNN) that consists of identical magnetic poles of the adjacent three magnets facing the rebar generates the lowest level of adhesion and therefore, can be disregarded. Layout 2 is found to be the optimum coupling structure that offers reasonable adhesion force level of 64 N at concrete cover as high as 40 – 45 mm and in this case, adding one extra magnet on the system creates two separate magnetic circuits and increases the overall adhesion force. Furthermore, layout 6 can be also be considered as it provides highest adhesion force at concrete cover of up to 35 mm. Comparisons between the layout 2 and the layout 6 show although layout 6 produces higher adhesion force and the ratio, η than layout 2 at lower concrete cover. As the cover increases, the variance in the ratio, η between the two becomes smaller as represented in Figure 3-21. Also, the rate at which adhesion force falls as the rebar distance increases is lower for the layout 2 than the layout 6. In case of the layout 6, having two same poles closer to each other ensure that magnetic flux lines travel a longer distance to meet the opposite pole compared to the layout 2 as shown in Figure 3-22. Therefore, layout 6 would be more applicable in cases where magnetic coupling with more than one layer of buried rebars are desired. On the other hand, if the rebars are located at a lower depth then layout 2 would be more considerable for lower overall weight of the robot. Moreover, layout 2 results in uniform distribution of magnetic flux lines which is also significant when it comes to balanced magnetic circuit.

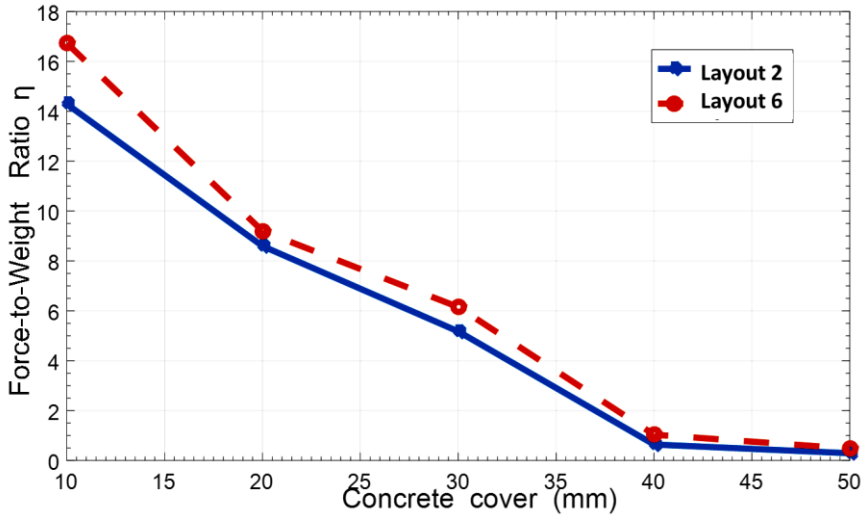

Figure 3-21. Comparison of adhesion force-to-weight ratio, η between layout 2 and layout 6 for different concrete cover.

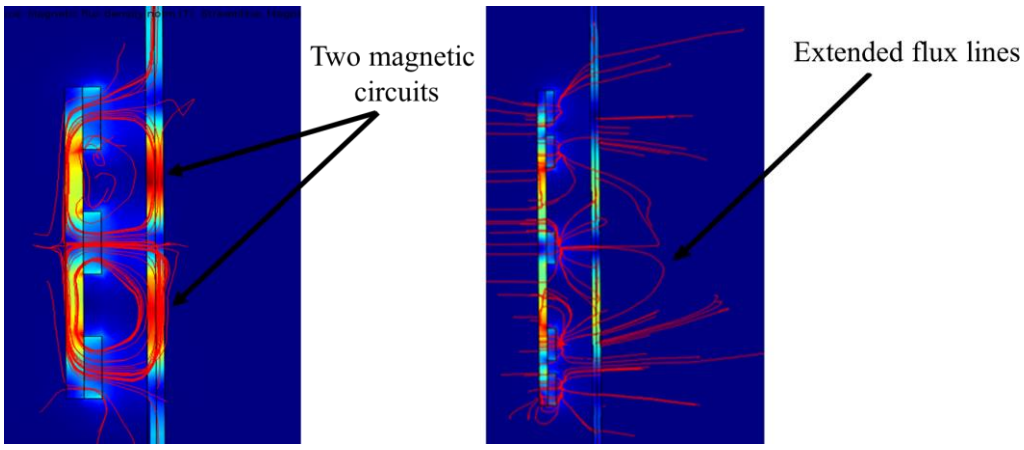

Figure 3-22. Two magnetic circuits created by the layout 2 and the extended flux lines created by the layout 6.

3.4.6 Implementation of multiple yokes

As the concrete structures are reinforced with mesh of the rebars therefore, implementation of multiple yokes can increase the attraction area and ultimately generate higher adhesion force. To investigate is criterion further, models are built using two layouts as in Figure 3-23 below and the adhesion force is measured for different distances, Y_d amongst them. Rebar meshing of 50 mm × 50 mm and 30 mm concrete cover is considered for this setup.

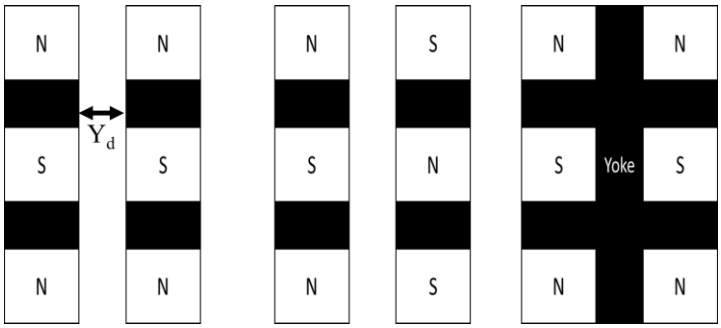

Structure 1 Structure 2 Structure 3

Figure 3-23. Three strucutres investigated for multiple yoke implementation.

Results in Figure 3-25 demonstrate that, structure 1 provides higher adhesion force compared to structure 2 when the distance between yokes is marginal. At 5 mm distance, structure 1 generates 211.7 N of force compared to 150.3 N for structure 2. The adhesion force decreases as the distance is increased to 50 mm. At distances higher than 50 mm, both structures generate exactly the same amount of adhesion force. Moreover, an increase of adhesion force to 188 N is seen at 60 mm and 80 mm of distance between the yokes. At these two points, both of the yokes for structure 1 and 2 are located right in front of the vertical rebars. The hot spots shown in Figure 3-24 illustrates the concentration of magnetic flux along two separate vertical rebars as each couples with them. Moreover, the adhesion force achieved from mounting six magnets on one yoke in NSN-NSN formation as structure 3 indicates that at smaller Y_d value of only 5 mm, achieved force is 50.6 N higher than using two separate yokes. However, as Y_d increases, one yoke system yields lower adhesion force compared to two yokes system. At 25 mm of $Y_{d,}$ the adhesion forces are 100.67 N and 160.23 N for one yoke and two yokes systems respectively and the change in force is marginal at higher Y_d values. This behaviour denotes that, at Y_d values of 25 mm and above, the first set of NSN module do not interact with the second sets of NSN module and there is no change in adhesion force. Considering the final output adhesion force, two yokes system with NSN-NSN formation is chosen as the optimum.

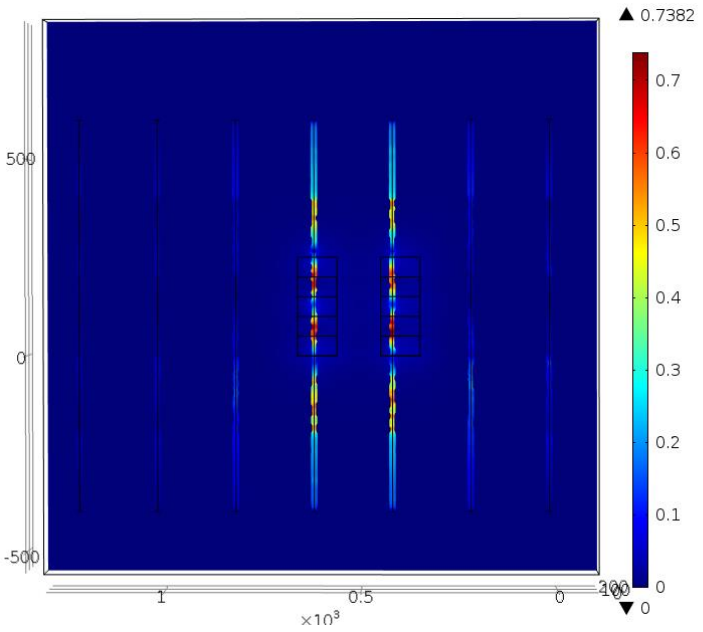

Figure 3-24. Magnetic flux concentration along two separate rebars using strucutre 1.

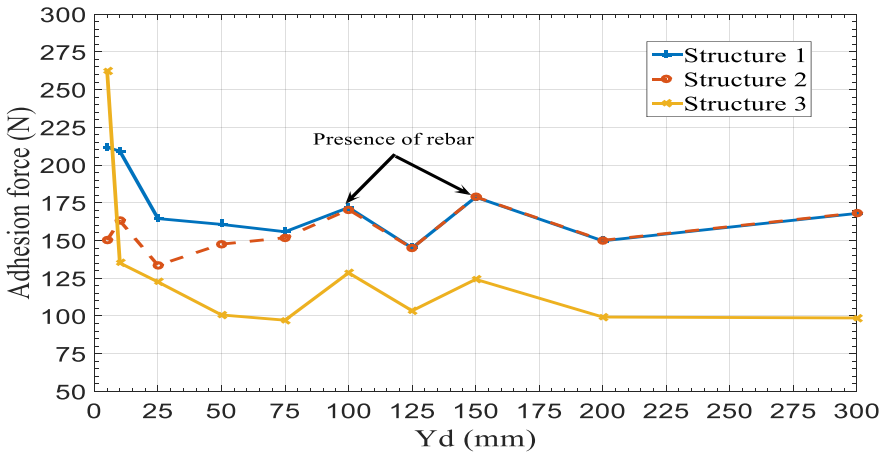

Figure 3-25. Adhesion force comparison between the three structures.

3.4.7 Effects of the rebar meshing

Different spacing between the rebars is used depending on the concrete structure. The adhesion force for a rebar mesh with different spacing is presented here. In the simulation model, the distance between horizontal rebars is set to 150 mm which is the European standard and the distance between the vertical rebars are varied from 50 mm to 200 mm while keeping the concrete cover constant at 30 mm.

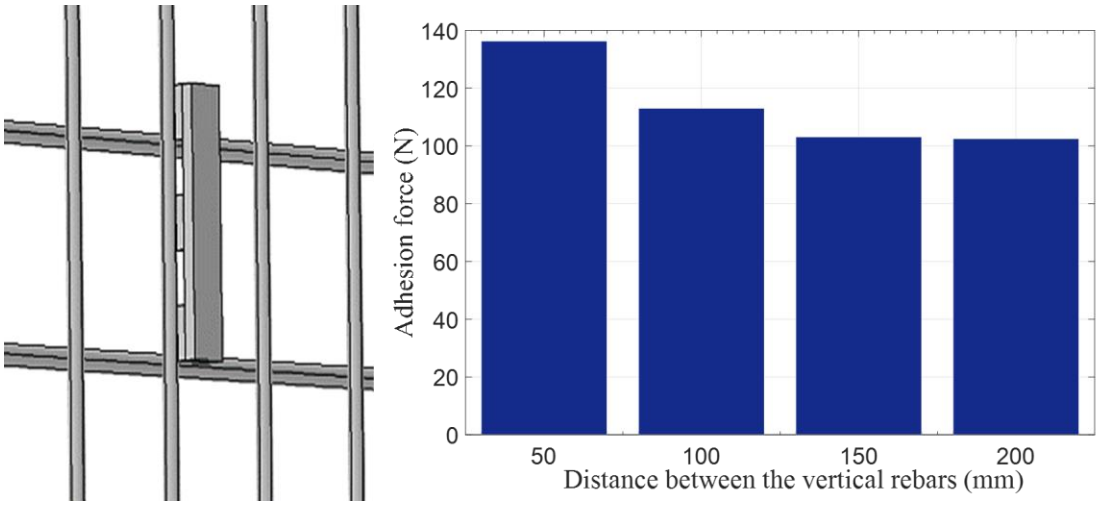

Figure 3-26. Simulation setup of rebar mesh and resultant adhesion force at different mesh settings.

The simulated adhesion force measurements in Figure 3-26 show that, the adhesion force is increased as the distance between the vertical rebars is reduced. This is because in case of two rebars close together, magnetic flux can act on a larger attraction area and generate bigger force compared to only a single rebar. In case of safety critical infrastructures, the rebars are meshed at a distance of 50 mm for greater strength and longevity and this novel adhesion mechanism is much suited to those environments to generate higher adhesion force.

3.4.8 Manoeuvring capability

The dense meshing of the rebars can offer the feasibility of greater robot's manoeuvrability on a vertical plane. To demonstrate that, the adhesion module arranged as structure 1 was rotated full 360 degrees along its centre of gravity and the adhesion force was measured at 300 intervals. Figure 3-27 shows the results and it can be seen that the adhesion force is at their lowest point of 148 N when the yokes were rotated 90^0 and 270^0 from its initial upright position. From this it can be said that, this two yokes based novel adhesion module can offer robots the freedom to turn 360^0 and maintain adhesion force down to 140 N. If only one yoke is deployed, the lowest adhesion force of 36.23 N is achievable. Furthermore, the flux density norm graph in Figure 3-28 indicates that, during the process of rotation, the adhesion module bonds with separate layer of vertical and horizontal rebars. Therefore, the adhesion force varies with the rotation angle and the number of rebars involved.

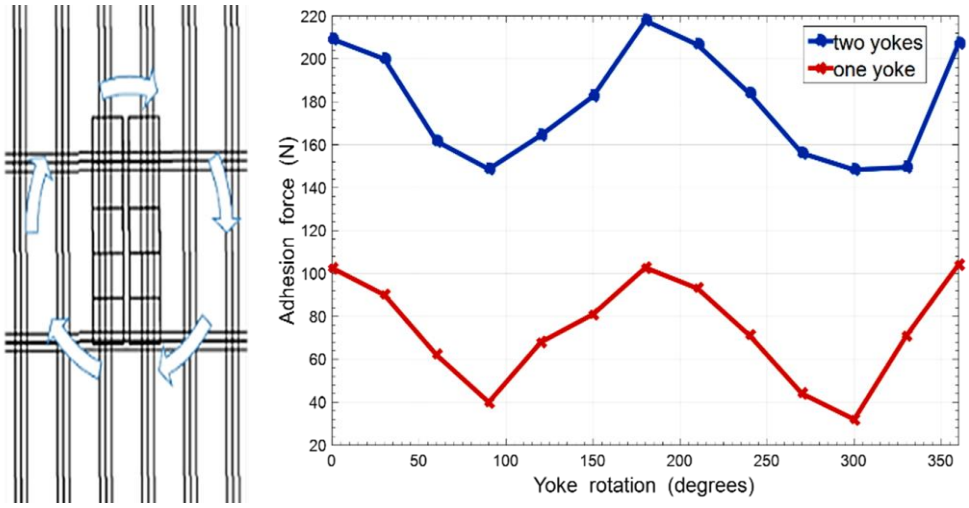

Figure 3-27. Comparison of adhesion forces at different rotational positions of adhesion modules consisting of one and two yokes.

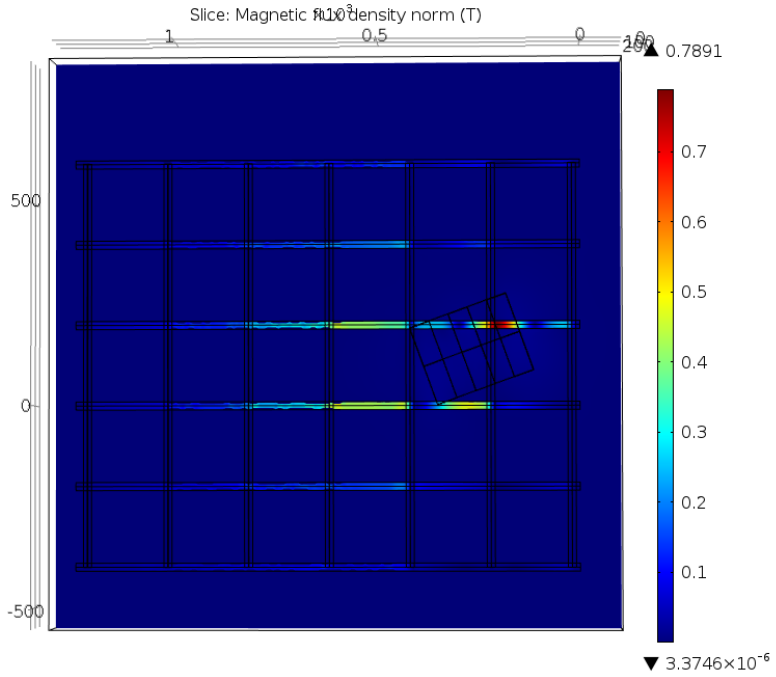

Figure 3-28. Flux density norm at different rotations of the adheison module.

3.5 Chapter summary

This chapter presents an overview of the robot's operational environment where the robot is expected to climb concrete surfaces that are reinforced with rebars located as deep as 45 mm. The force analysis reveals that for safe operation, the robot must avoid slipping, capsizing and rolling over. The required force to avoid those limitations depends mostly on the robot's body weight, dimension and the locomotion. The robot weight must be as low as possible to avoid slipping while a large distance between the robot's front wheels and the rear wheels can ensure capsizing avoidance.

Furthermore, parametric analysis of the adhesion module indicates that the distance between the two nearby magnets is critical in obtaining a balanced magnetic circuit and the distance must not be more that the length of the magnet used. Also, a thicker magnet rather than a wide magnet is highly efficient in terms of maximizing the adhesion force. Secondly, a yoke can concentrate the magnetic flux towards the rebars and reduce flux leakage on the opposite side. Having a yoke with side extensions can achieve marginally higher adhesion force than a flat shaped yoke. However, the flat yoke offers more consistent adhesion force at different concrete cover at higher weight ratios, η. The analysis also identifies that having two adhesion modules located at a small gap between them with magnets arranged in NSN layout can significantly maximize the resultant adhesion force and highly applicable for surfaces with 50×50 mm grid rebar meshing. The rebar meshing also supports the manoeuvring capability of the robot on a vertical surface.

Chapter 4. Development of a prototype climbing robot

This chapter describes the development process of a prototype climbing robot. Optimization of design parameters are achieved by carrying out experiments using a purpose built test rig. The climbing performance of the prototype robot is verified on both ferrous and concrete surfaces. The chapter is outlined as follows:

4.1 Overview

This chapter emphasizes on the design and development of a prototype climbing robot. The primary motivation is the experimental validation of the results obtained from the simulations. To achieve that goal, experimental setup using bespoke test rig is carried out and the results are discussed in this chapter. Adhesion modules consist of multiple yokes of various thicknesses are examined and evaluated against the simulation results. Design parameters such as the distance between the nearby magnets, yoke thickness, rebar grid meshing etc. are critically examined in test conditions in order to establish the optimum design dimensions.

Furthermore, the prototype climbing robot's performance is assessed considering its real life application. The tests are carried out on a vertical plate taken from a ship hull as well as on a reinforced concrete column of a residential building. The final adhesion module design is adopted to modify an existing climbing robot to be used for laser cutting task. The experiment results set the performance benchmark of the climbing robot and the technical feasibility of implementing permanent magnet based adhesion mechanism for reinforced concrete structures.

4.2 Prototype robot design

For performance evaluation, a magnetic adhesion system consisting of N42 grade rare earth neodymium magnets is built and attached to a prototype climbing robot. The measured dimensions of the whole system are: robot length = 360 mm, robot width = 210 mm, height of the centre of gravity = 15 mm. Wheels are chosen as preferred locomotion as they can provide higher velocity and manoeuvrability compared to other locomotion techniques as discussed in the design review section. Each wheel is independently driven using servo motors capable of delivering 2.16 Nm of torque at 30 rpm. Wheels made of rubber polyurethane layer are used for higher friction and the wheel's outer diameter is measured to be 63 mm. This wheel size is sufficient enough to keep the air gap between the magnet face and the concrete surface at 2 mm as a small gap increases the adhesion force significantly. Moreover, the ability to pass obstacles has been considered to be of secondary importance at this stage since the aimed climbing surfaces are closely uniform. The robot's net body mass is 2.23 kg and 3.68 kg when 5 mm and 15 mm thick yoke is used respectively. Therefore, the required force for sliding avoidance can be obtained as 46 N and 76 N for 5 mm and 15 mm yoked

robot respectively by using Equation (3.6) and Equation (3.8) when acceleration, a is 0.5 ms^{-2} and wheel's friction coefficient, μ is 0.5.

The robot is equipped with four strain gauges based load cells capable of measuring up to 1500 N each. Strain gauges are affixed to the beam at the top and bottom to measure changes in the beam due to deflection. Where they sense very small deflections in the metal caused by the load being applied to the cell, the difference in the output signal before and after the mass was placed on the platform is read, interpreted and displayed. Each load cell is mounted underside of the robot chassis and the adhesion module is suspended freely in the loading platform using extensions. As the adhesion module presses toward the buried rebar, it applies force in the loading area of each load cell. The load cells produce a low-voltage milli-volt (mV) relative to the force applied. An operational amplifier HX711 is used to amplify the voltage and AVR microcontroller based 10-bit analogue to digital module is used to convert the signals to numerical values and displayed on computer screen using serial data transmission system. A block diagram of the robot assembly and the prototype robot is given in Figure 4-1. The adhesion module is suspended freely on top of the load cell's loading area, but is secured on the place to avoid displacement using additional screws which are not shown in the block diagram.

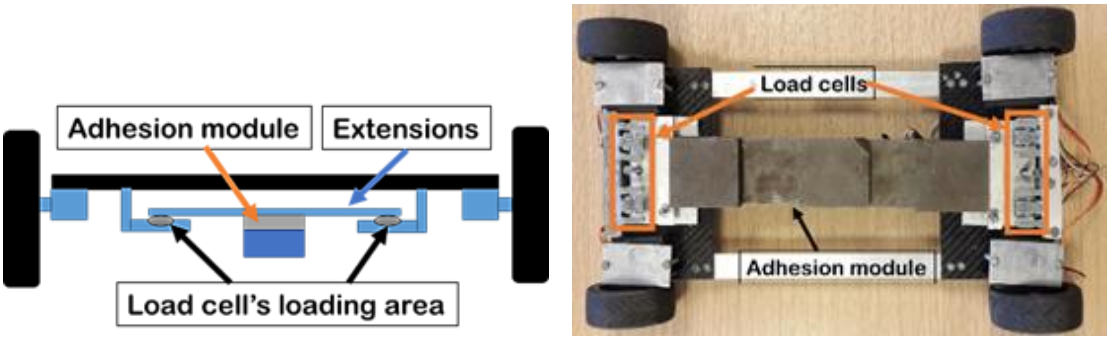

Figure 4-1. Block diagram of the robot assembly and bottom view of the built prototype robot.

The entire robotic system is powered by four 1.5 V Lithium-ion Polymer (Li-Po) batteries that supply enough operating voltage for the motors and force measurement unit. As a result, the robot is totally umbilical free and Bluetooth wireless communication system provides real time data transmission system from the control units to the Matlab environment for data analysis. An operator can access the control unit data as well as navigate the robot from a base station with ease. The total system block diagram is illustrated in Figure 4-2.

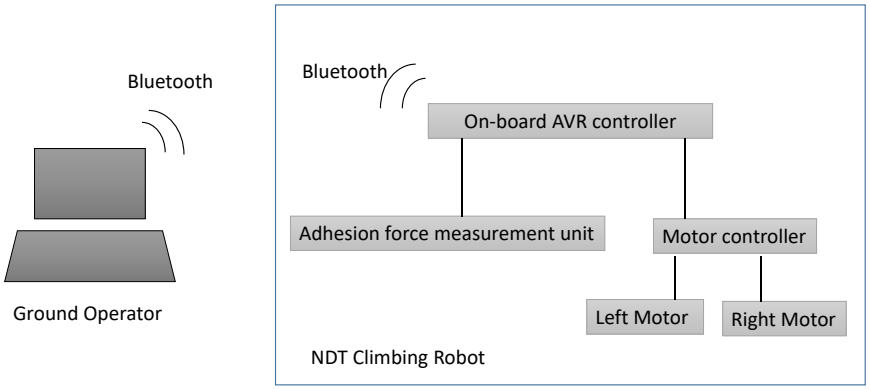

Figure 4-2. Block diagram of the robot's control system.

A testing rig has been constructed to validate the obtained results from simulations. A wooden frame of 1 m in length and 70 cm in height is built. Holes of 12 mm diameter are drilled along the length of the frame as a slot for 12 mm diameter rebars to fit in as shown in Figure 4-3. The distance between the rebars can be varied from 50 mm to 200 mm by slotting the rebars in through different drill holes. This setup is useful to investigate the effect of the nearby rebars on adhesion force. A 30 mm thick wooden plate is also attached to the frame with sliding screws. The distance between the wooden plate and the rebars is variable which will act as the concrete cover. Moreover, this testing rig will be useful to investigate the manoeuvring capability of the robot for different rebar arrangements. Concrete, wood and air have the same magnetic permeability level of 1. Therefore, this wooden frame can emulate the scenario of a reinforced concrete surface with varying concrete covers depending on the structure type [88].

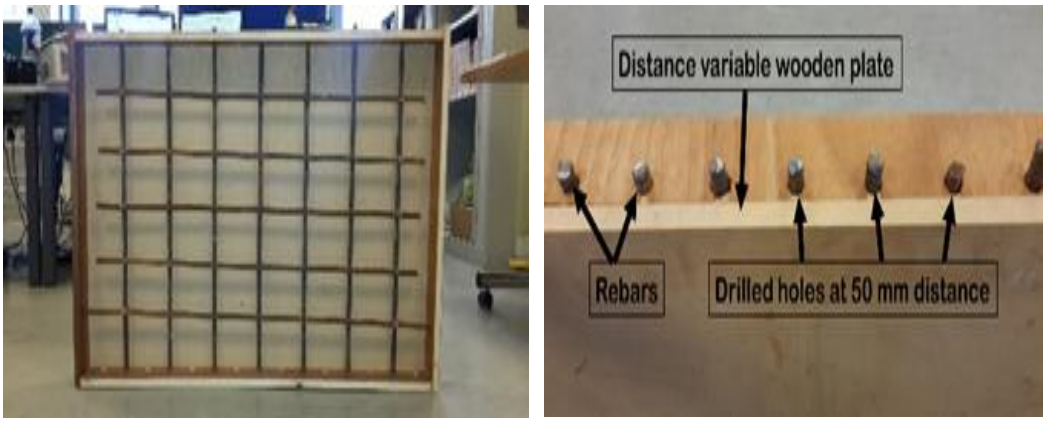

(a) (b)

Figure 4-3. Constructed experimental rig using a wooden frame and steel rebars: (a) front view; (b) top view.

4.3 Performance analysis on vertical ferrous surface

First prototype robot was implemented to scan long weld lines on 10 mm thick vertical ferrous surface cut out from a ship hull. The adhesion module consisted of two N42 grade magnets of 50×50×12 mm dimension arranged in NS layout with 50 mm gap between the magnets. Yokes of 5 mm and 15 mm thickness were used for better comparison. The robot and its other components are seen in Figure 4-4. The adhesion force measurements were recorded for both vertical and horizontal movement of the robot on the vertical surface at 10 mm air gap. An ultra-sound (US) flaw detector was attached with robot as an additional payload to emulate a real life NDT inspection scenario. The US probe together with the robot control unit weigh up addition 1.6 kg. Measurements were taken at six different test points along the height and length of the ship hull segment as shown in Figure 4-5. Performance of the robot was also assessed while transitioning to a 145^0 angled surface. Table 4-1 and Table 4-2 provide the adhesion force measured which account for both with payload and without payload.

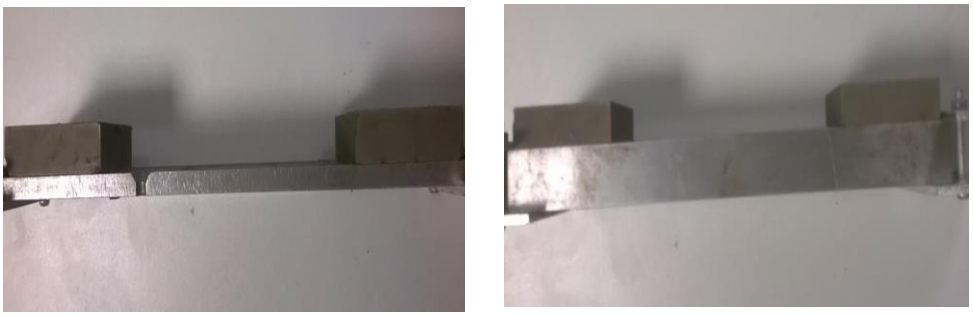

(a)

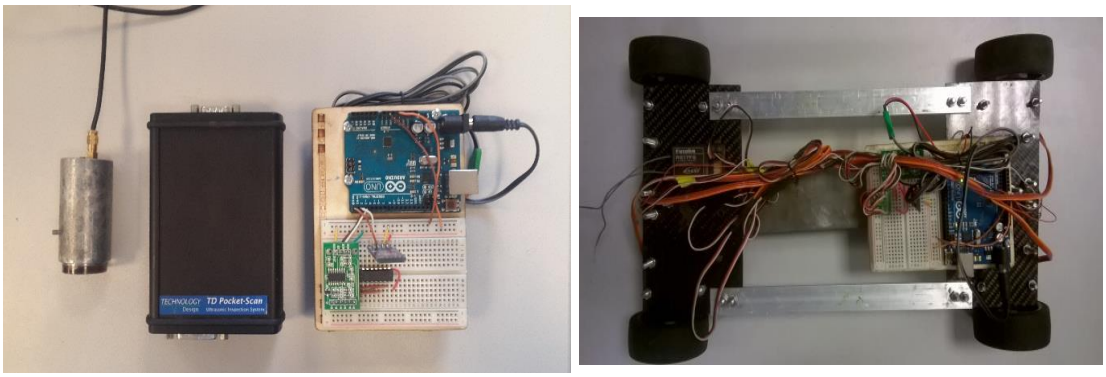

(b)

Figure 4-4. Prototype climbing robot: (a) 5 mm and 15 mm yokes; (b) Elements of climbing robot control system: US probe, US transceiver, Motor and measurement unit control system and the prototype robot (from left to right).

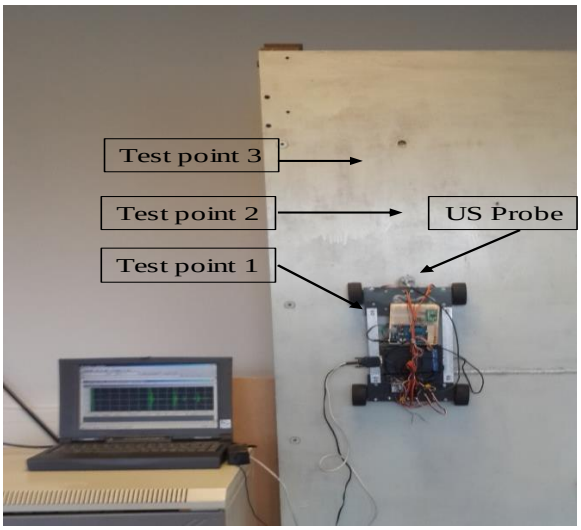

(a)

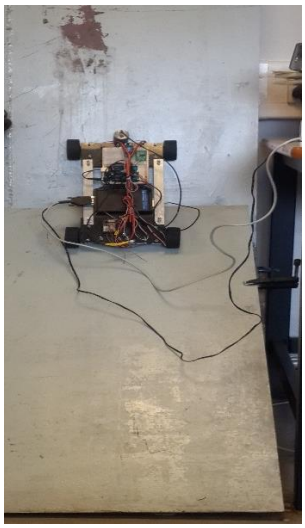

(b)

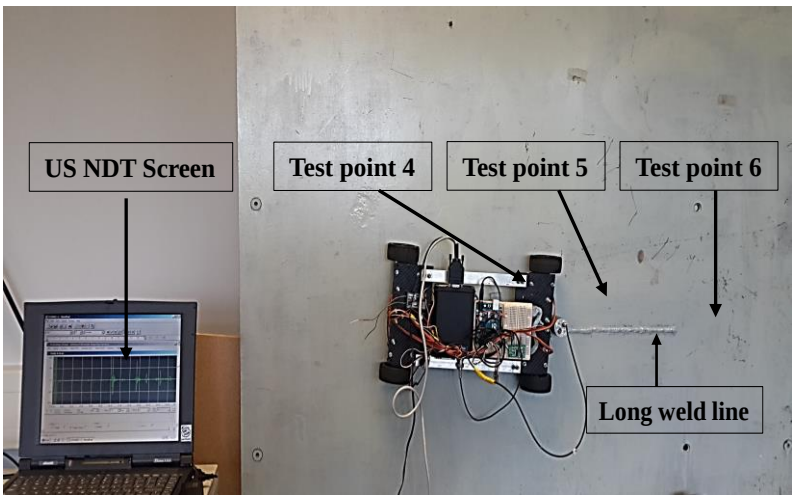

(c)

(d)

Figure 4-5. US NDT using the prototype climbing robot: (a) Robot operating vertically; (b) Robot transitioning a 145^0 angled surface; (c) horizontal navigation for US NDT of a long weld line; (d) Measuring robot's adhesion force at 20 mm air gap with a wooden plate acting as separator.

Table 4-1. Measured adhesion force at 10 mm air gap for 5 mm thick yoke.

	Test Point 1	**Test Point 2**	**Test Point 3**	**Test Point 4**	**Test Point 5**	**Test Point 6**
Without load	203.73	205.47	205.22	205.03	202.22	203.57
With load	192.75	191.13	191.53	193.39	192.24	192.11

Table 4-2. Measured adhesion force at 10 mm air gap for 15 mm thick yoke.

	Test Point 1	**Test Point 2**	**Test Point 3**	**Test Point 4**	**Test Point 5**	**Test Point 6**
Without load	225.58	227.09	227.14	226.05	226.42	226.64
With load	212.59	211.85	211.22	213.27	213.33	212.71

Experimental measurements confirm that using a thicker yoke of 15 mm yields higher adhesion force of 227.09 N compared to 205.47 N for 5 mm thick yoke however, the force-to-weight ratio reduces due to added weight as the yoke thickness is increased. Therefore, a yoke of 5mm thickness is highly recommended to keep the robot weight to a minimum. Moreover, as the vertical climbing surface taken from a ship hull is highly even, the differences between the measured adhesion force at different test points are negligible. The achieved mean adhesion forces are 204.206 N and 226.486 N for 5 mm and 15 mm thick yoke respectively. Also, as the robot carries additional payload of NDT sensor, the adhesion force does not suffer any setback as achieve maximum force with payload is 213.27 N 10 10 mm air gap. A wooden plate of 10 mm thickness has been introduced to increase the air gap to 20 mm and adhesion force is measured to be 176.73 N. Additionally, all the measurements closely follow the simulations obtained as shown in Figure 4-6 and notably the experimental results verify the improved efficiency of the adhesion module using unique magnet arrangement on a flux concentrator compared to other systems found in the literature as given in Table 4-3. As determined in chapter 3 (section 3) that the robot can safely carry half the adhesion force it can generate, the robot is expected to carry a maximum payload of 100 N or 10 kg.

Table 4-3. Comparison with systems found in the literature.

	Ref [5]	**Ref [6]**	**This work**
Robot weight (kg)	30	18	3.83
Maximum adhesion force (N)	1400	667	204.206
Force-to-weight ratio	4.76	3.77	5.43
Adhesion mechanism	Magnetic	Magnetic	Magnetic
Locomotion	Wheel	Track	Wheel

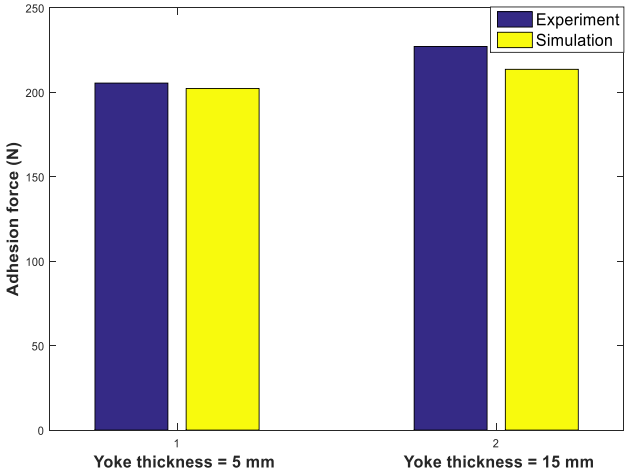

Figure 4-6. Experiment vs Simulation results for 5 mm and 15 mm thick yokes at 10 mm air gap.

4.4 Performance analysis on vertical concrete surface

Next few sets of experiments are carried in order to establish the feasibility implementing the permanent magnet based adhesion module in concrete surface climbing operation. The tests are carried out on the test rig as well as field testing are considered for the performance assessment.

4.4.1 Magnet layout

In order to obtain better comparison between different designs, adhesion modules were built in four distinctive layouts as shown in Figure 4-7 using 50×50×10 mm sized magnets and 5 mm thick, 50 mm wide and 350 mm long cast iron yokes. Experiments were carried out using the test rig for 30 mm concrete cover and rebar grid meshing of 50×50 mm. Adhesion force was recorded in three different points and the mean values are considered. Layout 1 with six N42 grade magnets arranged in the same polarity facing the rebar generates 98.12 N of adhesion force. The whole module weighs 2 kg net. Layout 2 incorporates only 4 magnets in NSSN arrangement that weighs 1.5 kg and generates 79.84 N of force. Using two less magnets results in reduction of only 18.28 N force compared to layout 1 however, layout 2 offers higher value of η at less system weight. Layout 3 comprises of three magnets in NSN polarity that achieves 88.45 N of force. However, if the magnet thickness is doubled to 20 mm and other settings are kept identical, NSN configuration generates the highest adhesion force level of 174.67 N at 30 mm concrete cover. This result confirms the behaviour establish during parametric studies that, thicker magnets are more efficient in maximizing the force while NSN coupling configuration the ideal arrangement layout. Moreover, there

is a difference of 0.5 kg in additional mass for thicker magnet based system compared to its predecessor, the adhesion force increases by approximately 97%. These experimental results reiterate the conclusions drawn from the simulations and NSN configuration has been selected for final design procedure. Table 4-4 summarizes the experimental results for each layout examined.

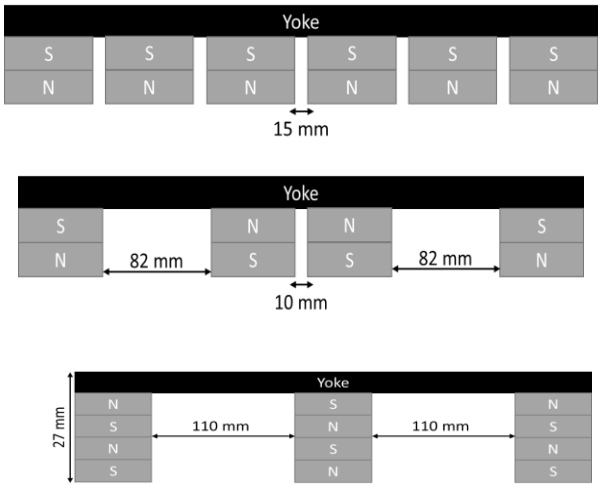

Figure 4-7. Layouts of the investigated configurations.

Table 4-4. Summary of experimental results.

	NNNNNN	**NSSN**	**NSN**	**NSN(double)**
System mass (kg)	2	1.5	1.23	2
Adhesion force (N)	98.12	79.84	88.45	174.67
Force-to-Weigth ratio, η	5	5.43	7.33	8.91

4.4.2 Distance between the magnets

Having selected the layout 3 for final design, effect of the distance between the magnets was investigated. The distance, M_d between 50×50×10 mm sized magnets mounted on 3 mm thick yoke as shown in Figure 4-8 was varied from 20 mm to 120 mm. At distances smaller than 20 mm, the measurements could not be taken as it was found difficult to keep the magnets in place due to high attraction force between two nearby magnets facing each other with same polarity. The results given in Figure 4-9 highlight that, the adhesion force reaches its peak of 102.53 N at M_d = 50 mm after a gradual increase from initial 20 mm point and that is followed by a sharp dip in adhesion force as the distance increases to 120 mm. Therefore, at 50 mm distance, two magnetic circuits created by the NSN configuration obtain balanced form of magnetic flux

distribution. At 20 mm distance, the attraction area is so small that the module achieves only 70.15 N of force. Likewise, at distances greater than 50 mm, the interaction between the magnets starts to diminish and the magnetic circuits disorient which describes the fall in adhesion force at intermediate distance bigger than 50 mm. The important feature is the ratio, η that decreases over the increased distance. This experiments identified the critical distance between the magnets to be 50 mm which is equal to the magnets length.

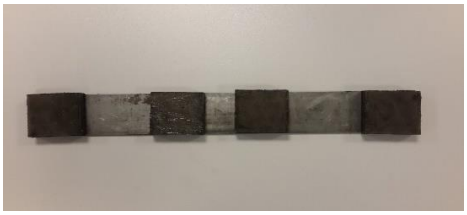

Figure 4-8. Magnets arranged on the yoke.

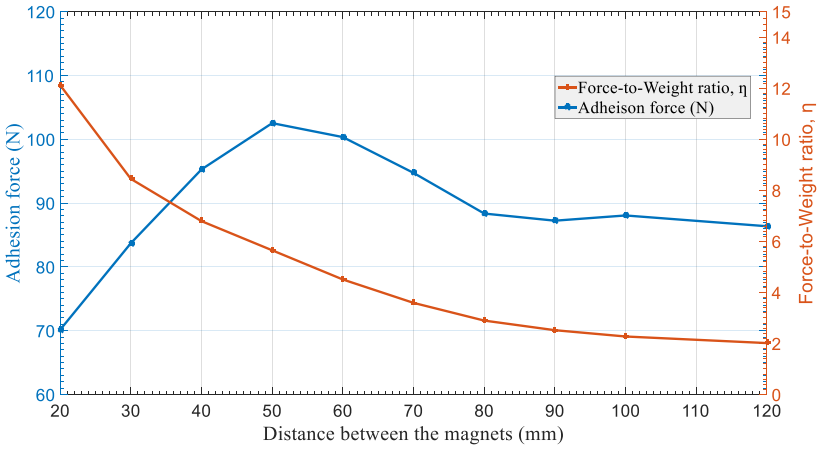

Figure 4-9. Adhesion force at different values of M_d.

4.4.3 Yoke thickness

Having established the optimum coupling structure and the intermediate between distance of the magnets, yoke thickness was the next parameter to be investigated. Five cast iron yokes of 3 mm, 5 mm, 10 mm, 15 mm, 20 mm and 25 mm thick were selected for testing as illustrated in Figure 4-10. The results given in Figure 4-12 confirm that, higher adhesion force can be achieved by implementing thicker yoke. The saturation point is found to be thickness of 15 mm after which the force does not experience any significant rise even if the yoke thickness is increased. For 3 mm thick yoke, the measured force is 102.53 N which increases by 41% to 144.78 N for 15 mm thickness. There is no more significant rise in adhesion force to be recorded as the yoke gets thicker such as at 20 mm thickness, the force increases by only 9.39 N and remains the

same subsequently. Instead, the weight ratio, η graph in Figure 4-12 emphasizes that the ratio falls dramatically from 10.88 for 3mm thickness to 9.01, 7.32 and 5.78 subsequently. However, the rate of fall at 15 mm and 20 mm thickness is lower than the previous case. This trend denotes that the efficiency of the adhesion module reaches its peak as the yoke thickness is increased over 15 mm. In order to keep the system mass to a reasonable level, optimum thickness of yoke is selected to be 15 mm. Comparing the experimental adhesion force data to simulations results however, indicates a large variance between them at low yoke thickness level but are in agreement at thickness level of 20 mm and higher. Nonetheless, the changes in adhesion force pattern are in synchronization between these two and differences could be pointed to the fine meshing of the 3D geometry in the FEA simulation setup.

Figure 4-10. Yokes of different thickness used for experiments.

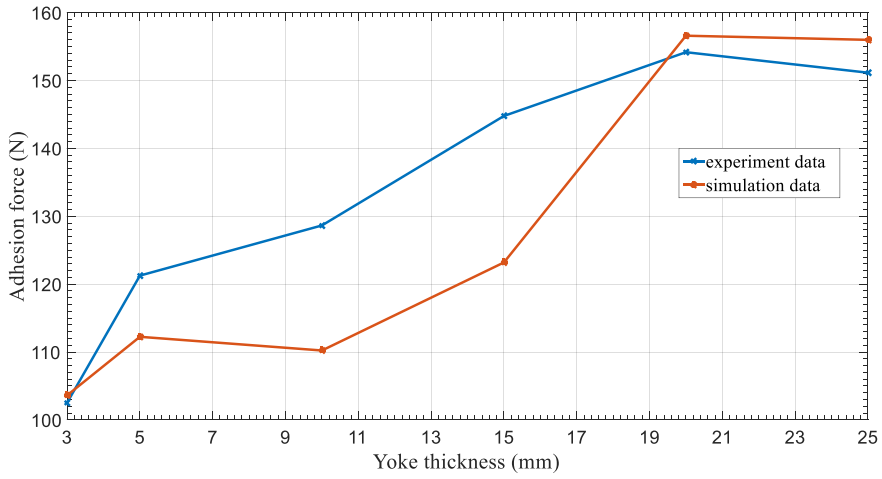

Figure 4-11. Experiment vs Simulation results for different thickness of yoke.

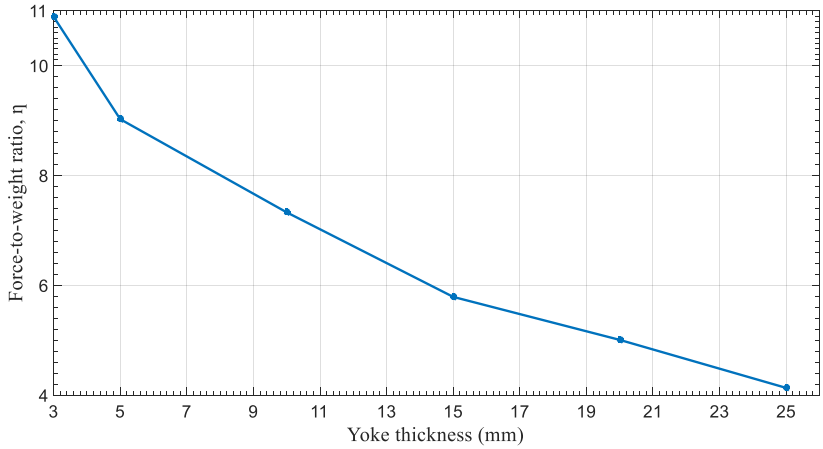

Figure 4-12. Experiment results for Force-to-Weight ratio, η.

4.4.4 Rebar grid meshing

This experiment investigates the effects of rebar grid meshing on the resultant adhesion force. Experiments were carried out using one yoke unit of 15 mm thickness with magnets in NSN configuration while the adhesion force was measured by changing the gap between the vertical rebars for 50×50 mm, 100×50 mm, 150×50 mm and 200×50 mm meshing. The setup of the experiment is shown in Figure 4-13. The robot was positioned such that the adhesion module was aligned face-to-face with a vertical rebar. The robot's position was not changed while the rebar mesh settings were changed. Results shown in Figure 4-14 suggest that when the rebars are densely meshed at 50×50 mm, highest adhesion force of 178.5 N could be achieved. In this case, the adhesion module can attract the front rebar as well as the adjacent vertical rebars located on its left and right side as shown in the colour map in Figure 4-15 acquired from the FEA software. As the distance increases to 100 mm, the module is only coupled with the front set of rebar and the next set of rebars are further apart. As a result, they do not couple with adhesion module unit to maximize the force. At this stage, the adhesion force is 144.64 N. A further increase in the distance has no effect on the adhesion force which stays at an average value of 144 N throughout.

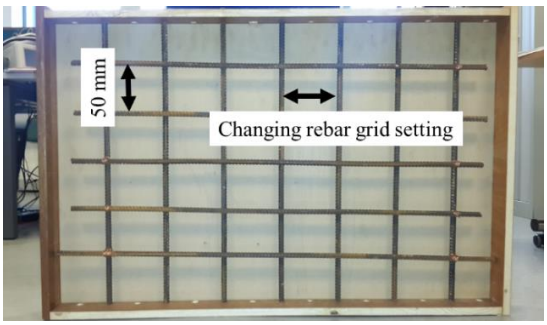

Figure 4-13. Experimental setup to investigate the effect of rebar meshing.

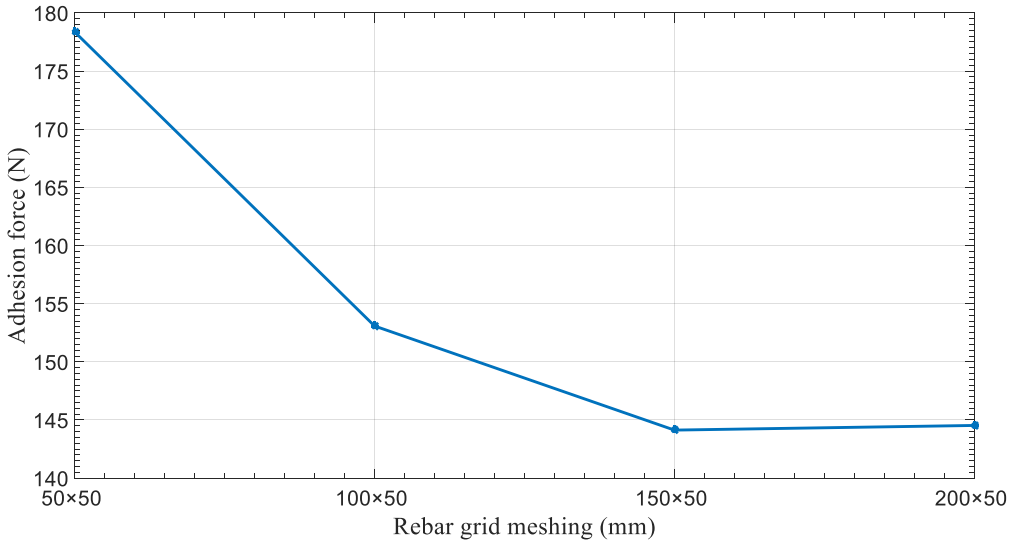

Figure 4-14. Measured adhesion force at different grid meshing.

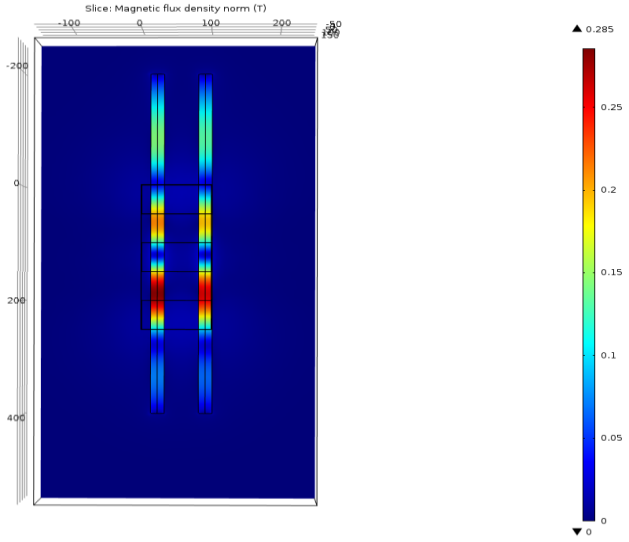

Figure 4-15. Concentration of magnetic flux along two separate vertical rebars.

4.4.5 Turning capability

For testing of rotational movements, the robot was rotated full 360^0 along its centre of gravity and the resultant force was measured for different settings of rebar mesh. Figure 4-16 shows the respective results and according to that, for 50×50 mm meshing, the adhesion force fell to a minimum mean value of 118 N at 30^0, 60^0, 120^0, 240^0, 300^0, and 330^0 of rotations. In these cases, the adhesion module was not aligned face-to-face with a single rebar and as a result magnetic flux distribution is uneven between multiple neighbouring rebars as shown in Figure 4-17. At 0^0, 180^0, and 360^0 positions, the adhesion module was located above the rebar which helped to maintain a balanced flux distribution and achieve maximum adhesion force of 178 N. Moreover, the adhesion

force achieved by the 50×50 mm meshing during this manoeuvring process was higher compared to other meshing due to the influence of the nearby rebars.

The same pattern in changes of the adhesion force was found for other grid setups where the achievable adhesion force remained the same at different angles. That is because at grid setting bigger than 50×50 mm, the nearby rebars are further apart to influence the adhesion. Also, adhesion forces at 30^0, 60^0, 120^0, 240^0, 300^0, 330^0 of rotations were decreasing at a higher rate with bigger mesh settings. The maximum adhesion force was at the same level of 144 N regardless of mesh settings as the module was aligned with a vertical rebar located in parallel right in front of the adhesion unit at 0^0, 180^0 and 360^0 rotations. Moreover, at 90^0 and 270^0 rotational positions, the adhesion module is aligned in parallel right above a horizontal crossbar. At these positions, the adhesion force rose to the maximum value achieved by the particular rebar setting.

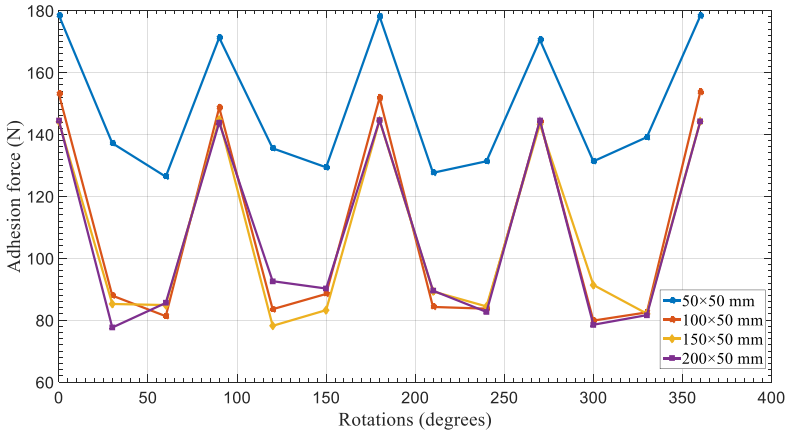

Figure 4-16. Adhesion force at different rotational positions of the robot on the vertical test rig.

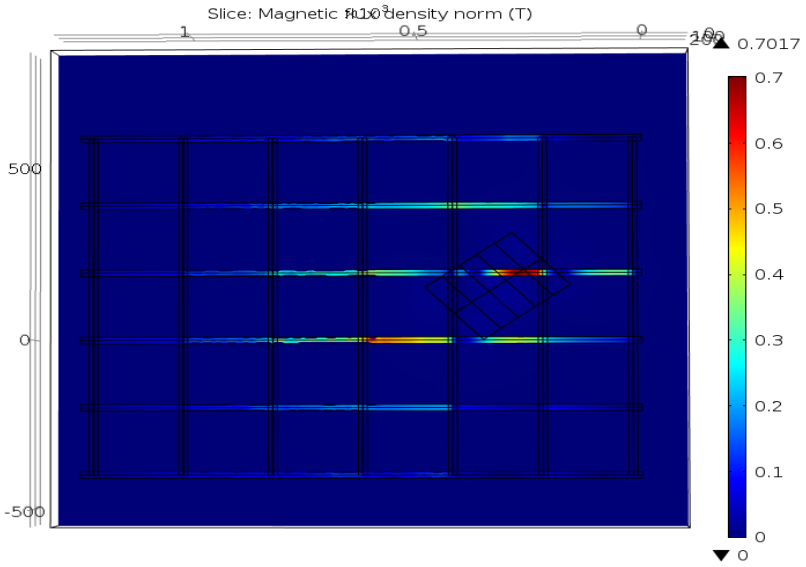

Figure 4-17. Flux distribution along multiple vertical and horizontal crossbars.

4.5 Field testing of the prototype robot

The robot was tested on the concrete column and ceiling of a residential building. The rebars were reinforced in a 50×150 mm meshing at 35 mm depth. The concrete cover was measured using a concrete cover meter. The robot was carrying a Hall-Effect sensor acting as a payload that can identify the presence of a rebar by measuring the changes in surrounding magnetic field. The average adhesion force was measured to be 110.16 N with a maximum value reaching 127.53 N. The mass of the attached Hall-Effect sensor was 1.3 kg. Pictures of the robot climbing surfaces are given in Figure 4-18.

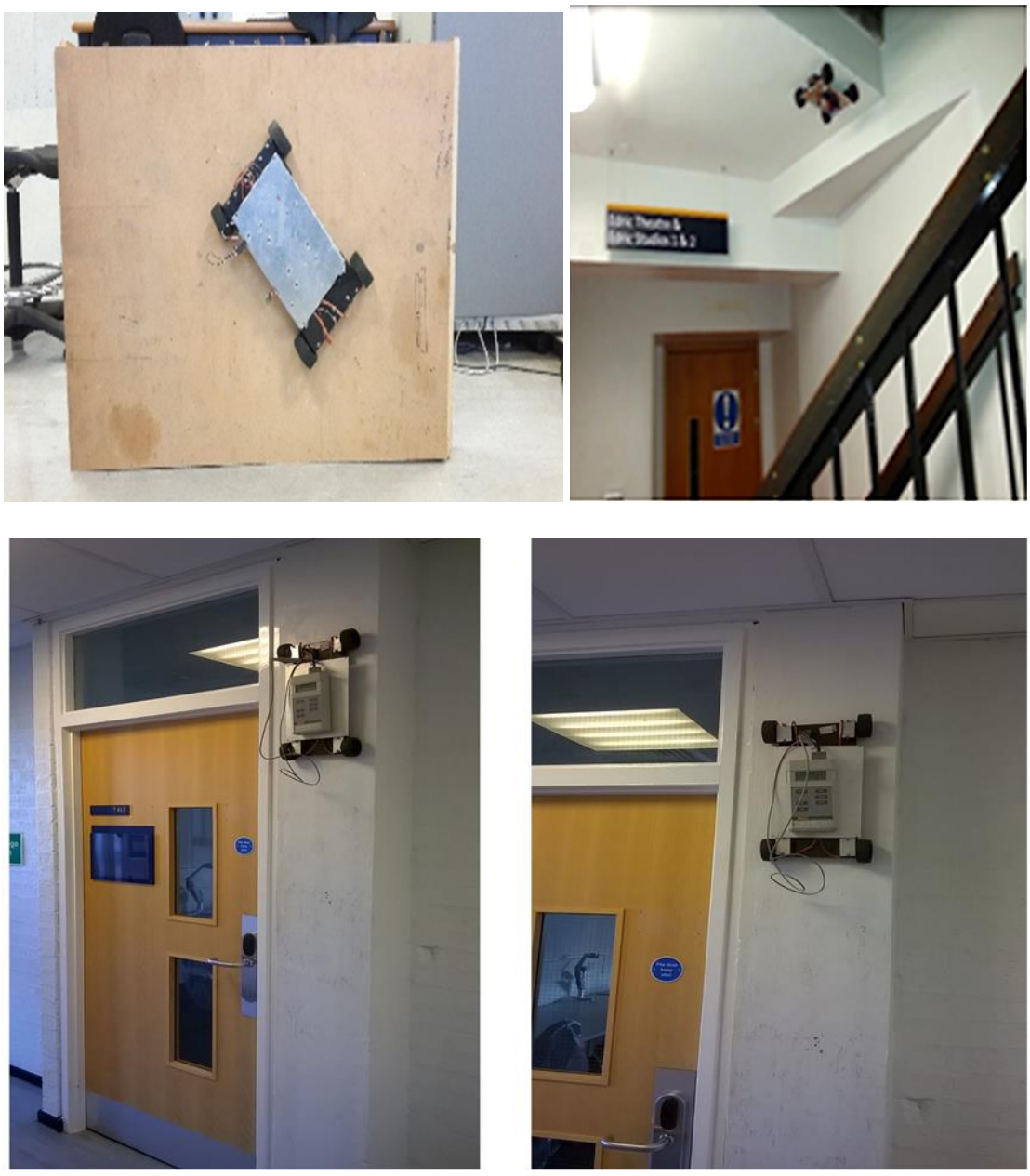

Figure 4-18. Climbing performance of the prototype robot on the test rig, concrete ceiling and columns carrying a payload.

Finally, an adhesion module based on multiple yoke system was built and implemented for a climbing robot to be deployed in industry standard laser cutting assignment. The adhesion module consists of three separate yoke units with magnets of 50×50×20 mm dimension mounted on a 15 mm thick high permeability cast iron yoke. The distance between the yokes are 30 mm. Although, simulation results indicate that marginal distance between the yokes offers the highest level of force, however, the repulsion force between the same polarity of the adjacent magnets are so high that a gap smaller than 30 mm is not possible without specialized machinery. The generated adhesion force of the unit was measured using the load cell based force measurement unit that records a high attraction force of 901.53 N action on a vertical steel surface only 5 mm thick located at 35 mm distance which is given in Figure 4-19. The transitioning procedure of the robot from an inclined surface to a vertical surface as well as the laser cutting process are illustrated in Figure 4-20. The laser cutter weighs 17 kg and the robot is controlled manually using 5 A current motor controller. All of these achieved results verify concept of a novel adhesion module developed in this research that offers high payload and efficiency.

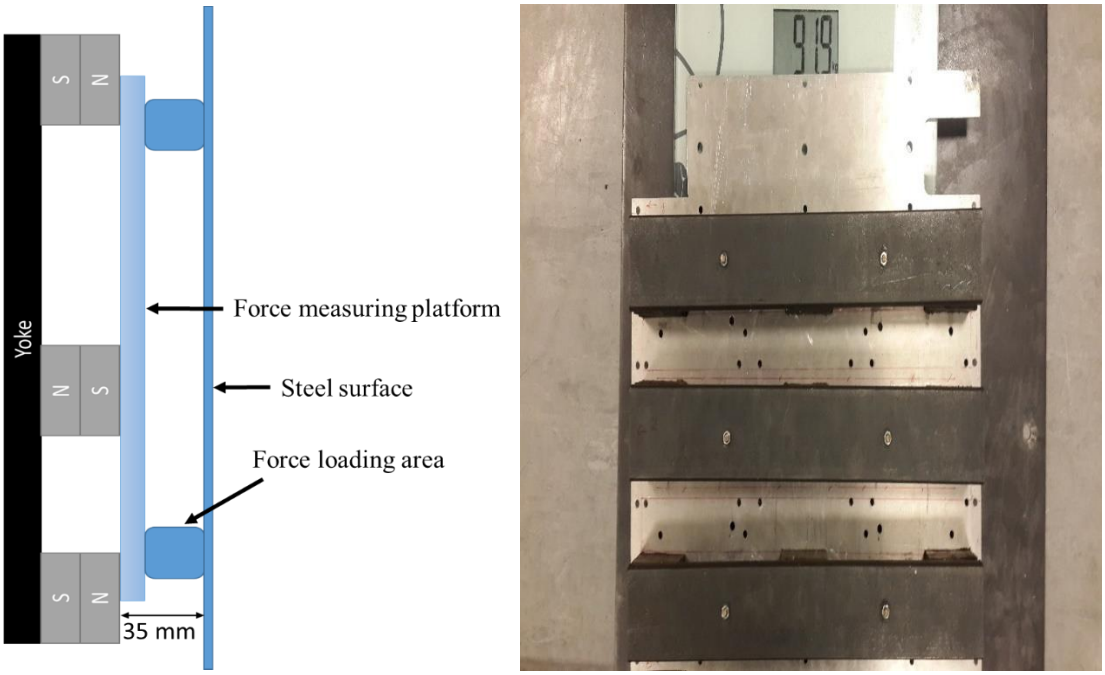

Figure 4-19. Force measurement setup of the multiple yoke based adhesion module.

Figure 4-20. Modified prototype robot completing: (a) surface transitioning procedure; (b) vertical and horizontal laser cutting task.

4.6 Chapter summary

A novel technique of magnetic flux concentration mechanism has been presented. In contrast to existing research findings, this research aims to manipulate physical and material constrains of permanent magnets to apply such adhesion system on a concrete surface where the attraction medium for permanent magnets is limited. The results show that the distance between the magnet and buried rebar has the maximum impact on the total adhesion force alongside the yoke thickness and the configuration of the magnet's polarity. The prototype system exhibits good payload capacity and can generate adhesion force of 121.26 N for the robot to climb a concrete wall reinforced with only one rebar located as far as 35 mm. Experiments on a test rig demonstrates the viability of 360^0 manoeuvrability of the robot on a reinforced rebar mesh surface. The minimum adhesion force is found to be 126 N on a 50×50 mm meshed surface when the robot is rotated around the vertical axis. This dense meshing is the only scenario where the robot is capable of completing a full 360^0 rotations. Considering the size and weight of the robot, a high payload capacity has been achieved by optimizing key design parameters of the adhesion mechanism. Overall, this mobile robot exhibits very good performance and force-to-weight ratio compared to other reported permanent magnet based robotic systems.

Chapter 5. GPR operating principles

This chapter describes the operating principles of a GPR system. It provides in-depth discussion of various components of a GPR system and antenna. The chapter is structured as follows:

5.1 Overview

Numerous types of sensor exist for detection of buried objects ranging from simple metal detector to much more complicated thermal neutron activation sensor. Deployment of those sensors depends on the application with their certain advantages and disadvantages. GPR is an EM radiation based sensor modality that has gained popularity in recent years because of its wide application area. GPR can sense metallic and non-metallic buried objects as well as obtain geometric information about the buried objects such as its depth and horizontal location. The application domain of GPR is versatile as it can be used in inspection of different media such as polar ice [89], water [90], dry sand etc. All of these capabilities make GPR a much more resourceful sensor compared to other subsurface sensors and has been considered as a matter of great interest for this research.

This chapter provides a background to the operational principles of GPR, including an explanation of the physics of EM wave propagation that governs the ability of GPR to penetrate through different media and provide data. The functionality of different GPR components have been elaborated in order to identify the scope of advancement in current GPR technology.

5.2 Robotic GPR inspection systems

The use of subsurface sensor as a sensing modality has received very little attention in robotics compared to other sensory systems such as thermal imaging, ultrasound or x-ray. As a result, there have been quite a lot of work in manual subsurface data gathering and interpretation compared to automated systems. Most of the work found in the literature about robotic subsurface imaging using GPR are mainly used for geological explorations and landmine detections. For example, the bridge deck assessment robot by [91] is a system capable of recognizing any harm to the bridge deck early without shutting down the traffic, highlighting zones which require fast repairs and henceforth constraining the effect on Washington's traffic. Figure 5-1 shows the system in operation using 2 GHz GPR with a total of 32 antennas.

Robotic field testing of underground pipe inspection using a combination of camera, LIDAR and GPR is reported in [92]. The system called ‘SewerVUE’, shown in Figure 5-2(a) can penetrate 60 cm – 2 m using antenna frequency ranging from 500 MHz – 2.6 GHz. It has two GPRs attached to its two arms which enable the robot to capture defect information along the 9 o’clock to 3 o’clock positions of a pipe section. Yeti robot [93]

shown in Figure 5-2(b) is a system to automatically classify GPR images of the crevasses on ice sheet. It implements hidden markov model based machine learning algorithm for real-time analysis and detection. Yeti uses 400 MHz antenna and tows the GPR along the polar ice surface and reports rough estimates of the crevasses location, depth, width, and snow bridge thickness.

While the robotic GPR inspection system has definitely gained some improvements in geological applications, GPR based inspection of vertical concrete structure is still facing challenges of hazardous environments such as nuclear industrial environments, working at high altitude, and limited manoeuvrability [94]. Therefore, the vertical concrete wall climbing robot proposed in this research can prove the concept of effective robotic GPR system for concrete structures.

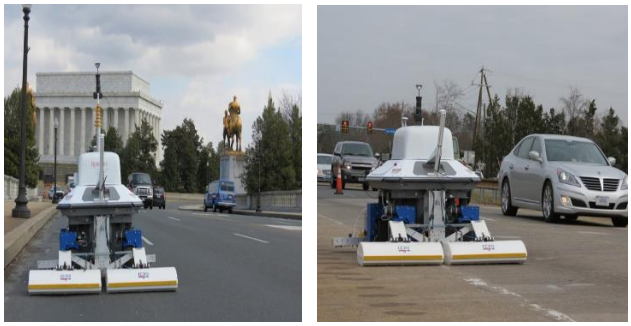

Figure 5-1. Operation of GPR bridge deck assessment robot [91].

Figure 5-2. Sewervue [92] and Yeti Robot [93] in operation.

5.3 Principles of GPR operation

GPR is an EM radar consists of a transmitter, Tx and a receiver, Rx antenna separated by a short distance apart. In such a system, EM pulses emitted by the Tx are propagated through a medium. Any discontinuity of electrical properties within the medium causes a part of the pulse energy to reflect back to the Rx antenna. This discontinuity is mainly caused by a buried object or the presence of a different medium ahead. The Rx antenna

converts the reflected pulses to electrical signal which are sampled by digitized receiver electronics. More often, separate antennas configured in a bi-static configuration are used for emitting and receiving EM pulses through the medium. Figure 5-3 illustrates such a system. On the contrary, a single antenna in mono-static configuration can be responsible for both sending and receiving EM pulses. A monostatic system requires extra timing circuit and multiplexer to synchronize the sending and receiving procedure. However, this setup gives rise to problem of extra reflection from the immediate surface layer. The propagation time of this extra reflection is fast and shorter than the transmitting pulse itself. It is a challenge to distinguish this extra reflection which requires very sophisticated electronic system. Even though, such fast synchronization switches can be found, their performance is not satisfactory enough for use in a GPR system. To negotiate this problem, bi-static configuration with certain gap between the antennas have been considered in this research where one antenna functions as a transmitter and another antenna as a receiver. Regardless of a bi-static or mono-static configuration, mounting the antennas above ground makes operation of the GPR system more portable.

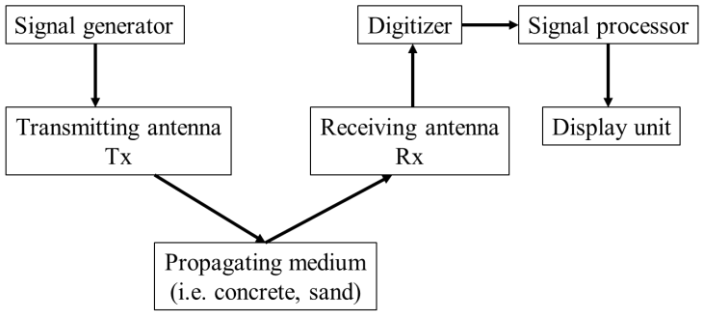

Figure 5-3. Block digram of a bi-static GPR configuration.

The most common method of GRP surveying is single-fold common-offset reflection profiling that involves transporting the antennas along survey line to map reflections against its position. This surveying method generates data as illustrated conceptually in Figure 5-4.

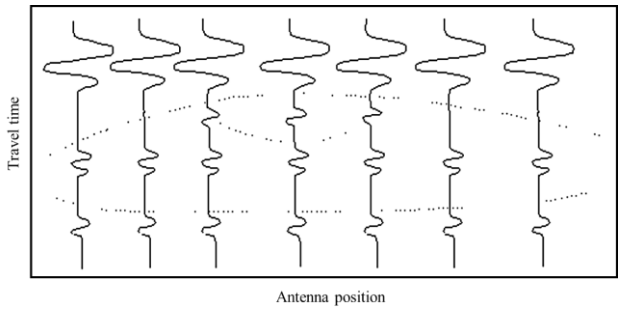

Figure 5-4. Format of reflection at different GPR antenna positions [95].

The radar system repetitively emits EM pulses into the medium and two-way travel time of the transmitting and reflecting pulse is measured. This measured travel time is very critical in detecting and measuring the depth of reflecting discontinuities in subsurface materials and other earth materials to within a few centimetres of accuracy. Moreover, the performance of the GPR system depends upon the physical parameters of the medium, dimension of the target buried object and the frequency of operation. For most subsurface investigation, the antenna unit is pulled along the inspection line and the two-way travel time versus the distance plot is generated in the control display. The scan rate at which the data is collected along the length of survey must be controlled for in-depth scanning. The limit of the scan rate relies upon the GPR system specification and antenna configuration. For example, if the GRP allows a maximum scan rate of 80 scans per second for every 5 cm gap along the survey line then the maximum surveying speed possible is 5 cm × 80 s^{-1} = 400 cms^{-1} or 4 ms^{-1}.

The nature of the propagating medium is vital in deriving the object depth as the medium's dielectric permeability influences the EM wave propagation speed through that medium. If a pulse is transmitted through a homogeneous material, where c is the EM wave propagation velocity in free space and εr_1 is the relative permittivity of the first medium, then the vertical depth of a test point, P_1 located at the boundary of two media with different dielectric constants shown in Figure 5-5 can be calculated using the velocity equation in Equation (5.1).

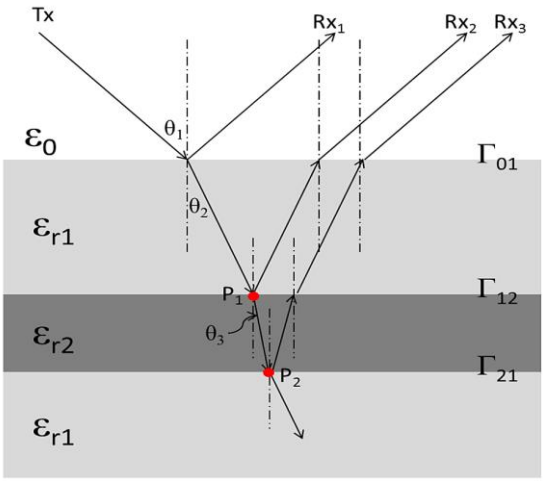

Figure 5-5. Incident, refracted and reflected GPR EM pulses.

$$v = \frac{c}{\sqrt{\varepsilon_{r1}}} \tag{5.1}$$

The depth, d_1 of the point, P_1 is derived from Equation (5.2), where θ_2 is the refraction angle that can be easily calculated using Snell's law [96] given the incident wave angle

θ_1, and ∇t is the time difference between receiving the first reflected pulse Rx_1 and the second reflected pulse Rx_2 received by the Rx antenna. θ_2 can be calculated by using the Snell's law given the incident angle, θ_1 [96].

$$d_1 = v\frac{\nabla t}{2}\cos\theta_2 \tag{5.2}$$

The thickness of the medium with εr_2 dielectric constant can be calculated once the depth, d_2 of the second test point, P_2 is measured using the same procedure as above. If the approximate dielectric constants of multiple layers are known, then a cross-sectional image of the material can be constructed.

GPR can provide information about the nature of the buried object from its reflected signal energy as well. The reflection coefficient, τ_{12} is the measure of the energy reflected from the second medium back to the first during the normal incident. Equation (5.3) defines the calculation of τ_{12} using the characteristic impedances Zo_1 and Zo_2.

$$\tau_{12} = \frac{Z_{o1} - Z_{o2}}{Z_{o1} + Z_{o2}} \tag{5.3}$$

The characteristic impedance, Zo is defined by the ratio of the electric, E and magnetic, H field inside a specific medium. So,

$$Z_o = \frac{E}{H} = \sqrt{\frac{-j\omega\mu}{\sigma - j\omega\varepsilon}} \tag{5.4}$$

Here, ω is the frequency, μ is the magnetic permeability, ε is the electric permeability, σ is the electric conductivity of the medium. These characteristic equations confirm the versatility of the GPR that can not only detect the depth and thickness of buried layers, but also can partially reveal their material characteristics.

5.3.1 Types of GPR

Based on the operation principle, a GPR can be categorized as a time-domain or a frequency-domain system. In a time-domain system, GPR sends a pulse at a given pulse repetition frequency (PRF) into the medium and receives the backscattered echoes. The family of time-domain GPR is divided into two categories: (a) amplitude modulated GPR and (b) carrier free GPR. Pulses are sent with a carrier frequency in amplitude modulated system. The duration of those pulses are kept short (in the nanosecond region) for good depth resolution. Monocycle pulses are mostly used for this application where the centre frequency, f_c can vary from few MHz to GHz.

The bandwidth of monocycle pulses used in carrier based system is small. This issue led to the development of a second category of time domain GPR i.e. carrier free or impulse GPR. In an impulse GPR system, a Gaussian pulse of sub-nanosecond pulse width is sent without any carrier. Impulse GPR can offer higher bandwidth compared to amplitude modulated system and is easier to construct.

In frequency-domain operation, GPR is divided into linear sweep GPR and stepped frequency GPR. A liner sweep GPR continuously transmits a changing carrier frequency by means of a voltage controlled oscillator (VCO) over a chosen frequency range. The frequency difference between the transmitted and the received signal is a function of the buried target depth. As this category of GPR transmits and receives signals continuously, it suffers from the signal leakage between the antennas. This leakage can mask the smaller backscattering wave and as a result, dynamic range of this type of GPR is very poor.

To overcome issues faced by the continuous wave GPR, a stepped GPR uses a frequency synthesizer to step through a range of frequencies equally spaced by a time interval. Here transmitting signals are mixed with the received signals at each frequency region using a quadrature mixer. Implementation of highly accurate and low-speed analogue-to-digital converters (ADC) can offer precision sampling of data.

The impulse radar has a major advantage compared to frequency domain radars as a time domain pulse can contain a spectrum with a given frequency content. The spectrum is directly linked to the shape and strength of the time domain pulse meaning that a broad range of frequencies can be sent into the medium simultaneously. This characteristic is not possible in the frequency domain radars where each frequency must be transmitted individually one after the other. For this reason, the impulse GPR will be the subject of investigation in this thesis.

5.4 Components of a time-domain impulse GPR

Apart from the data processing circuit and the display unit, the main components of an impulse GPR system shown in Figure 5-6 are antenna unit with transmitter and receiver circuits. This section discusses the fundamentals of each component.

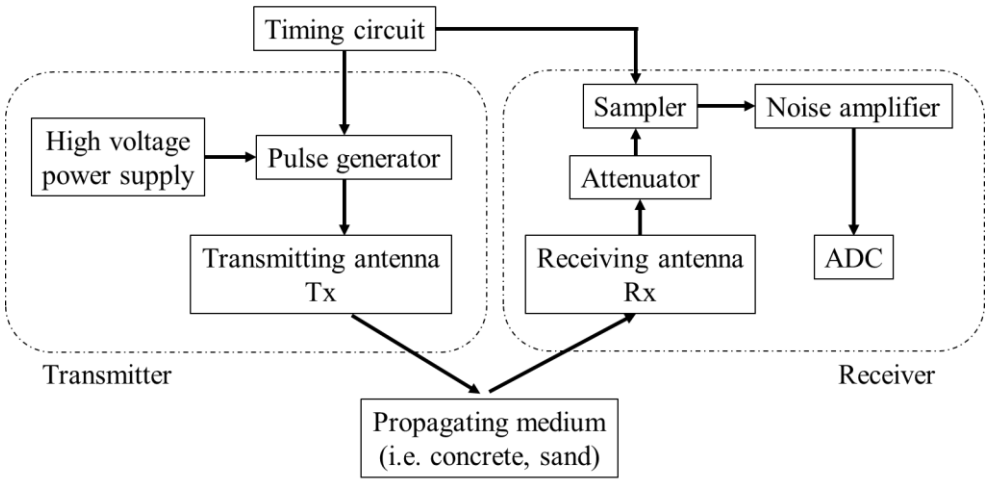

Figure 5-6. Block diagram of an impulse GPR system.

5.4.1 Transmitter

The function of a transmitter is to generate very short transient pulses of energy characterised by their peak power and their average power. Typical short pulse durations can range from 800 ps to 2 ns and the peak voltage can reach from 1 V to 200 V. The building blocks of an impulse generator are given in Figure 5-7 which contain a charging and a load impedance, energy storing capacitor as well as a fast switch. The technique of the impulse generation is based on the rapid discharging of capacitive energy through the fast switch that generates a short duration pulse. The duration of the pulse is in inversely proportional relation to the load impedance and the capacitance. The shape of the pulse is typically a monocycle or a Gaussian pulse. However, more complicated pulse shapes such as 2nd derivative of Gaussian or doublet Gaussian pulses as shown in Figure 5-8 can be generated using the same principle.

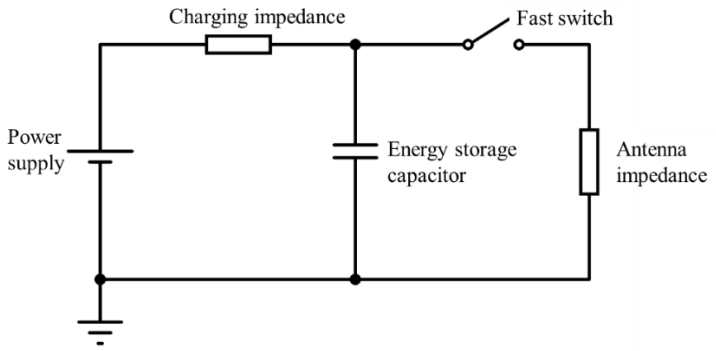

Figure 5-7. Block diagram of an impulse generator.

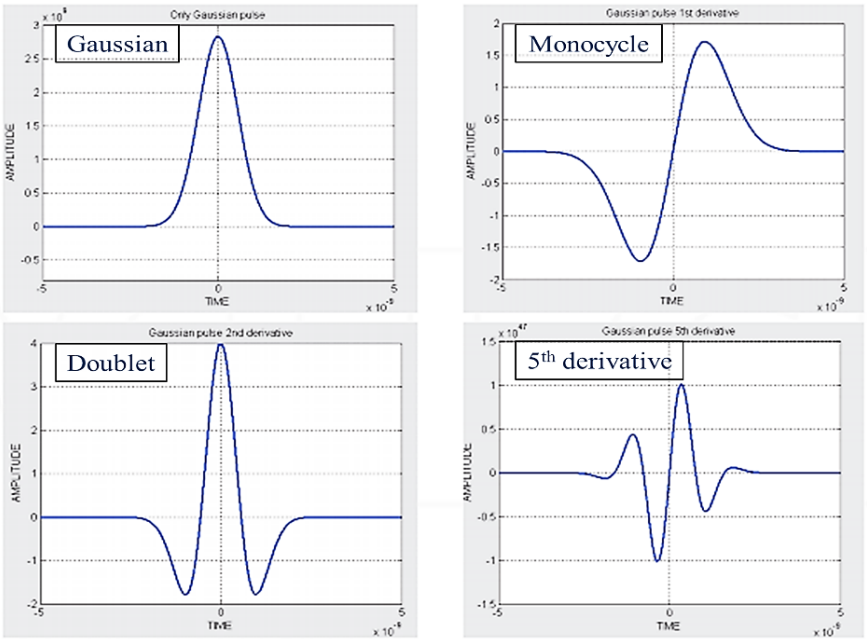

Figure 5-8. Gaussian, Gaussian monocycle, Gaussian doublet and 5th order Gaussian derivative pulse shape.

In order to ensure EM waves with sufficient peak power, a high voltage pulse is required. To achieve that, energy storage capacitors are charged in parallel from a low voltage source such as 12 V. Series discharging of multiple storage capacitors account as a voltage multiplier and produce a high voltage pulse. Alternatively, a DC-to-DC boost converter can be implemented to produce sufficient energy from 12 V to 400 V. More often, a combination of the two methods are used [97]. According to recent reported works, several techniques have been implemented to generate wideband pulses in the order of nanoseconds. The most traditional approach involves electric Marx generators [98], transmission line pulse forming networks and short-circuited stubs [99], micro strip transmission line or other newer fast semiconductor technology. However, these methods usually use Step Recovery Diode (SRD) for pulse sharpening purpose and SRD introduces pulse distortion and extra ringing into the output pulse [100]. The most reported method of narrow pulse generator is that of using avalanche transistors. Transistors operating in avalanche mode can generate pulses with amplitude of tens of volts however, can hardly reach picosecond range. Moreover, such circuits require high reverse biased voltage [101]. Detail discussing of development process a GPR pulse generator is provides in later chapter.

5.4.2 Receiver

The receiver has a direct impact on the over-all system performance. It is a more complex device then the transmitter which has to be very sensitive with a large

fractional bandwidth, a large dynamic range and a good noise performance. The main blocks of the receiver circuit are a time-varying gain (TVG) amplifier, a low noise amplifier (LNA), a sample and hold circuit (S/H), and an ADC. The block diagram of receiver is shown in Figure 5-9.

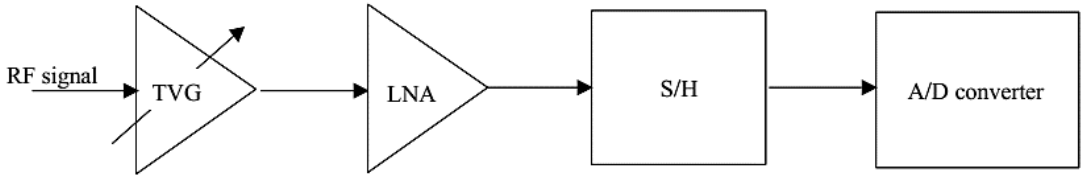

Figure 5-9. Block diagram of a GPR receiver circuit.

ADC at the receiver end is used to sample and digitize the reflected wave captured by the receiving antenna. Most of the received signals are in the GHz frequency range and most converters cannot deal with such high sampling rate. This problem is addressed by sequential sample and hold method that repeats the signal generation for a specific repetition frequency and sample only one digitized point in each reflected signal. Shifting the sampling time for the acquisition of each point provides the complete reconstruction of the received waveform. This method allows a conversion of the signal from the nanosecond to the micro or millisecond region and has been used in most sampling heads of ultra-fast oscilloscopes these days.

For accurate analogue to digital conversion procedure, the input signal must be stable for a certain time period. Therefore, the rate of input signal variation must be lower than the quantization step of the ADC used. The sample and hold circuit that is consisted of four bridge diodes keeps the signal variation to a minimum. During the hold mode, the reverse biased diodes prevent the input signal from conducting. The sampling mode is triggered by two narrow pulses of opposite polarity that cause the reverse biased diodes to conduct. The charging voltage of a capacitor, C_s is proportional to the input signal such that the sample corresponds to a specific portion of the input signal. A circuit diagram of the sample and hold circuit can be seen in Figure 5-10.

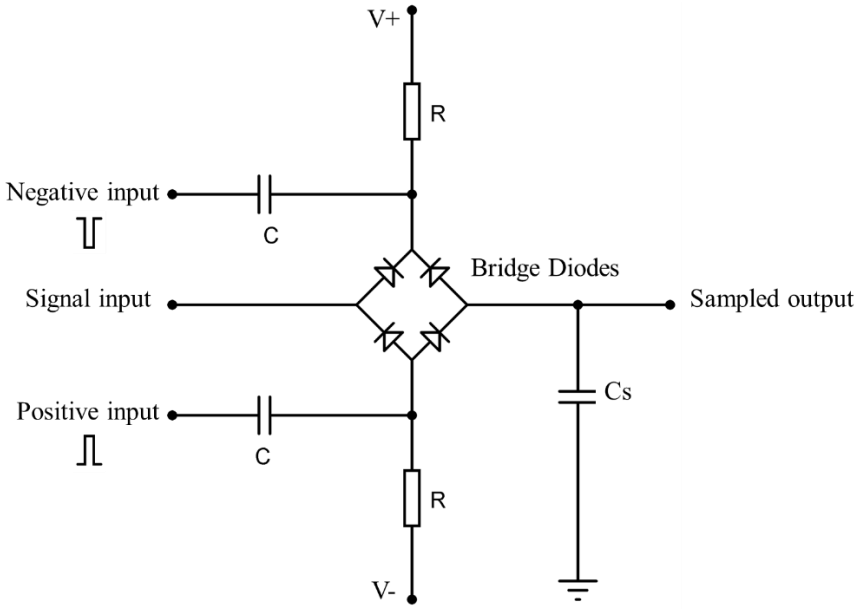

Figure 5-10. Schematic of a sample and hold circuit.

The number of data points recorded along the time axis is 256 or 512 depending the bit resolution of the ADC. The time resolution range can be from 250 ps to 1 ns which decides the maximum time window possible. For instance, 512 data points at 1 ns time resolution can produce time window of 1 ns × 512 or 512 ns. The amplitude resolution is a function of the ADC, 12-bit converter can record 2^{12} amplitude points and 16-bit converter can do 2^{16} points.

As the transmitting pulses from the Tx antenna propagate in lossy medium, reflected signals from the buried objects experience attenuation due to ground loss. A deeper object means greater losses therefore, a TVG is vital to compensate for the signal attenuation. In practice, TVG is not an amplifier that changes its gain as a function of time. Instead, it focuses more importance on the signals that have travelled deeper into the medium and experienced higher degree of attenuation. In fact, TVG an attenuator whose attenuation is changed as a function of time in order to bring the deeper reflections to a level similar to the shallower reflections. TVG circuit is based on PIN diodes that have the capacity of varying resistance as a function of voltage [102]. The TVG must be chosen carefully as a low gain can cause the radar to loose sensitivity. Alternatively, a high gain can saturate the sampling unit and ultimately limit the detection capability. Therefore, a design trade-off based on the application and the application medium is pivotal for successful implementation.

5.4.3 Antennas

Antennas are the most critical elements in a GPR system as it is believed that the main breakthrough in GPR hardware can be achieved in the antenna design [103]. It dictates the GPR performance in its capability of detecting buried objects therefore, their design must satisfy a number of requirements. One of the main characteristics of a GPR antenna is its ability to radiate short transient pulses which is directly linked with the antenna broadband capability. The fractal bandwidth of a GPR antenna can be as high as 160 % which is termed as ultra-wide band (UWB) antenna. High bandwidth capacity also ensures sufficient scan resolution of the system. In general, achieving an acceptable level of scan resolution requires a high gain antenna. To meet this requirement, the antenna dimension must be greater than the wavelength of the lowest frequency of the transmitted signals. Therefore, low frequency GPR system results in impractical dimensions of antenna. To achieve small antenna dimensions and high gain therefore require the use of high frequency signals. The implication with high frequency signals is that they do not penetrate the ground material to a sufficient depth. As a result, desired resolution, antenna dimensions and the penetration depth requirement are the design trade-offs that must be considered when choosing equipment for any particular application.

Besides, as GPR is effectively a near-range radar, the coupling between the Tx and Rx antennas must be minimum. If antennas are not well isolated from the effect of the material, then unwanted clutter will be presented in the reflected signals that may mask the target return. Moreover, both the antennas must have low ringing effect. High ringing effect can distort the transmitted signal which in turn limits the bandwidth characteristics of the signal and overshadows the target reflections. As GPR antennas are positioned very close to the ground while pulled along the survey line, the changes in the ground medium and electrical properties must not affect the antenna performance. Hence, the GPR antenna performance must be accessed both in free space and in realistic ground penetrating environment [104].

In general, several types of antennas are commonly used for impulse GPR system, such as; dipole, bow-tie antenna, spiral antenna, Vivaldi antenna and the most widely used TEM horn antenna. The dipole is simple, easy to design and linearly polarized antenna structure. However, the bandwidth achievable from a dipole is only 30% of its fractal frequency. Wu-King [105] proposed a loading profile for dipole antenna that exponentially increases the resistance towards the antenna end as illustrated in Figure

5-11. Resistive loading of dipole this way increases the bandwidth of the antenna. However, the increasing resistance causes extra losses in the antenna and thus reducing its efficiency and gain. This makes other planar antennas, like Bow-tie and spiral structures, a more attractive choice.

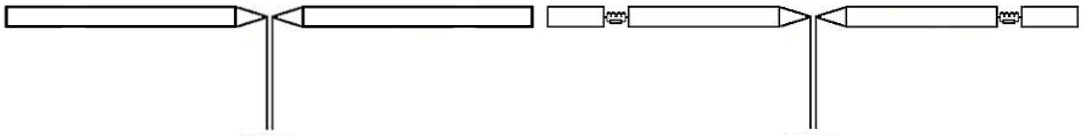

Figure 5-11. A conventional dipole and a loaded dipole antenna.

Bow-tie antennas are mainly used in impulse GPR applications because of their non-dispersive characteristics and their relatively high gain. Its wideband characteristic is a function of the arm width and the arm length determines the centre frequency. Therefore, the antenna behaviour depends on the antenna dimension with regard to the frequency. If the arm width is less than 0.6 times the wavelength, then the antenna can be regarded as a dipole with cylindrical arms [106]. The bow-tie radiation pattern is the same as the dipole but the antenna directivity is more focused to the top and bottom of the antenna. This offers less interference and is an advantage for GPR. Resistive loading can also be adapted for bow-tie antennas to increase its overall bandwidth. However, mismatch in the loading profile could add the ringing effect and distort the time domain waveform. Resistive loading technique always leads to deteriorating gain performance over the frequency wide band as shown in [107]. Figure 5-12 shows the typical structures of a bow-tie.

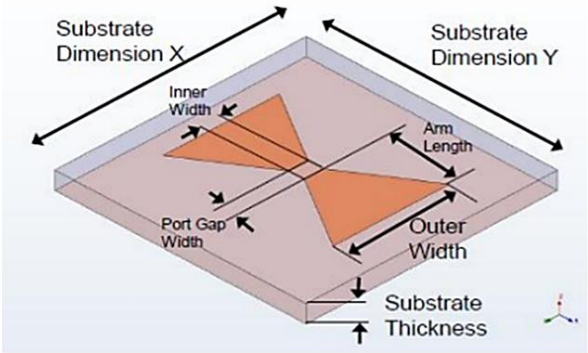

Figure 5-12. Design parameters of a bow-tie antenna.

A vivaldi antenna is a special tapered slot planner antenna. It consists of a micro strip feed line and two ground planes separated by a dielectric substrate as demonstrated in Figure 5-13. It is a frequency independent antenna with significant gain and linear polarization. Gain of 10 dBi with -20 dB side lobe has been reported for 2 – 40 GHz

span [108]. The antenna performance is depended on the nature of the dielectric substrate used. Having an exponential tapered profile, the antenna creates a virtual long electrical length compared to its actual physical length. Hence, compact vivaldi antenna size is achievable for a wide frequency range without compromising the gain.

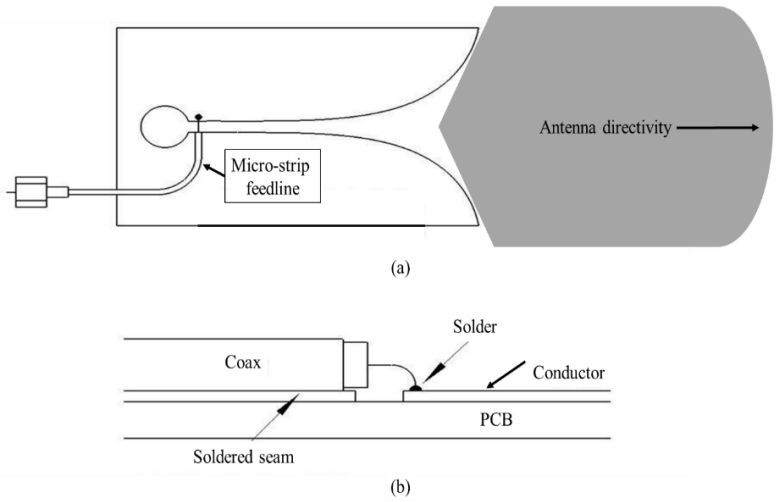

Figure 5-13. Layout of a vivaldi antenna: (a) top view; (b) side view.

TEM Horn antenna has a clear advantage over planar antennas described. A typical TEM Horn antenna structure is shown in Figure 5-14. Its narrow beam width typically ensures a higher directivity gain over a wider frequency range. The main design challenge is to achieve a good impendence matching in order to minimize feed point and aperture reflections. A design modification of the TEM horn antenna to achieve a better impedance matching can be found in [109]. The TEM horn-fed ridged horn antenna proposed, demonstrates a high gain up to 10 dB over a wide frequency range of 400 MHz to 16 GHz, with input reflections down to -10 dB. However, simulation results show that this design suffers from relatively high reflections over frequencies less than 3 GHz and greater than 7 GHz.

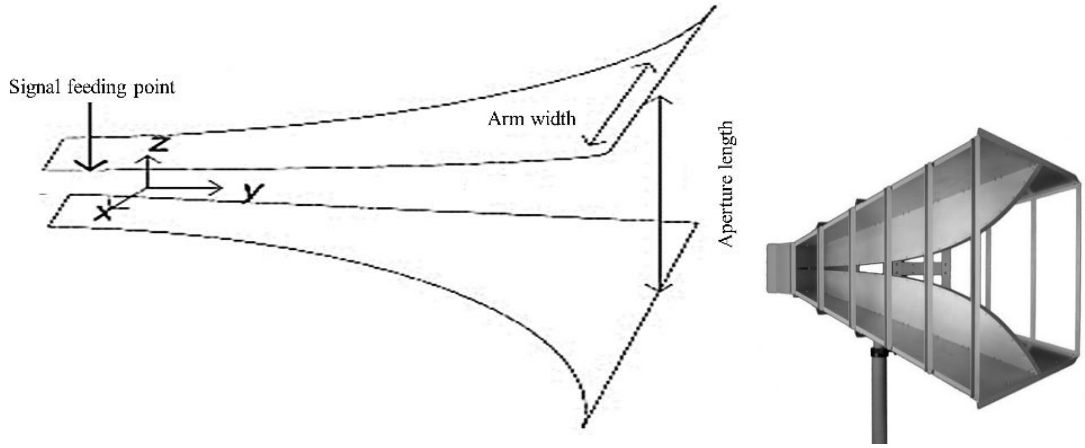

Figure 5-14. Design parameters and a manufactured TEM horn antenna.

5.4.4 Miniaturization of GPR antenna

Several compact design antennas have been proposed in the literature for GPR, telemetry, biomedical applications. Reference [110] proposes a miniaturized bow tie antenna for wideband applications. The length of bow-tie antenna is generally λ/2 of lowest operating frequency. The length of the bow-tie could be shortened by connecting the right and left arm of the bow-tie with thin conductor called folded elements as Figure 5-15. Folded elements bring the lowest frequency for VSWR ≤ 2 from 540 MHz to 300 MHz and a reduction of 31% in size. However, the folded bow-tie antenna (FBTA) suffers from degradation of VSWR characteristics at 920 MHz and 1860MHz. The authors suggest adding additional elements (AE) between the folded element and the bow-tie element to improve the VSWR characteristics. However, final results show improvements in VSWR values at 920 MHz and 1860 MHz, but the lowest operating frequency still stays at 300 MHz and no further reduction in size compared to original folded bow-tie antenna without additional elements.

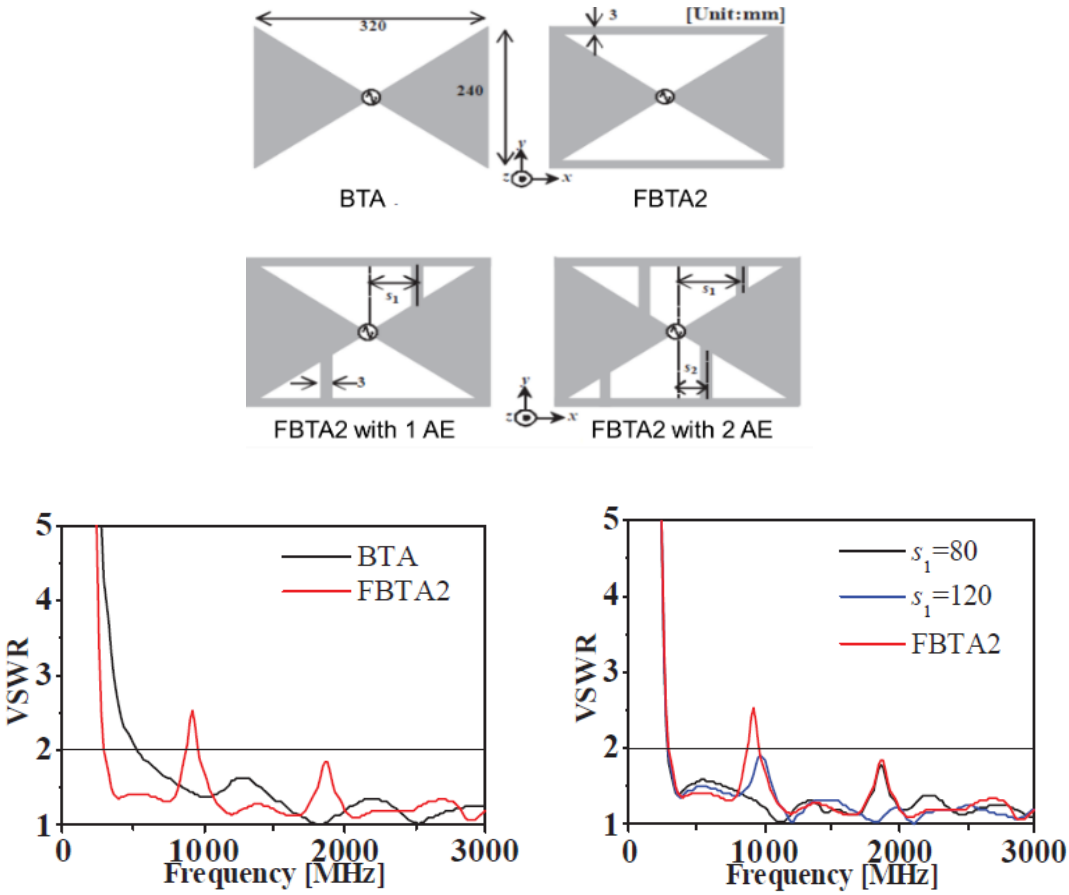

Figure 5-15. Bow-tie antenna with additional elements and their corresponding VSWR as proposed in [110].

In [111], a high frequency bandwidth antenna for the low frequency operation is proposed (Figure 5-16). The antenna dimension is 10×10×15 cm and the resonant frequency is 40 MHz. Even though the resonant frequency of the antenna is considerably low, the shape of the antenna makes it impractical to implement in GPR applications.

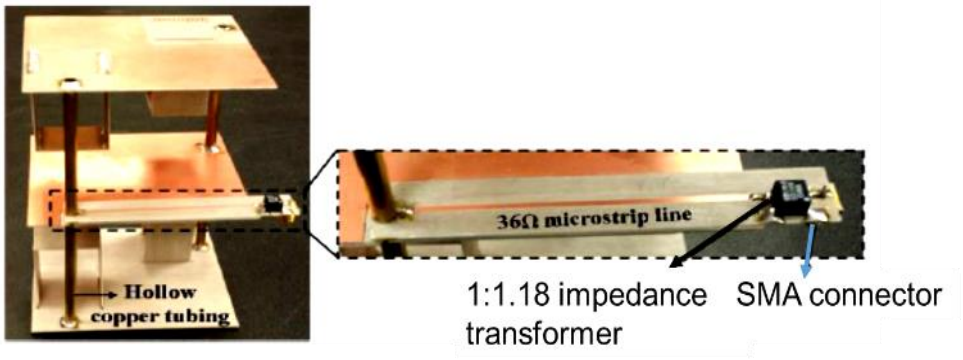

Figure 5-16. The fabricated antenna in [111].

In [112], the authors described a miniaturized dipole antenna for wearable devices. They used Koch fractal technique to reduce the antenna size and recorded a reduction of 108 mm in length for a 450 MHz fractal dipole compared to a conventional dipole. Jeans fabric was used as the material with permittivity of 1.6 to make it applicable to wearable applications. Moreover, the Koch antenna provided better reflection coefficient value of – 26 dB compared to -16 dB for a dipole of the same frequency range as given in Figure 5-17.

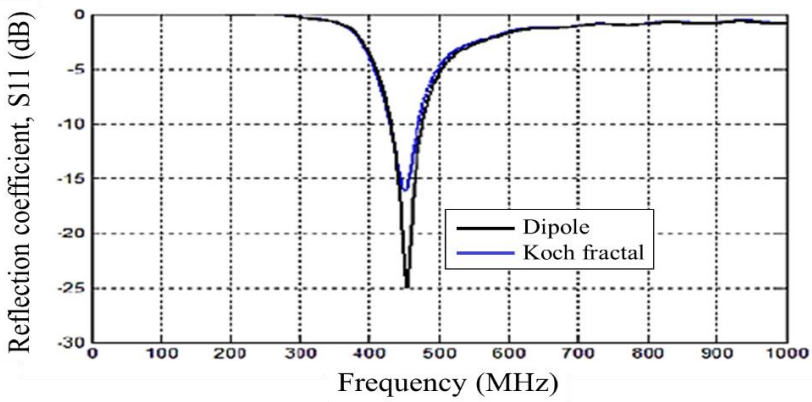

Figure 5-17. Layout of a fractal dipole antenna with its reflection coefficient values compared to a conventional dipole antenna [112].

Miniaturization technique for a strip folded dipole antenna (SFDA) by using two vertical linear conductors as shown in Figure 5-18 is described in [113]. A reduction of 26% is claimed for the SFDA antenna compared to a conventional folded dipole of 700 MHz resonant frequency. The antenna was built on material with permittivity of 1. However, VSWR characteristics graph shows that, antenna built on materials with higher permittivity such as 17.1, the resonant frequency could be lowered but VSWR values worsen as a result.

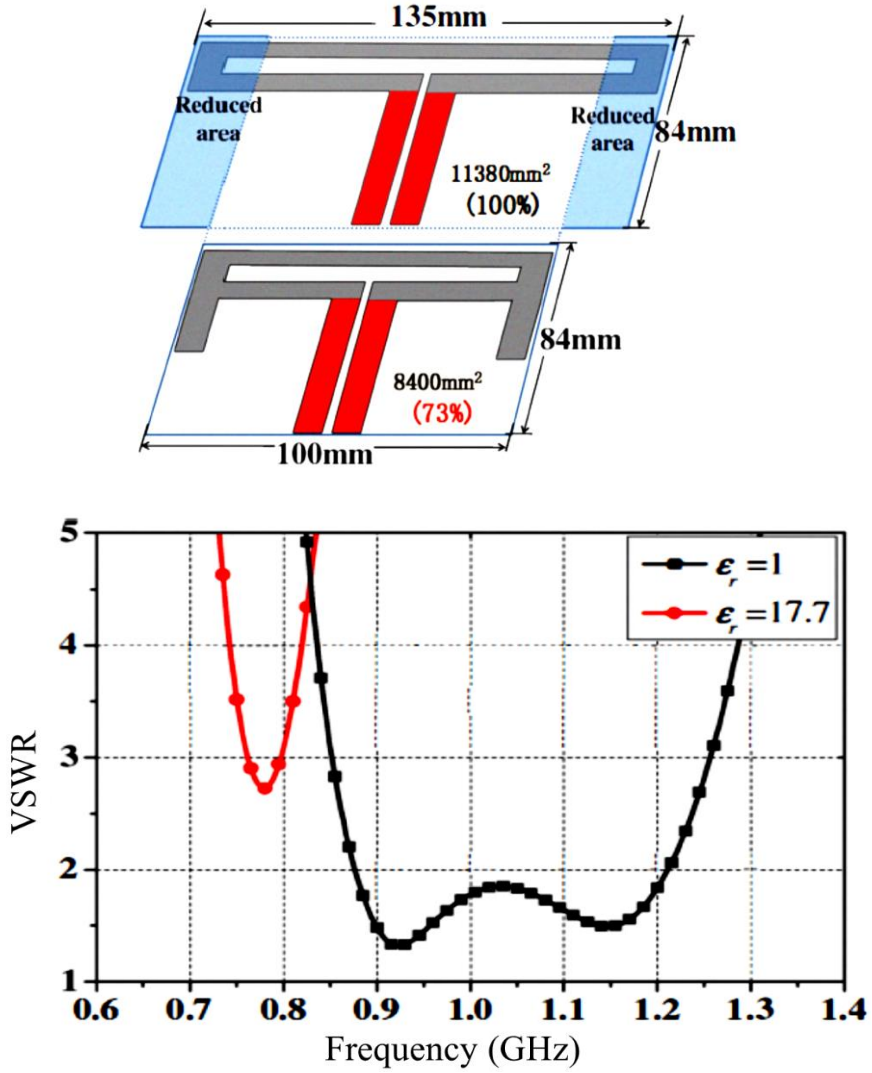

Figure 5-18. Proposed SFDA antenna and its VSWR behaviour [113].

Likewise, in [114] bow-tie antenna with folded elements of various inclinations have been studied. However, they offer no considerable improvements compared to conventional folder bow-tie antenna of the same resonant frequency. A planer folded dipole antenna with wide ground plane has been proposed in [115]. The current distribution of the folded elements in as Figure 5-19 shows that by loading the folded element of the antenna, the current at the upper edges increases strongly. It means,

impedance characteristics of the antenna could be controlled by the current pathway at the edges of folded structure. However, VSWR results show that widen ground plane and folded arms do increase the overall bandwidth of the antenna, but the resonant frequency stays at 1.35 GHz which is equal to a conventional dipole.

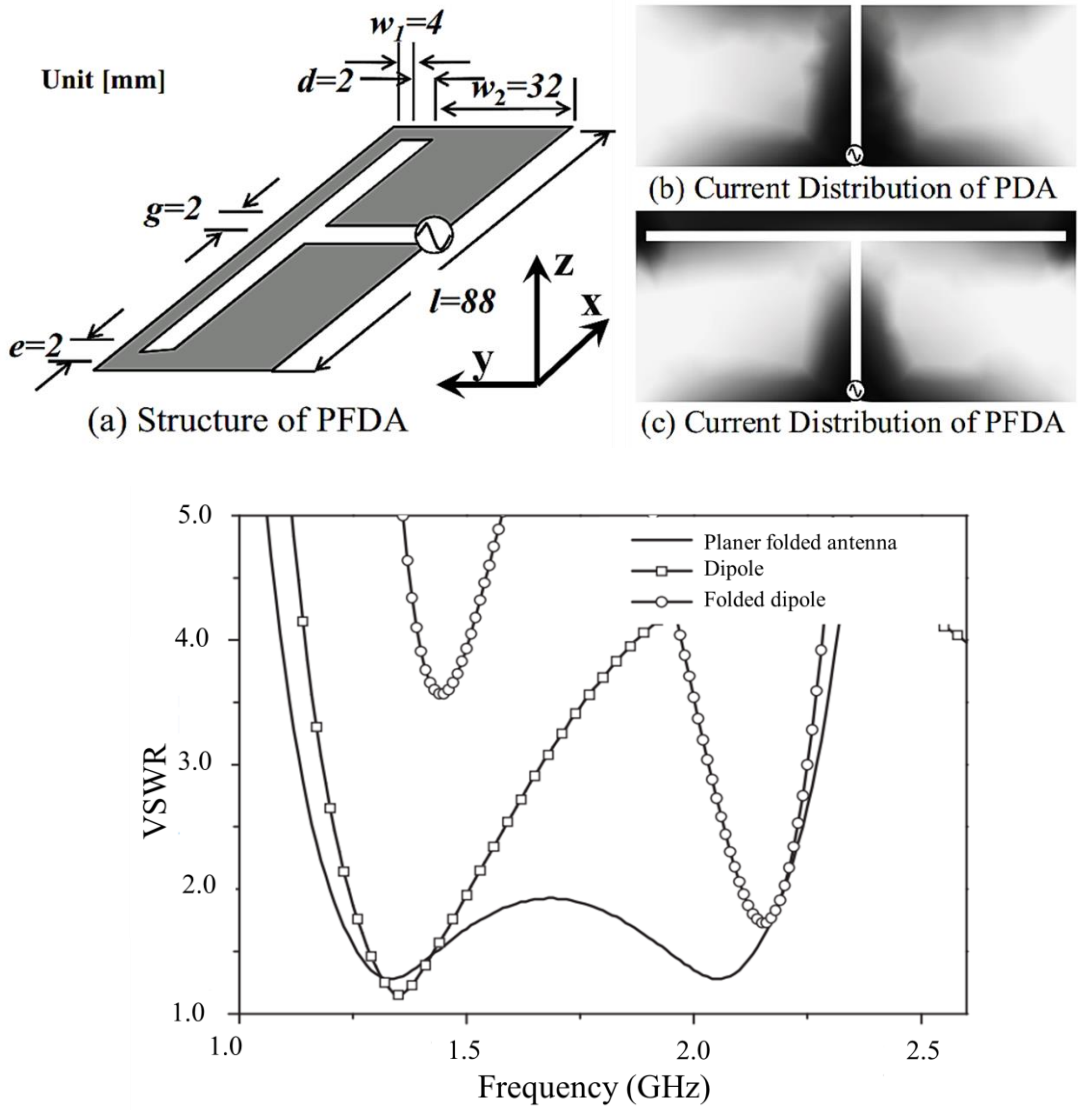

Figure 5-19. PFDA antenna and VSWR characteristics [115].

More examples of miniaturizing dipole and bow-tie antennas could be found in [116], [117], [118], [119] etc. But most of the designs discuss antenna miniaturization techniques for high frequency UWB and RFID applications hence, it is ideal to focus on miniaturization techniques of low frequency antennas and detail discussion of miniaturization technique is provided in later chapter.

Other factors that can influence the GPR operation include type of the medium, moisture content etc. Depth penetration of the GPR pulses depends on the electrical characteristics of the medium such as permeability, conductivity and dielectric

constant. The homogeneity of the medium confirms better resolution and low attenuation. For example, sand has a very low permeability, resulting in a low attenuation rate for the signals in GPR frequency. Clay on the other hand causes a very high attenuation rate. As a result, GPR signal cannot penetrate too deep in the soil with high clay concentration. Moisture content influences the electrical characteristics of the soil. Usually moisture content increases the attenuation rate [120] as given in Figure 5-20 and in some cases a layer of medium with a very high moisture content can cause a strong reflection of the GPR signal.

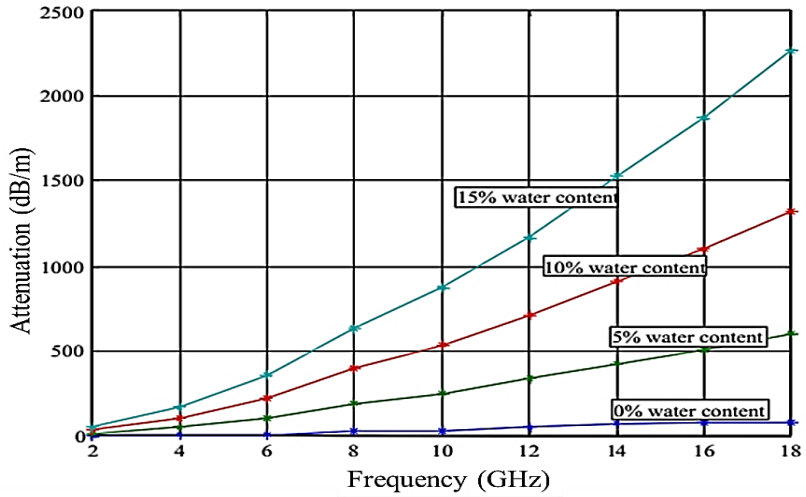

Figure 5-20. Rate of signal attenuation in sand as a function of frequency and water content [120].

5.5 Chapter summary

In this chapter, the modes of GPR operation have been presented. GPR and other types of radar are categorized based on the desired application. GPR based on frequency-domain mode offers low resolution compared to a time-domain impulse GPR. An impulse GPR can transmit Gaussian pulses with high power density that offers high resolution and detection capability. The building blocks of an impulse GPR reveals a nanosecond width pulse generator is at the heart of the transmitter circuit. Pulse width of the transmitting pulse determines the wide bandwidth feature of the GPR.

Additionally, detail discussion of the GPR antennas establishes that the dimension of the antenna configures the operating frequency and bandwidth of the signal. Therefore, a frequency matching between the transmitter and the antenna is vital. Any mismatch will severely limit the antenna radiation capability. Different antenna designs show the possibility of design modification for better matching and system portability.

Chapter 6. Numerical modelling of the GPR

This chapter presents a one-dimensional numerical framework based on FDTD method to model response behaviour of GPR. The objective is to assess the modelling criteria and success rate of detecting buried object using the framework. This chapter is structured as follows:

6.1 Overview

The previous chapter has presented various components and the fundamental principles of GPR operation. The key performance factor of any GPR application is the penetration depth achieved or the lack of penetration which depends on the electrical characteristics of the object and of the material in which the object is buried. The penetration depth is rapidly attenuated in conductive lossy materials. In [121], experiments showed that a high absorption of EM waves can be caused by the presence of high moisture content in the propagating medium while the presence of salt water can cause total attenuation of the signals. Another crucial factor is the lack of clear reflectors due to the presence of an inhomogeneous medium which limits successful application of GPR to obtain valid information on the geometry of the structures and on the kind and size of existing faults in it [122]. The responses received by the GPR in different application fields are complex. Therefore, one can use empirical methods and process to a series of testing during the GPR hardware development process to achieve the desired design specifications. The other option is to use simulation tools to predict the GPR performance and EM wave propagation behavior in different scenarios. The implementation of simulation tools can assist the designer to fine tune the design parameters to make the system robust. This also allows the investigation of many other configurations such as transmitter design, antenna design etc. without building any hardware.

The objective of this chapter is to review the main numerical methods for GPR signal analysis, such as the ray-based method [123], the frequency-domain method [124], the methods of moment (MoM) method [125], the finite element method (FEM) [126], and finally the FDTD method [127]. The FDTD method is the most popular EM technique in terms of its suitability and user-friendliness to solve GPR problems. In this chapter, a numerical framework for GPR modelling based on FDTD has been discussed. FDTD method has been used to model GPR scenarios which involve wave propagation in complex media such as nonhomogeneous, lossy, dispersive and non-linear media and objects of arbitrary shape. Effect of parameters such as the electric permittivity, magnetic permeability and conductivity of the medium on EM wave propagation has been investigated and a real life GPR application of detecting and measuring the depth of a steel rebar buried under a concrete cover has been presented. This chapter presents a version of the FDTD code based on the proposed numerical framework and has been implemented in Matlab to model and simulate a GPR's performance. A computationally intensive full 3D model will provide a complete view of wave

scattering and other interactions. However, due to the large amount of book-keeping required in any full 3D-FDTD code, the dimensionality has been reduced to 1D for better understanding of the framework while a 3D version can be derived using the same framework.

6.2 Justification for using FDTD method

There are several modelling techniques available for GPR modelling. The application of a certain method depends on the need and the environment to be analyzed, bandwidth requirement and the computational power available. The most important aspect of creating a model is the accuracy, time requirement and troubleshooting capability. This section presents an overview of the most popular techniques, their advantages and disadvantages.

6.2.1 The MoM mehtod

The MoM is a frequency-domain technique based on integral equations. The technique is implemented by breaking down the entire problem structure into wire segments or surface patches and deriving the current on each segment [128]. The dimension of the segments and patches must be smaller than one tenth of the operating wavelength in order to ensure accurate computation of the flowing current. The structure is initiated by a travelling plane wave or a voltage source on one of the wire segments whilst the MoM method calculates the unknown currents flowing on the structure. At the heart of the MoM is a coupling Green's function that integrates electrostatic coupling between the segments [129]. For example, if the spatial charge of the currents is known accurately for one segment, then the accumulation of charges at points on the structure can be computed. Subsequently, the electromagnetic field can be computed at any point of space by summing up all the contributions from all wires and all surface patches defining the structure.

6.2.2 The FEM method

The FEM is a powerful and versatile technique for modelling complex geometry problems and inhomogeneous media. The FEM handles complex region by discretizing the solution region into a finite number of elements [130]. The idea is that the structure is divided into a finite number of non-overlapping elements with specific electric and magnetic field response for each element. The entire problem area is assembled using meshing technique and solved with a polynomial function. In 3D space, the meshing

could of tetrahedral or hexahedral nature. For the complete convergence of complex geometry, meshing of very fine setting is required. Fine mesh setting increases the total number of elements and thus the total computation time. Therefore, a trade-off is required to keep the divergence to a minimum [131].

6.2.3 The FDTD method

The FDTD method provides a robust and dynamic electromagnetic modelling technique that simulates the behaviour of electromagnetic field interactions in both space and time. The FDTD is mainly a differential time domain numerical modelling solution where Maxwell's electromagnetic equations are solved in their differential forms in a time-stepping procedure [132]. The equations are solved by solving the electric field at a given time-step followed by the solution of the magnetic field at the next time-step and the process repeat itself until the entire structure is resolved. Permittivity and permeability values are assigned to each electric and magnetic component respectively to define the dielectric properties of a specific medium [133]. The computational power required and elapsed time depend on the number of cells that the entire structure is divided into and to the number of time-steps. Moreover, an infinite structure region can be modelled using the FDTD by implementing an absorbing boundary condition (ABC) [134]. A detail structure of the FDTD algorithm is provided later in this chapter.

6.2.4 Comparison of the methods

Each of the methods discussed above have their pros and cons that can outline their suitability for a specific application. Starting with the MoM, the number of wire segments determines the accuracy of the model. A higher number of segments can deliver accurate current flow measurement. With higher accuracy comes the requirement of higher computational power and speed. Furthermore, the method is a frequency domain technique. Therefore, multiple runs are required to obtain results for a wide bandwidth. This makes the MoM unsuitable for transient analysis [135]. The major drawback of the MoM is that, simulation of buried object in a medium is almost impossible or extremely difficult as it would require to determine an enormous number of unknowns. As a consequence, the modelling of a buried rebar in concrete cannot be undertaken with the MoM, making this technique inapplicable for this research [136].

With the FEM method, it is possible to analyze both uniform and non-uniform buried objects with desired electromagnetic properties [137]. Fine tetrahedral mesh setting

enables the FEM to refine its convergence criteria to model those complex geometries. However, being a frequency-domain based system does not allow the FEM to be suitable for transient analysis. Overall, the FEM is generally the slowest process compared to other techniques.

The FDTD method is the most reliable and sophisticated technique that can be implemented one, two or three dimensions. Buried objects in a medium can be modelled with ease by defining the dielectric properties of the cell structure [133]. This method is an intuitive time-domain method that does not require any matrix storage as the field equations are computed directly by solving the Maxwell's equations in time-stepping manner. Time-domain based system also means the capability of transient analysis and wide bandwidth results. Overall, the FDTD method is more complete and efficient algorithm in terms of computational power and time consumption [138]. Complex geometric structures can be distributed with no extra computation as modelling a multilayer dielectric medium requires no more extra computation time than modelling a single layer uniform medium.

Overall, MoM and FEA solvers that deal with dense and sparse matrix, the CPU time and memory requirement grow exponentially with increase in the total number of unknowns. For the FDTD, the requirements grow only linearly with the increase in cell numbers [139]. Therefore, the FDTD is the best selection amongst all the methods for solving large scale problem scenario. A summary of comparison between the most popular techniques can be found in Table 6-1.

Table 6-1. Summary of comparison between the modelling techniques.

Criteria	**MoM**	**FEM**	**FDTD**
Operation domain	Frequency-domain	Frequency-domain	Time-domain
Bandwidth limit	Requires multiple runs	Requires multiple runs	Wide band
Homogeneous media	Good	Good	Good
Inhomogeneous media	Bad	Average	Good
Buried object detection	Not capable	Complex procedure	Good
CPU time [138]	Good for less complex structures	Average	Average
Memory requirement [138]	Good	Bad	Good

6.3 A FDTD based framework for GPR modelling

Maxwell's electromagnetic equations that mathematically express the relations between the fundamental electromagnetic field quantities and their dependence on their sources can be used to describe all electromagnetic phenomena. The fundamental equations are:

$$\nabla \times E = -\frac{\mu_r}{C_0}\frac{\partial H}{\partial t} \tag{6.1}$$

$$\nabla \times H = \frac{\varepsilon_r}{C_0}\frac{\partial E}{\partial t} \tag{6.2}$$

where t is time in seconds, ε_r, μ_r are the relative permittivity, relative permeability of the medium respectively. These parameters, referred to as the constitutive parameters are functions of position, direction, the strength of the applied field and time and they couple the flux quantities with the electric and magnetic field intensities. From Equations (6.1) and (6.2), six three-dimensional partial differential equations of Maxwell's equations can be written as:

$$\frac{\partial E_x}{\partial z} - \frac{\partial E_z}{\partial x} = -\frac{1}{C_0}\left(\mu_{yx}\frac{\partial H_x}{\partial t} + \mu_{yy}\frac{\partial H_y}{\partial t} + \mu_{yz}\frac{\partial H_z}{\partial t}\right) \tag{6.3}$$

$$\frac{\partial E_y}{\partial x} - \frac{\partial E_x}{\partial y} = -\frac{1}{C_0}\left(\mu_{zx}\frac{\partial H_x}{\partial t} + \mu_{zy}\frac{\partial H_y}{\partial t} + \mu_{zz}\frac{\partial H_z}{\partial t}\right) \tag{6.4}$$

$$\frac{\partial E_z}{\partial y} - \frac{\partial E_y}{\partial z} = -\frac{1}{C_0}\left(\mu_{xx}\frac{\partial H_x}{\partial t} + \mu_{xy}\frac{\partial H_y}{\partial t} + \mu_{xz}\frac{\partial H_z}{\partial t}\right) \tag{6.5}$$

$$\frac{\partial H_x}{\partial z} - \frac{\partial H_z}{\partial x} = \frac{1}{C_0}\left(\varepsilon_{yx}\frac{\partial E_x}{\partial t} + \varepsilon_{yy}\frac{\partial E_y}{\partial t} + \varepsilon_{yz}\frac{\partial E_z}{\partial t}\right) \tag{6.6}$$

$$\frac{\partial H_y}{\partial x} - \frac{\partial H_x}{\partial y} = \frac{1}{C_0}\left(\varepsilon_{zx}\frac{\partial E_x}{\partial t} + \varepsilon_{zy}\frac{\partial E_y}{\partial t} + \varepsilon_{zz}\frac{\partial E_z}{\partial t}\right) \tag{6.7}$$

$$\frac{\partial H_z}{\partial y} - \frac{\partial H_y}{\partial z} = \frac{1}{C_0}\left(\varepsilon_{xx}\frac{\partial E_x}{\partial t} + \varepsilon_{xy}\frac{\partial E_y}{\partial t} + \varepsilon_{xz}\frac{\partial E_z}{\partial t}\right) \tag{6.8}$$

These equations need to be solved with regards to the geometry of the problem and its initial conditions in order to numerically model the GPR response from a particular target or set of targets. FDTD can be implemented to numerically solve Maxwell's equations by discretizing them in both the space and time continua. As a result, the resolution of spatial and temporal discretization steps plays a very significant role since higher resolution can provide the model a closer representation to a real-life scenario of the problem. However, in order to keep the computation time to a reasonable level, the values of the discretization step always have to be finite. Hence, the FDTD model represents a finite size of a discretized version of the real problem. The building block of this discretized FDTD grid was first proposed by Kane Yee [140] in his ground

breaking algorithm called the Yee cell. According to Yee, a point of space in a rectangular matrix and a function of space and time can be denoted as:

$$(i, j, k) = (i\Delta x, j\Delta y, k\Delta z) \tag{6.9}$$

$$F^n(i, j, k) = F(i\Delta x, j\Delta y, k\Delta z, n\Delta t) \tag{6.10}$$

Here Δx, Δy, and Δz are the space increments in the X, Y and Z axis respectively. Δt is the time increment and I, j, k, n are step integers. The sampling of electric (E) and magnetic (H) field components are carried out according to the Yee cell is illustrated in Figure 6-1. Within the cell, the E and H filed components are separated in space by half a space increment and in time by half a time-step. The E field is located on the edge of the cell for convenience because boundary conditions are usually more common on the E field than on the H field.

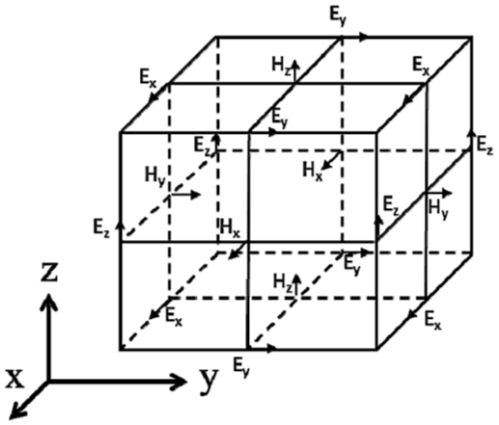

Figure 6-1. A 3D Yee cell proposed by Kane Yee [140].

The solutions of a general class of problem can be handled robustly using Yee algorithm which mimics the cyclic principle of a time varying E field producing a time vary H field and a time varying H field producing a time varying E field in turn. Within the cell, the E and H filed components are separated in space by half a space increment and in time by half a time-step. The E field is located on the edge of the cell for convenience because boundary conditions are usually more common on the E field than on the H field. Taking guides from a one-dimensional space-time chart of a Yee cell shown in Figure 6-2, the discretization equations of Maxwell's equations for the diagonal anisotropic material could be formulated.

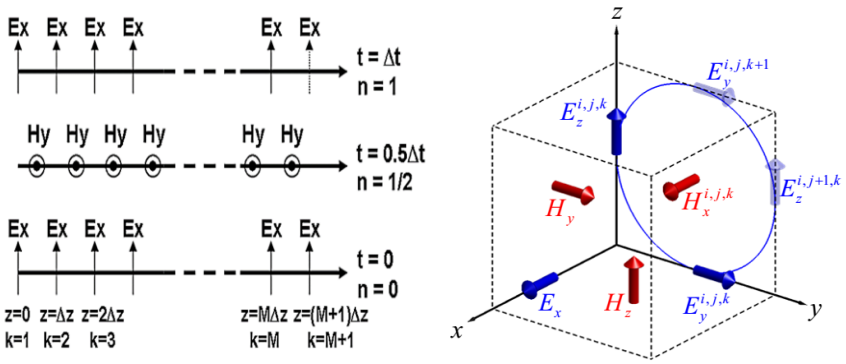

Figure 6-2. One dimensional and three-dimensional space-time chart of the Yee algorithm showing the space and time difference between the E and H fields.

$$\frac{E_x^{i,j,k+1}|_t - E_x^{i,j,k}|_t}{\Delta z} - \frac{E_z^{i+1,j,k}|_t - E_z^{i,j,k}|_t}{\Delta x} = -\frac{\mu_{yy}^{i,j,k}}{C_0}\frac{H_y^{i,j,k}|_{t+0.5\Delta t} - H_y^{i,j,k}|_{t-0.5\Delta t}}{\Delta t} \tag{6.11}$$

$$\frac{E_y^{i+1,j,k}|_t - E_y^{i,j,k}|_t}{\Delta x} - \frac{E_x^{i,j+1,k}|_t - E_x^{i,j,k}|_t}{\Delta y} = -\frac{\mu_{zz}^{i,j,k}}{C_0}\frac{H_z^{i,j,k}|_{t+0.5\Delta t} - H_z^{i,j,k}|_{t-0.5\Delta t}}{\Delta t} \tag{6.12}$$

$$\frac{E_z^{i,j+1,k}|_t - E_z^{i,j,k}|_t}{\Delta y} - \frac{E_y^{i,j,k+1}|_t - E_y^{i,j,k}|_t}{\Delta z} = -\frac{\mu_{xx}^{i,j,k}}{C_0}\frac{H_x^{i,j,k}|_{t+0.5\Delta t} - H_x^{i,j,k}|_{t-0.5\Delta t}}{\Delta t} \tag{6.13}$$

$$\frac{H_x^{i,j,k}|_{t+0.5\Delta t} - H_x^{i,j,k-1}|_{t+0.5\Delta t}}{\Delta z} - \frac{H_z^{i,j,k}|_{t+0.5\Delta t} - H_z^{i-1,j,k}|_{t+0.5\Delta t}}{\Delta x} = \frac{\varepsilon_{yy}^{i,j,k}}{C_0}\frac{E_y^{i,j,k}|_{t+\Delta t} - E_y^{i,j,k}|_t}{\Delta t} \tag{6.14}$$

$$\frac{H_y^{i,j,k}|_{t+0.5\Delta t} - H_y^{i-1,j,k}|_{t+0.5\Delta t}}{\Delta x} - \frac{H_x^{i,j,k}|_{t+0.5\Delta t} - H_x^{i,j-1,k}|_{t+0.5\Delta t}}{\Delta y} = \frac{\varepsilon_{zz}^{i,j,k}}{C_0}\frac{E_z^{i,j,k}|_{t+\Delta t} - E_z^{i,j,k}|_t}{\Delta t} \tag{6.15}$$

$$\frac{H_z^{i,j,k}|_{t+0.5\Delta t} - H_z^{i,j-1,k}|_{t+0.5\Delta t}}{\Delta y} - \frac{H_y^{i,j,k}|_{t+0.5\Delta t} - H_y^{i,j,k-1}|_{t+0.5\Delta t}}{\Delta z} = \frac{\varepsilon_{xx}^{i,j,k}}{C_0}\frac{E_x^{i,j,k}|_{t+\Delta t} - E_x^{i,j,k}|_t}{\Delta t} \tag{6.16}$$

In this chapter, problems composed of dielectric layers will be modelled in just one dimension. In this case, the materials and the fields are uniform in any two directions, hence, derivatives in these uniform directions will be zero. If the uniform directions are to be the X and Y axis, then the electromagnetic wave propagation behaviour along the Z axis would be as in Figure 6-3.

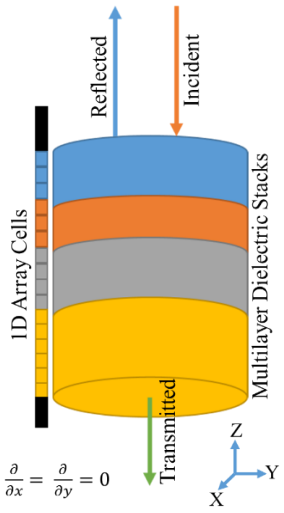

Figure 6-3. 1D array of a Yee cell.

Therefore, the three dimensional equations from (6.11) to (6.16) could be scaled down to one-dimensional equation by substituting $\Delta x = \Delta y = 0$. Here, the longitudinal field components, E_z and H_z are always found to be zero and the Maxwell's equations decouples into four equations as:

$$\frac{E_x^{i,j,k+1}|_t - E_x^{i,j,k}|_t}{\Delta z} = -\frac{\mu_{yy}^{i,j,k}}{C_0}\frac{H_y^{i,j,k}|_{t+0.5\Delta t} - H_y^{i,j,k}|_{t-0.5\Delta t}}{\Delta t} \tag{6.17}$$

$$-\frac{H_y^{i,j,k}|_{t+0.5\Delta t} - H_y^{i,j,k-1}|_{t+0.5\Delta t}}{\Delta z} = \frac{\varepsilon_{xx}^{i,j,k}}{C_0}\frac{E_x^{i,j,k}|_{t+\Delta t} - E_x^{i,j,k}|_t}{\Delta t} \tag{6.18}$$

$$\frac{E_y^{i,j,k+1}|_t - E_y^{i,j,k}|_t}{\Delta z} = \frac{\mu_{xx}^{i,j,k}}{C_0}\frac{H_x^{i,j,k}|_{t+0.5\Delta t} - H_x^{i,j,k}|_{t-0.5\Delta t}}{\Delta t} \tag{6.19}$$

$$\frac{H_x^{i,j,k}|_{t+0.5\Delta t} - H_x^{i,j,k-1}|_{t+0.5\Delta t}}{\Delta z} = \frac{\varepsilon_{yy}^{i,j,k}}{C_0}\frac{E_y^{i,j,k}|_{t+\Delta t} - E_y^{i,j,k}|_t}{\Delta t} \tag{6.20}$$

Equations (6.17) and (6.18) together is called the E_x/H_y mode and equations (6.19) and (6.20) together is called the E_y/H_x mode. These two modes will propagate independently in physical medium. However, numerically they are same and will exhibit identical electromagnetic behaviour. Therefore, it is only necessary to solve just only one mode. In this chapter, E_x/H_y mode is solved for numerical modelling. Therefore, two update equations for E_x/H_y mode and basic framework for 1D FDTD for GPR can be rewritten as:

$$E_x^{i,j,k}|_{t+\Delta t} = E_x^{i,j,k}|_t + \left(\frac{C_0\Delta t}{\varepsilon_{xx}^{i,j,k}}\right)\left(\frac{H_y^{i,j,k}|_{t+0.5\Delta t} - H_y^{i,j,k-1}|_{t+0.5\Delta t}}{\Delta z}\right) \tag{6.21}$$

$$H_y^{i,j,k}|_{t+0.5\Delta t} = H_y^{i,j,k}|_{t-0.5\Delta t} - \left(\frac{C_0\Delta t}{\mu_{yy}^{i,j,k}}\right)\left(\frac{E_x^{i,j,k+1}|_t - E_x^{i,j,k}|_t}{\Delta z}\right) \tag{6.22}$$

A high level programming language such as Matlab where the array indices can be declared, a script can be developed by following the bare bone structure of the proposed 1D FDTD algorithm as in Figure 6-4.

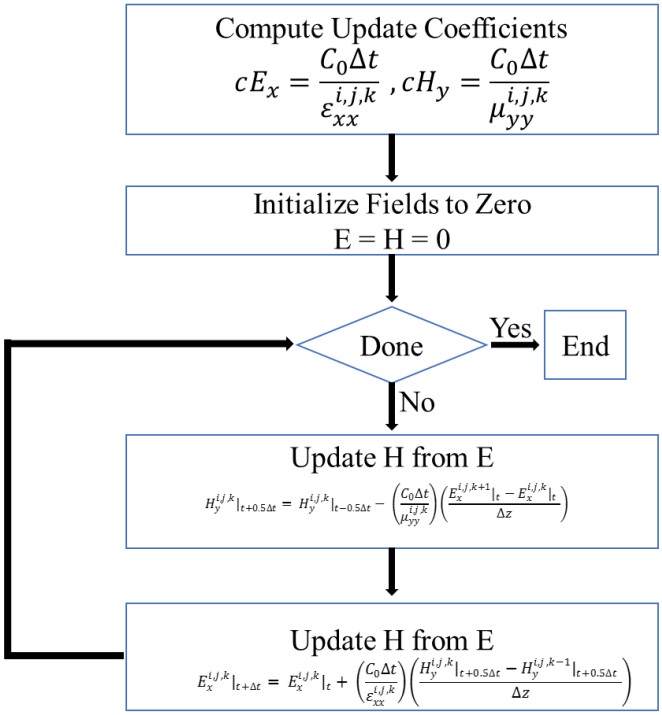

Figure 6-4. Proposed numerical framework for 1D FDTD algorithm.

6.3.1 Source

Energy in the form of Gaussian or sinusoidal wave is injected into the grid cell to initiate the FDTD algorithm. The source is usually assigned as values to E_x at the boundary z = 0, k = 1. In order to simulate a broad range of frequencies, pulses in Gaussian form are widely used. A Gaussian pulse centred at t_c can be defined by,

$$g(t) = e^{-(t-t_c)/2\sigma^2} \tag{6.23}$$

It is a good practice to have t_c = 5×pulse width/2 so that the Gaussian pulse is centred at half of the total 5 cycles of the signal and σ can be determined by:

$$\sigma = \frac{t_c}{pulse\ width, \tau} \tag{6.24}$$

Other derivatives of the Gaussian pulse such as monocycle, doublet and so can be derived from the Equation (6.23). For example, in order to reduce the error and high frequency at the beginning of the simulation, a modulated Gaussian pulse can be formed by multiplying the Equation (6.23) with a sinusoidal wave equation as:

$$E_x(t) = \sin(2\pi f_0 t)\, e^{-(t-t_c)/2\sigma^2} \tag{6.25}$$

The resultant modulated Gaussian pulse can be seen in Figure 6-5.

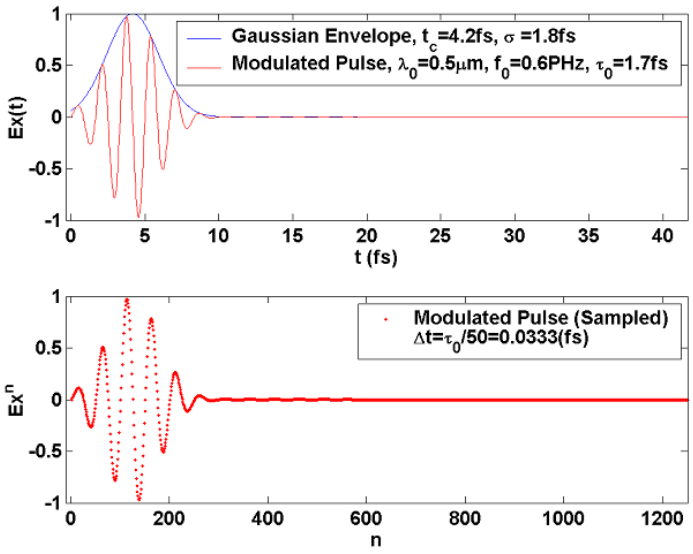

Figure 6-5. Modulated Gaussian pulse using 0.6 PHz sinusoidal wave.

6.3.2 Boundary conditions

Modelling open boundary problems like GPR faces an issue of truncation of the computational domain at a finite distance from the sources and targets as the electromagnetic fields cannot be calculated directly by the numerical method at the boundary. As FDTD 1D array has a finite number of cells, the outgoing Gaussian pulse will come to the edge of the model after certain period. If any special boundary condition is not defined, then unpredictable reflections would be generated at the boundary that would go back inward and as a result, there will be no way of determining real wave from the reflected one. The reflections are due to the intrinsic impedances of the media boundary and a solution is to make an adaptation, such ABC between them that the reflection coefficient would be zero and no reflection would occur [141]. These ABC's will absorb any wave hitting the boundaries, hence will emulate an infinite space. In FDTD as the fields at the edge are propagating outward and it takes two time steps for the field to cross one cell therefore, the field value at the end can be estimated by the following equation:

$$E_x^k(n) = E_x^{k-2}(n+1) \tag{6.26}$$

The simple way to implement this is to store a value of $E_x(1)$ for two time steps and then put it in $E_x(0)$. However, numerical imperfections might exist in ABC and reflections might still travel backward from the termination of medium at the truncation boundaries of the model. But they are easily distinguishable from the actual reflections from targets inside the model as those reflections will have significantly small amplitude compared to target reflections.

6.3.3 Total Field/Scattered Field

The source equations described earlier are for two directional sources, whereas, total-field/scattered-field (TF/SF) is a technique to inject a one directional source. Any system grid could be divided into two regions as shown in Figure 6-6 where, the total field contains the source field and the field scattered from any target. But the scattered field can pass through source injecting point transparently into the scattered field region. This ensures waves at the boundaries are only travelling outwards and entire energy injected by the source is incident on the medium that is being simulated.

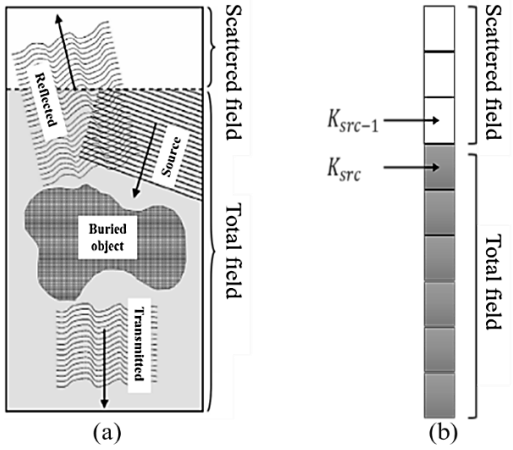

Figure 6-6. EM wave propagation in a TF/SF grid.

To implement TF/SF, a point of source, k_{src} as in Figure 6-6(b) needs to be declared which divides the scattered field and total field. If field types are the same on both sides of the injection point (both scattered or both total) then the Equations (6.21) - (6.22) can be used to update the corresponding field in time. However, as the field on the top of the source injection point is intended to be the scattered field and the bottom to be the total field, E and H field update equations at k_{src} point becomes,

$$E_x^{i,j,ksrc}|_{t+\Delta t} = E_x^{i,j,ksrc}|_t + \left(\frac{C_0\Delta t}{\varepsilon_{xx}^{i,j,ksrc}}\right)\left(\frac{H_y^{i,j,ksrc}|_{t+0.5\Delta t} - H_y^{i,j,ksrc-1}|_{t+0.5\Delta t}}{\Delta z}\right) \quad (6.27)$$

$$H_y^{i,j,ksrc-1}|_{t+0.5\Delta t} = H_y^{i,j,ksrc-1}|_{t-0.5\Delta t} - \left(\frac{C_0\Delta t}{\mu_{yy}^{i,j,ksrc}}\right)\left(\frac{E_x^{i,j,ksrc}|_t - E_x^{i,j,ksrc-1}|_t}{\Delta z}\right) \quad (6.28)$$

Looking at the E_x field update Equation (6.27) which is located on the total field side, the term $H_y^{i,j,ksrc-1}|_{t+0.5\Delta t}$ is located on the scattered field side. For consistency, all terms of an update equation should be located on the same side of fields. Therefore, a magnetic field source is added to the term to turn all terms to total-field quantities and the update equation become,

$$E_x^{i,j,ksrc}|_{t+\Delta t} = E_x^{i,j,ksrc}|_t + \left(\frac{C_0\Delta t}{\varepsilon_{xx}^{i,j,ksrc}}\right)\left[\frac{H_y^{i,j,ksrc}|_{t+0.5\Delta t} - \left(H_y^{i,j,ksrc-1}|_{t+0.5\Delta t} + H_y^{i,j,ksrc-1}|_{t+0.5\Delta t}^{src}\right)}{\Delta z}\right] \quad (6.29)$$

Likewise, in Equation (6.28) which is located on the scattered field side has a term, $E_x^{i,j,ksrc}|_t$ from the total field side. To convert all the terms to scattered field quantities, an electric field is subtracted from the term as below,

$$H_y^{i,j,ksrc-1}|_{t+0.5\Delta t} = H_y^{i,j,ksrc-1}|_{t-0.5\Delta t} - \left(\frac{C_0\Delta t}{\mu_{yy}^{i,j,ksrc}}\right)\left[\frac{\left(E_x^{i,j,ksrc}|_t - E_x^{i,j,ksrc}|_t^{src}\right) - E_x^{i,j,ksrc-1}|_t}{\Delta z}\right] \quad (6.30)$$

The above formulations show that original update equations (6.21), (6.22) stays the same with added correction term $H_y^{i,j,ksrc-1}|_{t+0.5\Delta t}^{src}$ and $E_x^{i,j,ksrc}|_t^{src}$ in equations (6.29), (6.30) which needs to be redefined. The way to achieve those correction terms is to define the field, E_x which is a Gaussian pulse as equation (6.23) in this case and then derive the H field source with a phase shift, H_y using Maxwell's equations. So from Maxwell's equations,

$$E_x^{i,j,ksrc}|_t^{src} = g(t) \quad (6.31)$$

$$H_y^{i,j,ksrc-1}|_{t+0.5\Delta t}^{src} = \sqrt{\frac{\varepsilon_r^{i,j,ksrc}}{\mu_r^{i,j,ksrc}}}\, g\left(t + \frac{n_{src}\Delta z}{2\times C_0} - \frac{\Delta t}{2}\right) \quad (6.32)$$

Where, $\sqrt{\frac{\varepsilon_r^{i,j,ksrc}}{\mu_r^{i,j,ksrc}}}$ is the amplitude of the magnetic field based on Maxwell's equations, n_{src} is the refractive index of the medium at the point of source injection and $\frac{\Delta t}{2}$ is the phase shift with the electric field. The corresponding electric and magnetic field is shown in Figure 6-7 which shows a phase shift of 3.7 ps for a 1 GHz Gaussian pulse.

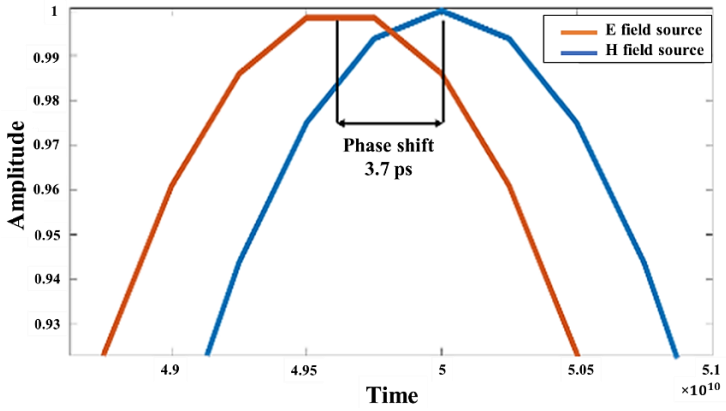

Figure 6-7. Correlation between E field and H field sources.

6.3.4 Propagation in a lossy medium

The E and H field update equations derived in the previous sections are for free space medium only and any loss term is neglected. However, to model a realistic GPR, the loss term of the medium must be incorporated in the update equations. In many media, loss term is specified by the conductivity, σ. This loss term result in the attenuation of the propagating energy of the electromagnetic wave through the medium. Maxwell's curl equations to incorporate conductivity is,

$$\nabla \times H = \eta_0 \sigma E + \frac{\varepsilon_r}{C_0} \frac{\partial E}{\partial t} \tag{6.33}$$

Here, η_0 is the free space impedance. By discretizing and taking the spatial derivatives of the Equation (6.33) in the same way as described previously, the new update equation can be formulated as:

$$E_x^{i,j,k}|_{t+\Delta t} = \left(\frac{2\varepsilon_0 \varepsilon_{xx}^{i,j,k} - \Delta t \sigma_{xx}^{i,j,k}}{2\varepsilon_0 \varepsilon_{xx}^{i,j,k} + \Delta t \sigma_{xx}^{i,j,k}}\right) E_x^{i,j,k}|_t + \left(\frac{2\varepsilon_0 c_0 \Delta t}{2\varepsilon_0 \varepsilon_{xx}^{i,j,k} + \Delta t \sigma_{xx}^{i,j,k}}\right)\left(\frac{H_y^{i,j,k}|_{t+0.5\Delta t} - H_y^{i,j,k-1}|_{t+0.5\Delta t}}{\Delta z}\right) \tag{6.34}$$

If conductivity, σ is set to zero in Equation (6.34) then the equation reverts to the initial equation (6.21). Moreover, incorporating conductivity term into the system does not affect the H field update equation therefore, Equation (6.22) remains the same. The pseudo programming code for the final E and H field update equations could be written as:

$$E_x[k] = (cE_{x1})E_x[k] + (cE_{x2})\big(H_y[k-1] - H_y[k]\big)/dz \tag{6.35}$$

$$H_y[k] = H_y[k] - \big(cH_y\big)(E_x[k+1] - E_x[k])/dz \tag{6.36}$$

Here, cE_{x1}, cE_{x2}, cH_y are the constant coefficients and they could be calculated before the final loop of the program starts. The final numerical framework of FDTD could be achieved by combining all the steps outlined to obtain a working GPR model. The field propagation behaviour and modelling of materials with different permittivity, permeability and conductivity can be achieved and visualized in Matlab. The final numerical framework is shown in Figure 6-8.

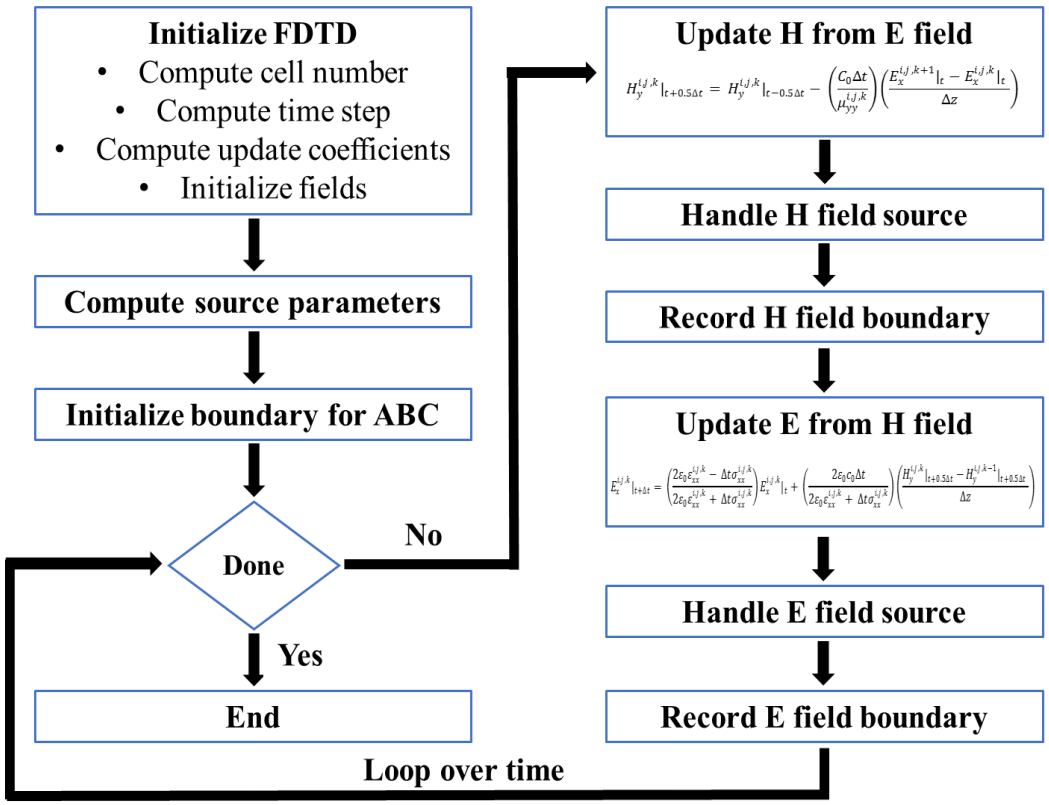

Figure 6-8. Final proposed FDTD algorithm for GPR modelling.

6.4 Matlab implementation and analysis

A FDTD code was written using the numerical framework developed in the previous sections. A perfect absorbing boundary condition was implemented so that the code can be easily parallelized, allowing operation in an infinite medium. The simulation was done on a 3078 cell z-axis grid system with space discretization size, $\Delta z = 0.003$ m and time step, $\Delta t = 5.5$ ps.

6.4.1 Validation of the ABC

A lossless dielectric medium with $\varepsilon_r = 1$ was simulated first where the Gaussian pulse with centre frequency of 1.5 GHz was injected at cell number 385 along the dotted vertical line that travels outward. Propagation of both E and H fields are shown in Figure 6-9. Total number of iterations was 19068 which is 3 times higher than required for total convergence of the simulation. At 5650^{th} iteration, the EM wave hits the boundary line. But as the boundary is perfectly absorbing therefore, the wave does not reflect after hitting the boundary. As the wave completely passes the problem window at later iterations, there is no reflected wave present which validates successful implementation of ABC.

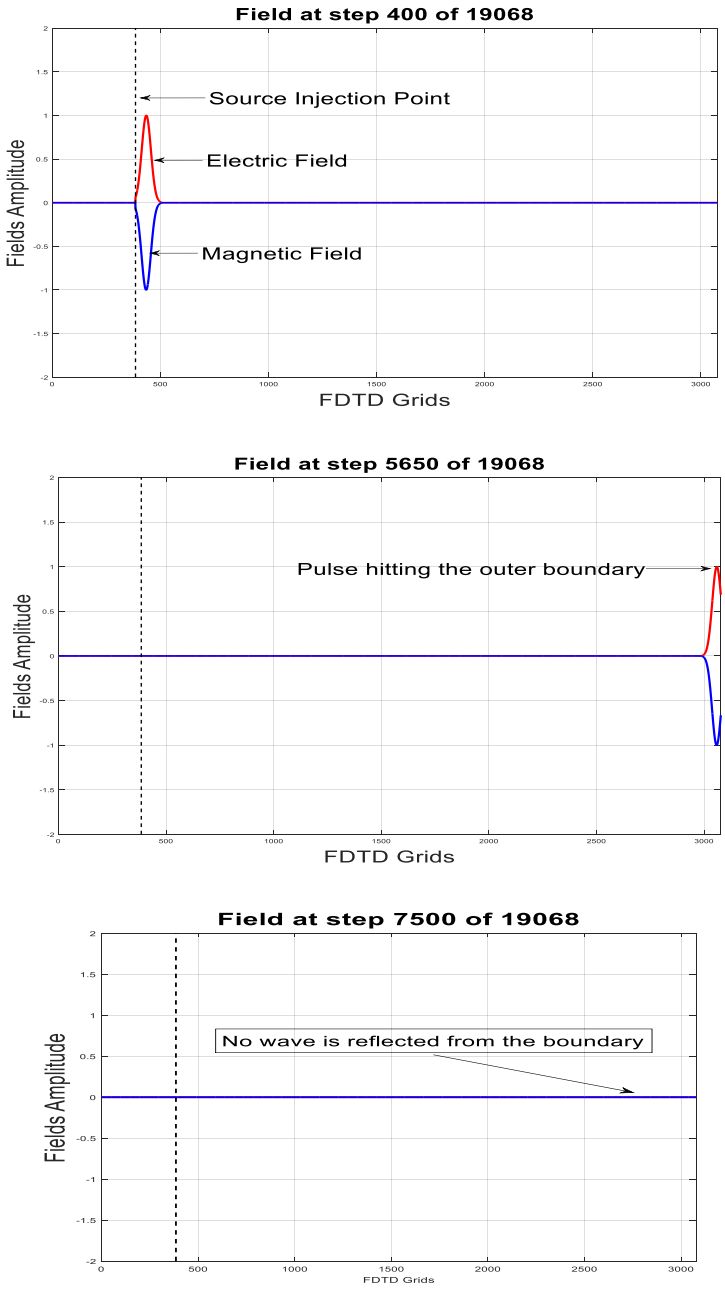

Figure 6-9. EM wave propagation through the ABC.

6.4.2 Propagation through a dielectric medium

Figure 6-10 shows the simulation of the Gaussian pulse propagation, first in the air and then in the dry sand with dielectric constant of $\varepsilon_r = 6$ after crossing the air – sand interface at cell number 1570. When the wave encounters the dielectric medium, a part of it is transmitted and the other part is reflected. Moreover, the wavelength in the sand is shorter that the wavelength in air also the electric field amplitude reduces and changes polarity as the wave enters the sand medium. Furthermore, by calculating the time difference between the incident wave and reflected wave at the source injection point,

the distance of the air-sand interface from source point could be determined, this is a fundamental feature of GPR.

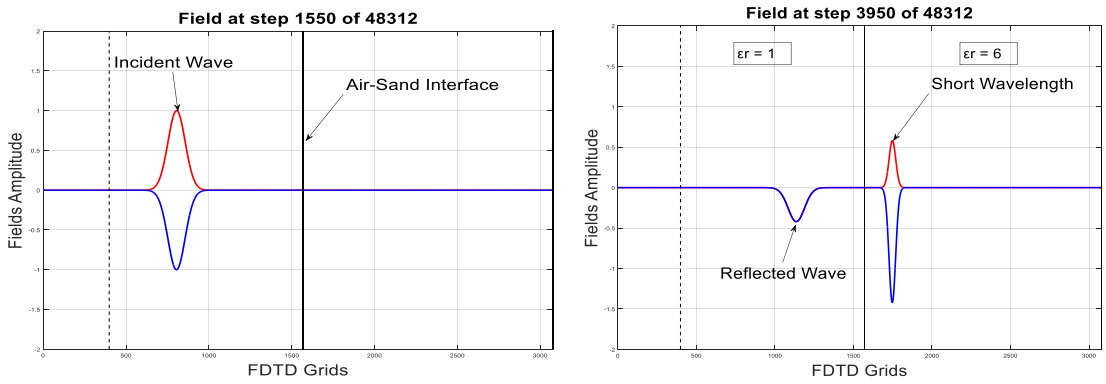

Figure 6-10. Simulation of Gaussian wave propagation on a medium of relative dielectric constant of 6.

Simulation of the same setup using a sinusoidal wave reveals the effect of change in dielectric constant on the transmitted pulse wavelength. A sinusoidal incident wave 700 MHz passing through a medium with $\varepsilon_r = 6$ also reveals that as soon as the wave hits the medium with higher dielectric constant, the wavelength shortens as in Figure 6-11.

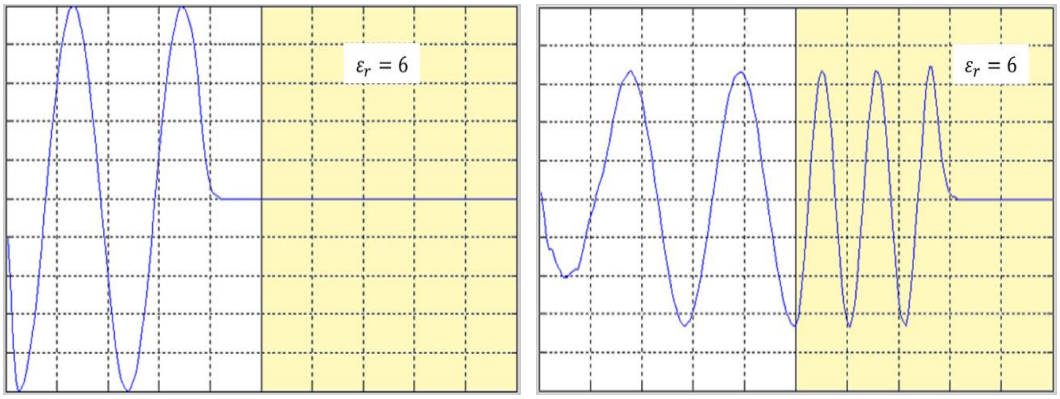

Figure 6-11. Simulation of propagation of a 700 MHz sinusoidal incident wave on a medium of relative dielectric constant ε_r=6.

6.4.3 Simulation of a reinforced concrete wall

FDTD was implemented to simulate a real-life application of GPR to detect reinforced buried rebar on a concrete wall. The medium used in the simulations corresponds to a homogenous medium (dry concrete with dielectric properties $\varepsilon_r = 5.5$, $\sigma = 0.043$ S/m). First a 1 m thick concrete wall was modelled in the system to observe wave propagation behaviour on a lossy concrete medium. The space discretization, Δz was set to 0.0014m and time step, Δt to 2.3 ps. Length of the total model was 8.6 m simulated with a centre frequency of 1.5 GHz. Figure 6-12 shows the model setup and

it is noticeable that, a part of the wave reflected from the air-concrete interface and also the magnitude of the transmitted wave attenuates this time in the medium. This feature simulates the characteristic of any lossy medium.

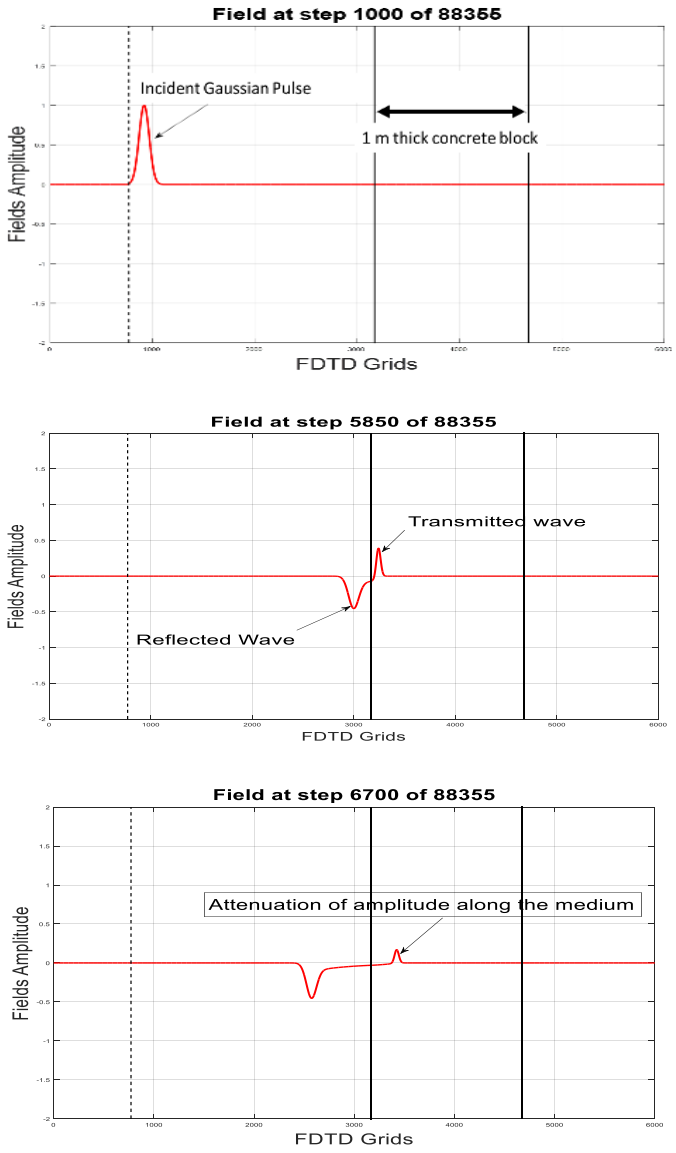

Figure 6-12. Propagation of EM pulse in a lossy concrete medium.

Next, a steel rebar was planted in the concrete block. Steel is a highly conductive metal, and as a result, the electric field value inside steel or any conductive metal is zero. Therefore, it should have infinite dielectric constant i.e., acts as perfect electric conductor. But ideally, no metals are perfect conductor as they have a portion of impurity in them. The permittivity for real metal is purely negative with very small imaginary part. At high frequency region, steel will reflect 100% of the electromagnetic wave as electromagnetic wave cannot penetrate the metal, and the wave is exponentially decayed inside the surface of the metal. The imaginary part represents the absorption

of a part of the wave energy. However, high conductivity value of steel ($\sigma = 10^6$ S/m) negates the effect of imaginary part of the overall simulation result. To model the steel, dielectric constant value of −1 is used in the codes. In the simulation setup as Figure 6-13, a steel rebar of 10 cm diameter is located under a 30 cm concrete cover. The distance between electric field transmitter and air-concrete interface is 3.35 m.

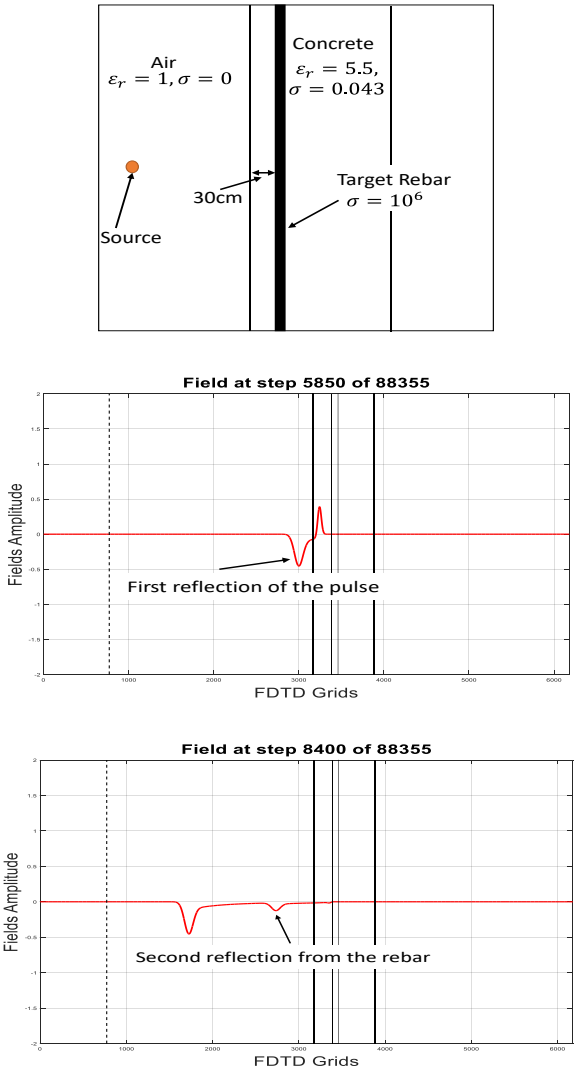

Figure 6-13. Reflection of pulses from the air-concrete interface and the rebar.

From the wave propagation behaviour, it is seen that there are two reflected pulses - one from the air-concrete interface and the other from the steel rebar. Also, there is transmitted wave present on right side of the rebar which indicates that 100% of the wave has been reflected although with reduced amplitude. By measuring the ToF of the two reflected pulses, the thickness of the concrete cover can be determined.

In FDTD algorithm, electromagnetic wave propagates one cell in two time steps and recorded two-way travel time of the reflected pulses in Matlab are, 1st reflected pulse

= 2.26 × 10^{-8} s, 2nd reflected pulse = 2.46 × 10^{-8} s. Therefore, time difference between the two reflected pulses to reach back the source injection point is 0.1×10^{-8} s. Using pulse velocity method equation, $distance = velocity \times travel\ time$, the concrete cover is measured to be 0.3 m where pulse velocity is the speed of electromagnetic pulse (3.9×10^{8} ms^{-1}). This measured concrete cover completely matches with the initial simulation model setup.

6.5 Chapter summary

Simulation techniques offer a fast way to analyze different configurations and parameters of a GPR system. A numerical framework based on FDTD algorithm developed through this research can help to model response behaviour of a GPR under different test conditions by simply changing some material properties in the code settings without remaking the entire system or moving to a different environment. The use of simulations allows changing a specific parameter of the test environment and then looking for the most optimized performance. These results can then be compared to the developed prototype GPR system to check for correct behaviour. This chapter demonstrate the robustness and versatility of FDTD method in simulation GPR responses. The EM wave propagation in different media showed that the amplitude of the wave deteriorates significantly in the medium with lossy conductivity. It also displayed the effect of electrical properties of the medium on wave propagation. In general, the time-domain data obtained was successful to detect a buried object based on reflected wave and the by measuring time-of-flight of the reflected wave, the depth of the object was successfully calculated.

Chapter 7. GPR prototype design and experimentation

This chapter describes the development process of a prototype GPR. This involves the fabrication of the miniaturized dipole antennas and the GPR pulse generator. The signal processing is done based on the time-domain signals received from the receiving antenna. This chapter is structured in the following sections:

7.1 Overview

This chapter focuses on the development process of a prototype GPR. Based on the discussion of GPR components in chapter 5, the objective of this chapter is to describe the development process of a prototype GPR. The system contains a trigger circuit, avalanche transistor based pulse generator and pulse shaping circuit to form the nanosecond pulse generator. The trigger circuit utilizes the advancement in emitter coupled logic (ECL) gate technology with fast pulse rise and fall time (less than 200 ps). A programmable delay line (PDL) is used to generate two out of phase pulses that pass through an ECL XOR gate to generate a trigger pulse. This narrow pulse triggers an avalanche transistor capable to generate pulses in nanosecond range width. The output Gaussian pulse is 5 V in peak-to-peak and tuneable from pulse width tuneable from 750 ps to 10 ns.

Furthermore, antennas are another essential component of a GPR system for transmission and reception of the EM waves. Efficient emitting and receiving of electromagnetic energy is ensured by high antenna gain as antennas with a high gain improve the signal-to-noise ratio [29]. As physical size and gain of antennas are determined by the operating frequency, therefore small antennas offer compact system dimension for high frequency applications. However, small antennas have a low gain at lower frequency regions therefore, larger antennas are required to operate at lower frequencies. Various types of antennas are used for GPR systems, but dipole and bow-tie antennas are the most common as they are easy to fabricate on a variety of substrates because of planer surface structure [142]. Theoretically, the length of a dipole antenna is half of its lowest operating wavelength. Few examples of dipole antennas utilized for low frequency GPR scanning operations can be seen in Figure 7-1. Due to the low frequency operation, the antenna size is quite an issue since the antenna size determines the whole system size and portability.

Figure 7-1. Archaeological GPR scanning with 100 MHz unshielded and shielded dipole antenna [143].

Therefore, a novel antenna miniaturized technique is presented here and applied to 100 MHz and 200 MHz conventional dipole antenna respectively. The technique is first implemented using Agilent ADS software platform to establish the optimum antenna design parameters to achieve maximum reduction in antenna dimension. Consequently, two prototype antennas have been fabricated for design validation.

Lastly, the fabricated antenna and the pulse generator are integrated with the climbing robot to construct a climbing robotic GPR platform. The robot's climbing capability as well as the detection capability of the GPR has been analysed experimentally both in time-domain spectrum. Currently, there is an inaccessibility of an efficient and cost effective survey technique since all commercially available GPR systems such as StructureScan and UtilityScan from GSSI, GroundExplorer from Mala shown in Figure 7-2 can cost up to tens of thousands of pounds. Also, specially trained operators are needed for on-field radar data interpretation. Therefore, the key deliverable of this chapter is a working robotic GPR prototype to demonstrate the proof of concept that can guide towards the design of a low cost simplified GPR system.

Figure 7-2. Commercial StructureScan and GroundExplorer GPR.

7.2 Design of a Gaussian pulse generator

For GPR systems, the pulse generator plays a crucial role in overall system performance. Narrow-width pulse could provide higher time resolution and detection capabilities. A pulse generator of fixed pulse width is used for typical GPR system and pulses usually take the shape of step, Gaussian or higher derivative of Gaussian pulse. These pulses have very wide instantaneous bandwidth with no DC components. It simplifies the design process of antennas, amplifiers and receivers. These pulse types have better impedance matching with the transmitting antenna and produce less distortion for the transmitting and receiving signals [144].

However, for the advancement of GPR technology, a pulse-width tuneable pulse generator is essential for proper characterization of ground permittivity and

conductivity of different ground thicknesses [145]. A conventional system has the limitation of adapting to test conditions such as environment, moisture content etc. as the transmitting pulse width and magnitude cannot be adjusted. A narrow pulse width signal has large bandwidth and time resolution but suffers from high propagation loss in the medium. Wide pulse width signal on the contrary, has high power spectral density and good penetration capability but provides low bandwidth. Therefore, a tuneable GPR pulse generator is crucial for a GPR to operate at different frequencies for different ground and test conditions. The relationship between the pulse width and spectrum density is given in Figure 7-3.

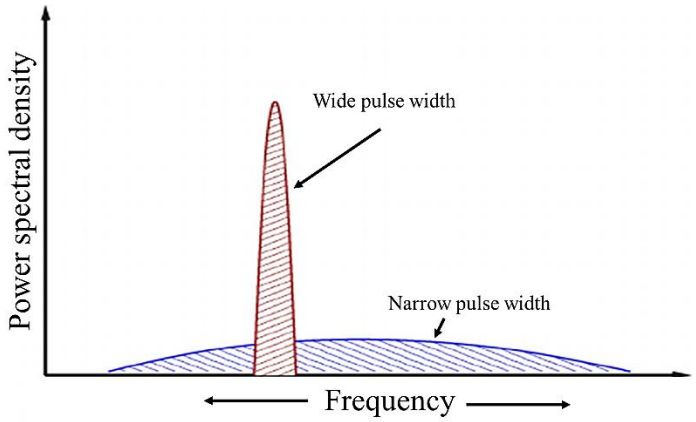

Figure 7-3. Power spectral density of variable pulse width.

The pulse generator proposed in this research can deliver a pulse-width tuning facility to set specific GPR configuration suited for different inspection environments. The proposed pulse generator circuit block diagram is shown in Figure 7-4. The first stage is the external clock pulse that is sharpened for a well-defined nanosecond pulse at the output stage.

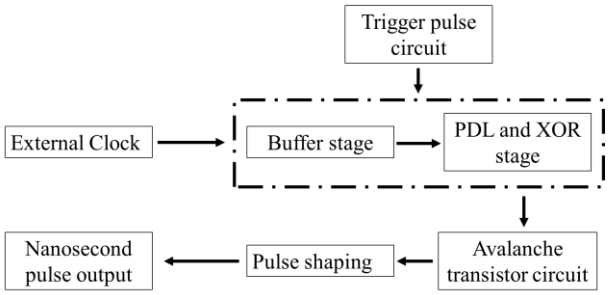

Figure 7-4. Block diagram of the proposed UWB pulse generator.

7.2.1 Trigger pulse circuit

The trigger pulse circuit is activated by an external clock. Here, the external clock is generated by a LTC1799 VCO that outputs square waves at 1 MHz frequency with

pulse rise and fall time of 14 ns. The frequency of this VCO could be varied up to 33 MHz which will ultimately decide the PRF of the GPR pulse output. As low pulse rise and fall time value ensures higher pulse bandwidth, pulses produced by the VCO is passed through two separate buffer logic gates to generate two separate signals with reduced pulse rise and fall time. The implemented SY100EP11UZG ECL buffer logic gate is manufactured by Micrel. This buffer logic gate outputs pulses with rise and fall time of only 120 ps. The transient response of the VCO and buffer logic pulses in Figure 7-5 shows that the buffer output pulse has a sharp rising while the VCO pulse is suffering from a slow rising period.

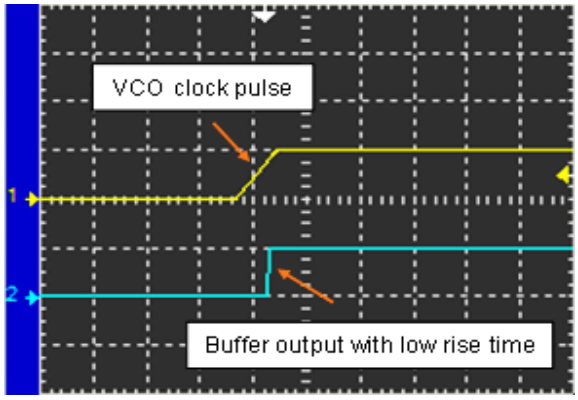

Figure 7-5. Transient response of the VCO and Buffer pulses.

Pulses outputted by the two buffer gates are then fed through two separate PDL to generate relative delay between these two pulses. The type of PDL used is DS1124U manufactured by Maxim Integrated that can generate relative delay of up to 84 ns between the input and output pulse and has pulse rise and fall time of 220 ps. It has three programmable pins that is used to vary the delay from 20 ns ns to 84 ns in 250 ps increments. Therefore, timing between two output pulses from the PDL is set such a way that delay is variable up to 10 ns in 250 ps resolution. To achieve this, first PDL time delay is set fixed to 20 ns. The second PDL time delay is varied between 20 ns and 30 ns in 40 steps at 250 ps delay resolution. These features make it possible to fine-tune the output Gaussian pulse width as desired.

During the final stage of the trigger circuit, two pulses are compared at a ECL XOR gate to generate pulses of as low as 1 ns width. XOR gate model MC10EP08DTG from On Semiconductor is used which has a propagation delay of only 250 ps between its input and output with 130 ps pulse rise and fall time. The rise time value of the chosen PDL is crucial as rise time greater than 250 ps seriously limits the XOR gate's capability to distinguish its two input pulses. Moreover, XOR's own short rise time of 130 ps

preserves the high bandwidth of the pulses. Figure 7-6 represents the timing diagram of the trigger pulse circuit where XOR extracts the avalanche circuit trigger pulse from two delayed PDL pulses.

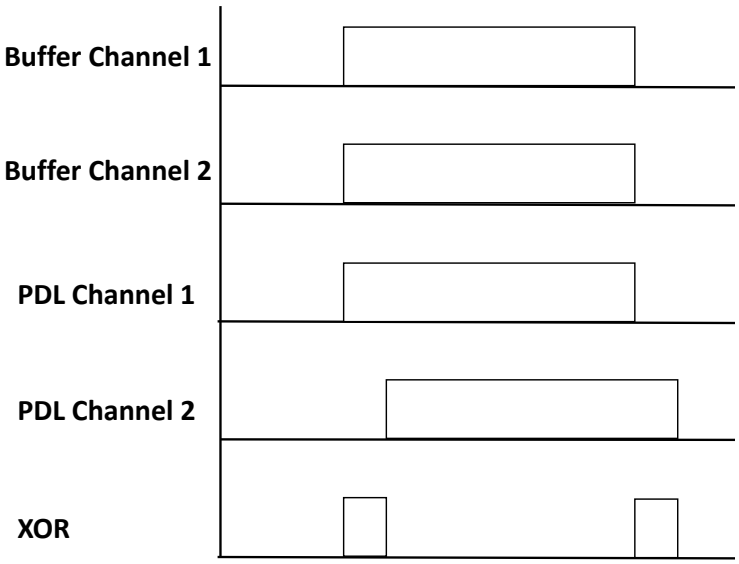

Figure 7-6. Timing diagram of different stages of the trigger pulse circuit.

7.2.2 Avalanche pulse forming circuit

This avalanche circuit block is the core element of the proposed UWB pulse generator that consists of a NPN bipolar junction transistor (BJT) operated in the avalanche mode. The basic requirement for a transistor to operate in avalanche mode is that there must be a significant difference between the collector-to-base voltage, BV_{CBO} and the avalanche breakdown voltage, BV_{CEO} as shown in Figure 7-7. When the circuit is not triggered, the base is on zero bias and the avalanche transistor operates in cut-off region. When there is a high voltage applied between the collector and emitter junction, a strong electric field is produced on the collector junction because of the strong electric field. As a result, electron hole pairs form in succession within that region. Newly generated electron and holes will move in the opposite direction of the original ones and this causes collision between them. When gaining enough power, new electrons and holes accelerate the movement and repeat the above process and produce more electron hole-pairs. This increased number of electron-hole pairs increases the collector current sharply like avalanche and this phenomenon is called the avalanche multiplication effects [146]. During the avalanche operation, the relationship between collector current, i_c and emitter current, i_e can be written as:

$$i_c = \alpha M i_e \tag{7.1}$$

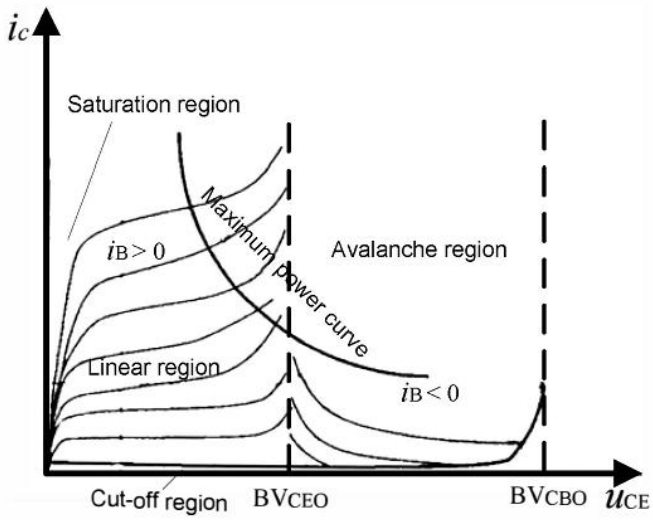

Figure 7-7. Avalanche transistor operation characteristics [146].

Where, α is the current amplification factor and M is the avalanche multiplication factor in the avalanche area. The parameter M emphasis that if one current carrier enters the collector charge region; M number of current carriers will overflow the collector charge region. Avalanche multiplication factor, M can be represented as [147]:

$$M = \frac{1}{1 - (\frac{U_{CE}}{BV_{CBO}})^m} \tag{7.2}$$

Here, m is the miller factor which is related to the transistor material. For example, for silicon transistor, the value of m is between 3 and 4.

During avalanche mode operation, negative resistance characteristics appear between the collector and emitter junction due to the continuous collector current increase. As the current reaches a critical point '*a'*, the phenomenon of secondly breakdown occurs as Figure 7-8 [148]. If the circuit is driven properly, working point 'a' will reach point 'c' by passing the region 'b' which is a negative resistance area. As the drive current capacity of the avalanche transistor is high, the working point will drive to '*e*' from '*c*' through the second negative resistance area '*d*'. As during the transition between point '*a*' to '*e*', the avalanche transistor has to pass through two negative resistance areas, therefore, the voltage and the current is accelerated by two positive feedbacks during this operation. This makes the voltage and current magnitude of the acquired signal significantly high. Therefore, the avalanche transistors can be used to generate high speed and high amplitude pulse.

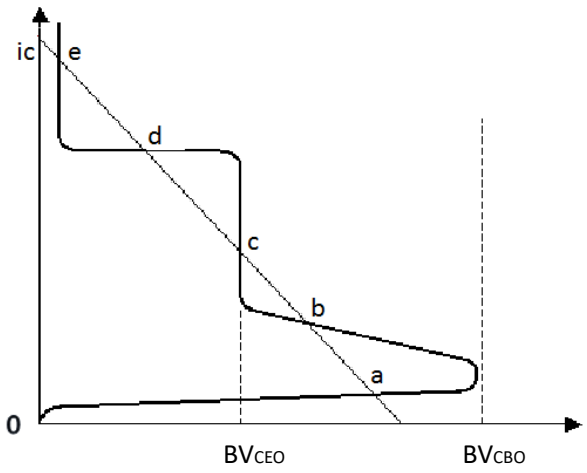

Figure 7-8. Negative resistance characteristics of the avalanche transistor [148].

A ZTX 415 transistor have been chosen as the avalanche transistor in the circuit schematic given in Figure 7-9. This a specially designed transistor for avalanche mode operation with low avalanche breakdown voltage of 100 V. Pulse from the trigger circuit with short rise time triggers the transistor's avalanche mode operation and short fall time brings it back to cut-off region. V_{cc} charges the avalanche capacitor C_2. When charging is complete, the capacitor voltage is approximately equal to V_{cc}. When the input trigger is high, a positive spike pulse generated through C_1 and R_1 differential circuit is applied to the base of the avalanche transistor, Q_1. This pulse spike activates the transistor into unstable avalanche negative resistance area and as a result, avalanche breakdown occurs in Q_1. The transistor stays in low resistance state and the avalanche current increases sharply. As a result, electric charge stored in C_2 discharges through Q_1 to load, R_L and a narrow pulse is achieved across the load. As the avalanche current is high, the narrow pulse has a high peak amplitude. As the avalanche effect finishes, transistor Q_1 returns to cut-off region and source V_{cc} charges C_1 to initiate another avalanche cycle. Turn on time of the transistor, Q_1 determines the discharging extent of capacitor, C_2. So, the function of the trigger circuit is vital as it delivers the narrow width trigger pulse. Moreover, the bias resistor, R_c must be suitable for avalanche effect as power consumption will be high if R_c is too small and output pulse rise time will be high if R_c is too high due to high recovery time. A base resistor, R_b acts as a collector current limiting resistor before avalanche occurs and the value of R_b ranges from 10 to 100 ohm to minimize the effect of collector-to-base transition capacitance.

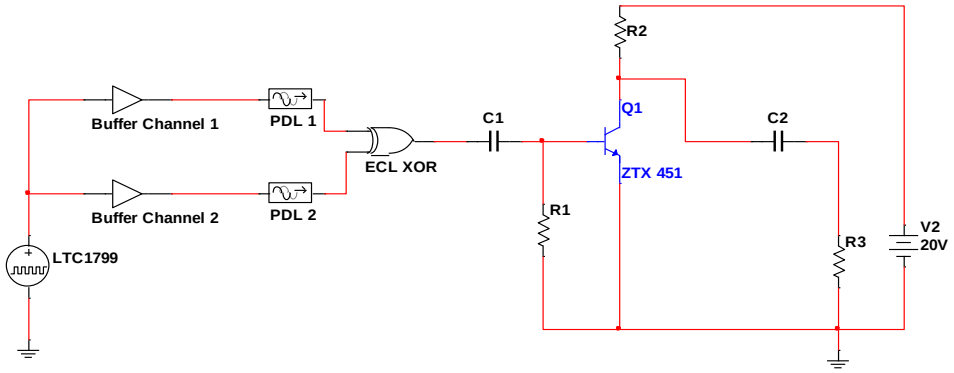

Figure 7-9. Equivalent circuit schematic of the delay line and avalanche transistor based Gaussian pulse generator.

7.2.3 Measurements

Measurements were conducted using TDS2024 2 GS/s four channel digital oscilloscope and Agilent E4405B spectrum analyser. A square wave from the LTC1799 VCO was used as the clock signal. The output voltage of the Gaussian pulse generator was measured choosing the following element values: C_1 = 100 pF, C_2 = 2.2 pF, R_1 = 50 Ω, R_2 = R_3 = 10 kΩ, V_{cc} = 100 V. The input and output Gaussian pulses measured by the wideband oscilloscope are presented in Figure 7-10, which displays the output pulses with varied FWHM width of 750 ps, 1 ns, 2 ns and 10 ns respectively with amplitude of approximately 5 V in the following figures. The normalized PSD obtained from the spectrum analyser of the output is given in Figure 7-11. Normalized PSD of the generated 1 ns width pulse at 1 MHz and 2.5 MHz PRF. which shows that the acquired power level is contained well within -80 dBm to -10 dBm range. Moreover, a comparison of the frequency components between 1 MHz and 2.5 MHz PRF signals with identical pulse width of 1 ns shows that the 2.5 MHz PRF signals contain higher concentration of frequency components. Likewise, the frequency component with highest normalized power are found to be 1 MHz and 2.5 MHz for the respective corresponding PRF's shown by the marker point in Figure 7-11. The PRF of this Gaussian pulse generator could reach up to 33 MHz and the narrowest Gaussian pulse width has been chosen at 750 ps as a design trade-off as the output pulse width could reach as low as 250 ps. However, the pulse amplitude reduces significantly to 400 mV at that level, making the pulse incompatible for GPR application since signal attenuation within the medium will limit the recovery of any reflected signal.

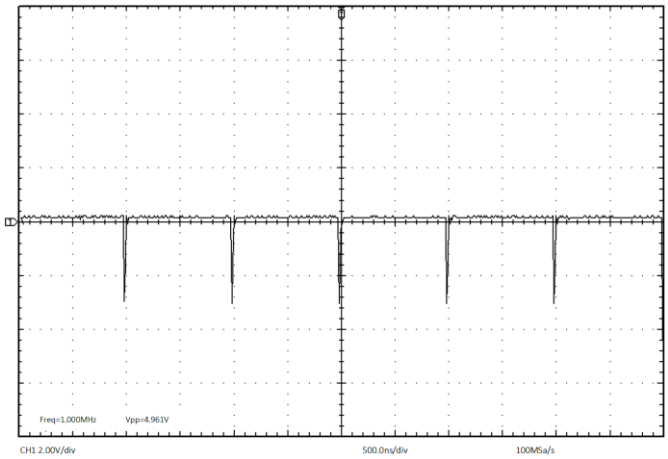

(a)

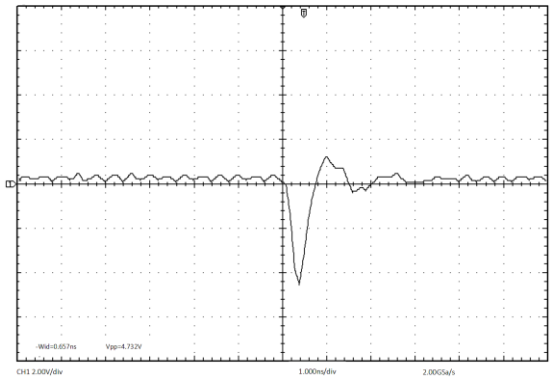

(b)

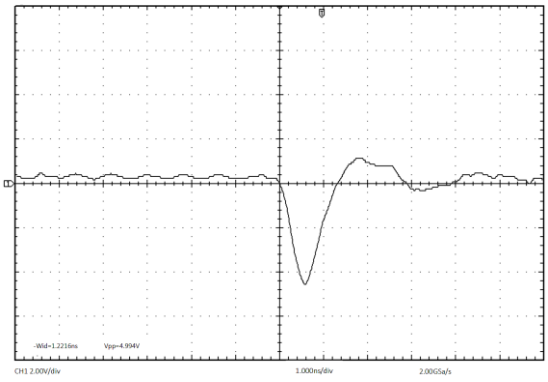

(c)

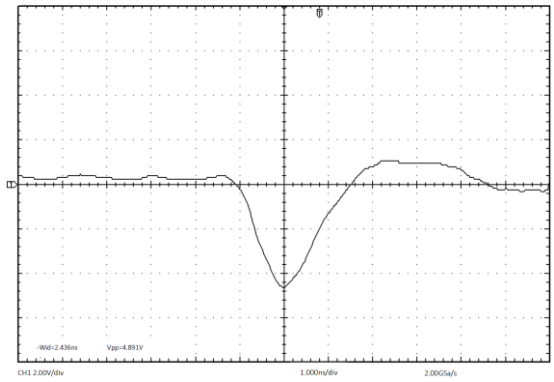

(d)

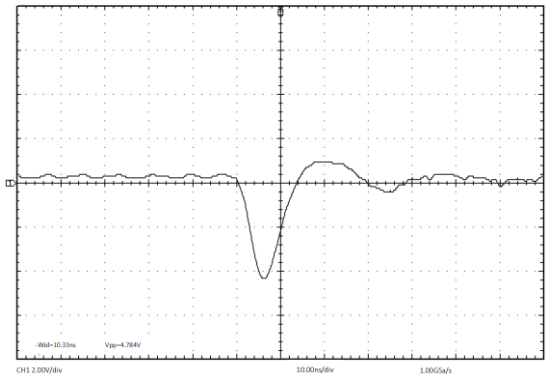

(e)

Figure 7-10. Measured output pulses of the Gaussian pulse generator: (a) Pulse train of 750 ps width at 1 MHz PRF; (b) 750 ps output pulse; (c) 1 ns output pulse; (d) 2 ns output pulse; (e) 10 ns output pulse.

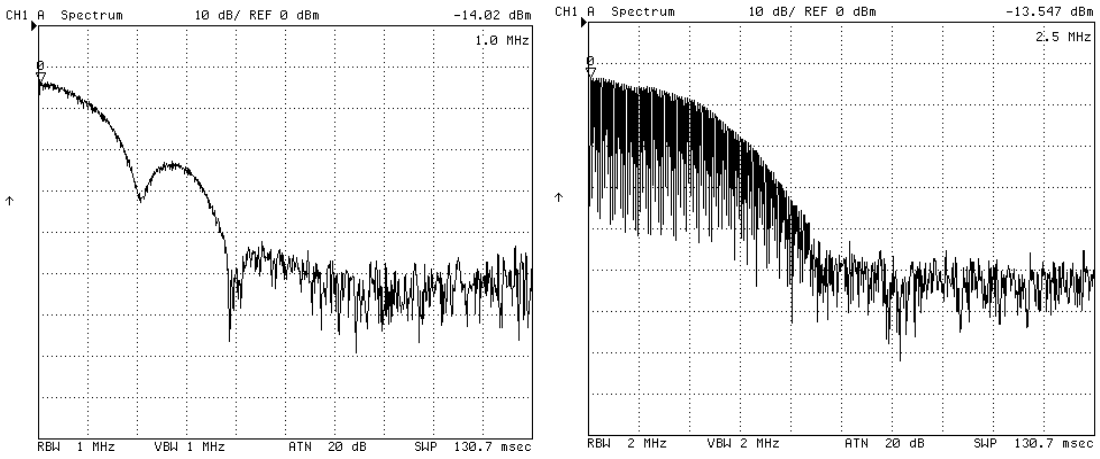

Figure 7-11. Normalized PSD of the generated 1 ns width pulse at 1 MHz and 2.5 MHz PRF.

7.3 Design of the GPR antennas

In impulse GPR applications, short pulses, corresponding to wide bandwidth are used. An accurate ToF measurement is available at the receiving end because of the pulse's high time resolution. In this work, pulses with 10 ns and 5 ns duration are used as transmitting signals, corresponding to 100 MHz and 200 MHz centre frequency operation respectively. Figure 7-12 shows conventional dipole antenna characteristics for the 100 MHz resonance frequency. The material is FR4 with a dielectric constant of 4.4. Total length of the dipole is 1.5 m and width is 15 mm. The reflection coefficient (S11) and voltage standing wave ratio (VSWR) graphs show that the bandwidth of the antenna is 8 MHz for VSWR $\leq$ 2 values.

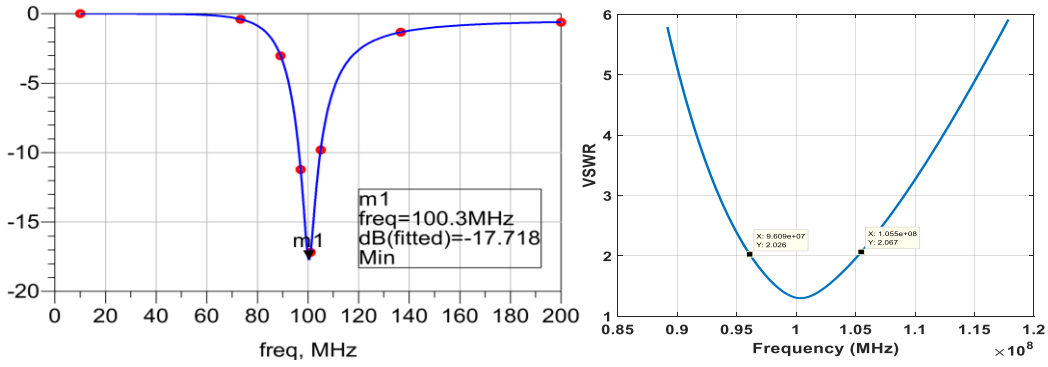

Figure 7-12. Reflection coefficient and VSWR characteristics of dipole antenna.

The configuration of the proposed symmetric dipole antenna with multiple radiating arms is shown in Figure 7-13. The radiating arms consist of 17 μm thick and 15 mm width copper layer. The whole radiating structure is set on FR4 dielectric substrate of 1.6 mm thick.

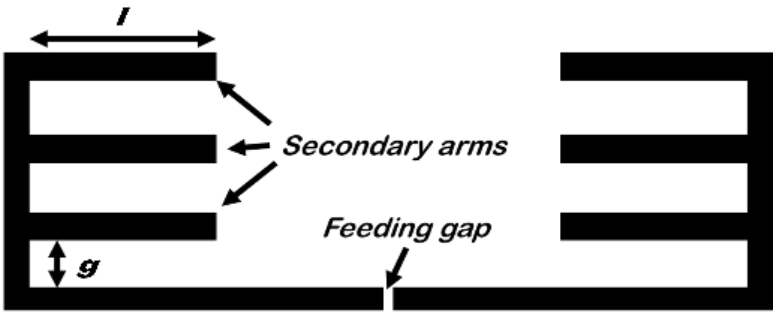

Figure 7-13. Configuration of the proposed miniaturised dipole antenna for 100 MHz centre frequency.

The distance between the primary dipole arm and extra radiating arm is *g* and length of the secondary arm is *l*. In this section, the antenna characteristics are investigated as the parameters are changed to establish an optimum value for both 100 MHz and 200 MHz antenna with maximum dipole length reduction.

7.3.1 Parametric studies

Every aspect of antenna dimension has an effect on the operating bandwidth and centre frequency. To understand the design criteria and their effect on overall antenna performance, antenna design optimization was carried out by MoM based ADS electromagnetic simulator. To establish the optimum antenna design parameters, parametric studies of the distance between the primary dipole arm and extra radiating arms, *g* and length of extra arms, *l* are carried out.

Firstly, the effects of change in antenna additional arm's length, *l* from 300 mm to 10 mm, setting constant g = 20 mm were investigated. The antenna feed gap was kept to 2 mm for FR4 dielectric material. Figure 7-14 shows the reflection characteristics (S11) of the antenna with only three sets of additional arms of various lengths, *l*. It is seen that, long extra radiating arm length of 300 mm provides lowest resonance frequency operation of 137 MHz, but, reflection coefficient, S11 value is below -10 dB and is not acceptable for good performance. As the extra arm length is reduced to 100 mm, the centre frequency increases to 141 MHz, but it provides better S11 value of just above -26 dB. Further reduction of *l* to 10 mm results in antenna operating at 163.5 MHz centre frequency with -21.6 dB of the reflection coefficient. Therefore, reduction in extra arm's length causes the resonance frequency to go higher and reflection coefficient value to reduce. For an acceptable performance of the antenna, length of extra radiating arms is set to the optimum level of 150 mm which represents 132.7 MHz of centre frequency with -16.32 dB of reflection coefficient value.

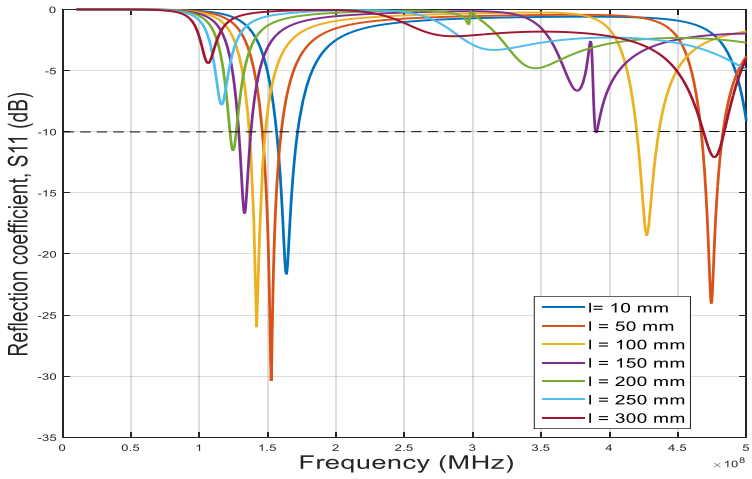

Figure 7-14. Reflection coefficient values at different radiating arm lengths, *l* of 100 MHz dipole.

Likewise, for the 200 MHz dipole, two sets of additional antenna arm's length, *l* was varied from 150 mm to 10 mm, *g* = 20 mm and the reflection coefficient, S11 plot was recorded. Figure 7-15 shows the S11 values for various lengths. It is noticeable that, reduction in additional arm's length results in higher resonance frequency and better S11values. At *l* = 150 mm, the S11 performance is not adequate. The S11 value improves to below -10 dB as the length decreases to 100 mm and reaches its best value of -17.69 dB at 50 mm length with resonant frequency of 199 MHz. At length of 150 mm, the S11 value reaches its lowest point of -26.72 dB however, the resonant frequency shifts to higher region from the desired level. Therefore, the length of additional arms is selected to be 100 mm for an acceptable antenna performance of -17.69 dB S11 at lower resonant frequency of 199 MHz.

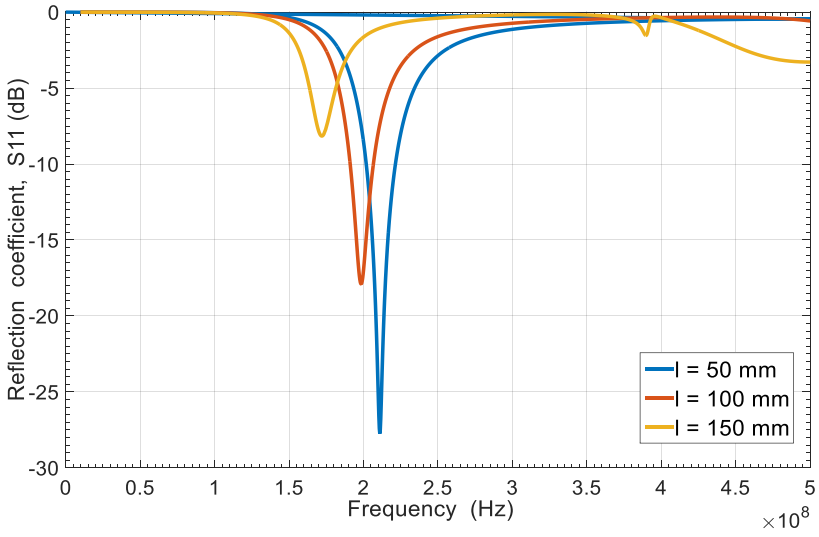

Figure 7-15. Reflection coefficient values of 200 MHz antenna with extra radiating arms of different lengths.

Next, the effect of the gap between the dipole arm and the extra radiating arms, *g* was examined. The additional arm's length was set to 100 mm and *g* values were varied from 5 mm to 150 mm. According to reflection coefficient graph given in Figure 7-16, at *g* value of 10 mm, centre frequency of 133 MHz and S11 value of -16 dB can be achieved. However, another resonance was present at 385 MHz region. As the gap was increased to 50, 100 and 150 mm, centre frequency shifted to lower frequency region of 102, 81 and 68 MHz respectively. The same pattern was observed at higher gap. However, for any *g* value of below 50 mm, the reflection coefficient value increased above the threshold value of -10 dB and therefore, the antenna was not up to the standard required. In order to keep the total area of the antenna to an acceptable minimum level, a value of 50 mm was chosen optimum where a good S11 value of -17 dB was observed at 102 MHz centre frequency.

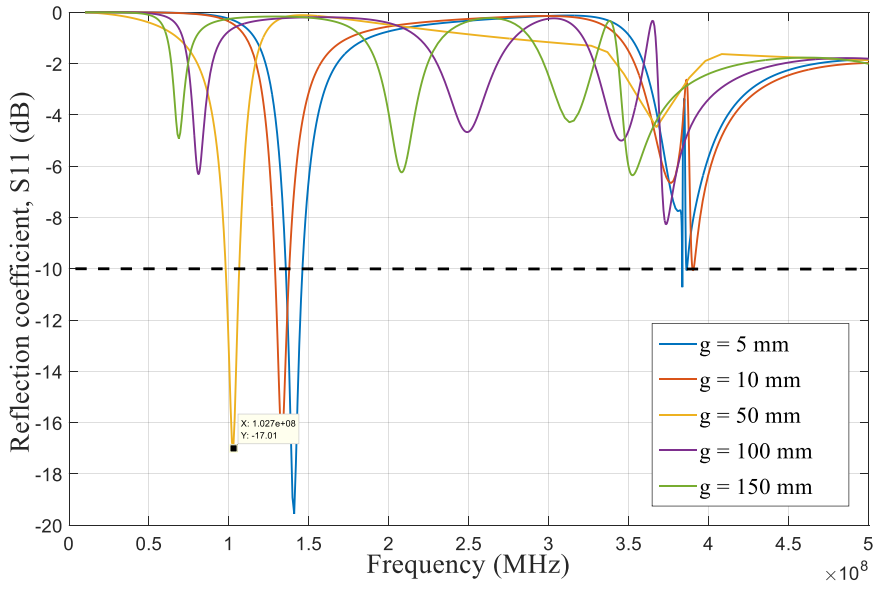

Figure 7-16. Reflection coefficient values for different gaps between the dipole arm and extra radiating arms.

In case of 200 MHz antenna, *g* values were varied from 10 mm to 500 mm while the additional arm's length was kept constant to 100 mm. According to S11 graph given in Figure 7-17, at g = 10 mm, the antenna resonates at 164 MHz with S11 of -11.84 dB. Even though this resulted in a significant amount of dipole length reduction, for impedance and centre frequency matching, g = 20 mm was selected as optimum which resonates at 199 MHz with -17.84 dB of S11 and 9 MHz bandwidth. As the gap was increased to 50 mm gradually, the resonance frequency increased to 215 MHz and was ignored as it fell above the required frequency level.

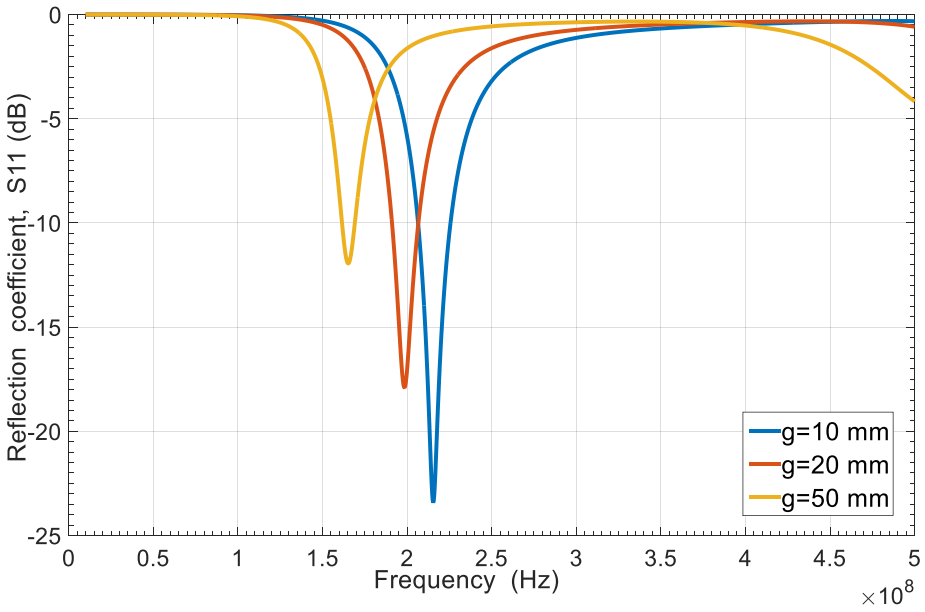

Figure 7-17. S11 values of 200 MHz antenna at different gaps between the dipole arm and extra radiating arm.

Finally, the effect of multiple sets of arm on antenna performance was carried out for g = 50 mm and l = 150 mm for 100 MHz antenna and g = 20 mm and l = 100 mm for 200 MHz antenna subsequently. In case of 100 MHz antenna, only one set of arm delivered -22.38 dB of reflection coefficient at 141.8 MHz and increasing the number of set reduced the resonant frequency to lower band as shown in Figure 7-18. While three sets of arm were implemented, -15.3 dB of reflection coefficient could be achieved at 100.5 MHz centre frequency. However, at four and higher sets of arm could not deliver satisfying S11 value and as a result antenna with three sets of extra radiating arm was selected as optimized design and prototyping.

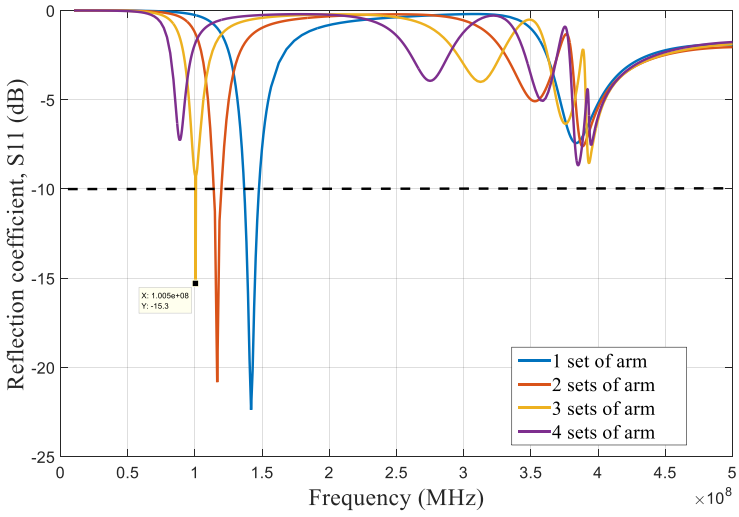

Figure 7-19. Reflection coefficient values for antennas with multiple sets of radiating arm.

Regarding 200 MHZ antenna, without any additional arms, the antenna is a pure dipole that radiates at 300 MHz, while one set of extra radiating arm brings the resonance down to 246 MHz and two sets of arm bring the resonance down to the desired value of 199 MHz with -17.98 dB of reflection coefficient. Three or higher sets of arm cannot provide satisfactory S11 values of greater than -10 dB, therefore, two sets of extra radiating arm have been selected as optimized design and prototyping testing that provides acceptable level of S11. Figure 7-20 represents the effect of multiple sets of radiating arms.

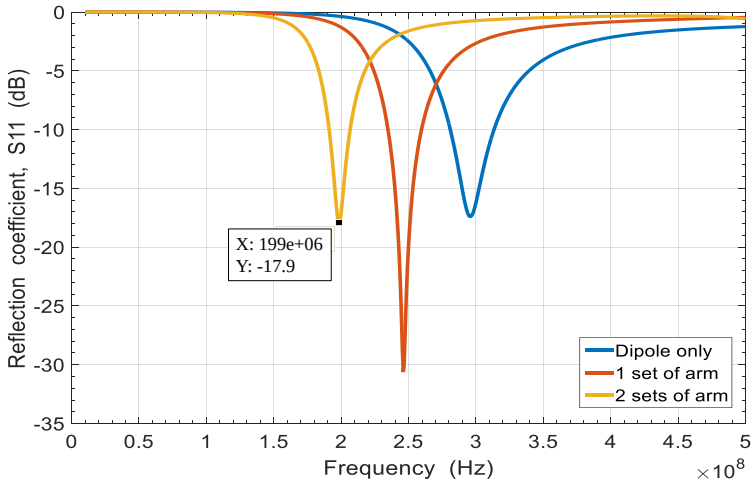

Figure 7-21. S11 values of 200 MHz dipole with multiple set of extra radiating arms.

Figure 7-22 shows the simulated surface current of the proposed 100 MHz antenna with l = 150 mm and g = 50 mm at 100 MHz centre frequency compared to a conventional 100 MHz dipole. It is observed that the extra arms offer significant current distribution along the side bars and extra radiating arms in comparison. This phenomenon explains the reduction in resonance frequency.

Figure 7-22. Distributed surface current along the proposed antenna structure compared to a conventional dipole antenna at 100 MHz centre frequency.

7.3.2 Radiation performance

The radiation pattern in the E-plane and H-plane of the 100 MHz antenna in Figure 7-23 demonstrates that the proposed antenna has a typical dipole like characteristics at the resonant frequency band. The patterns are nearly omnidirectional with an efficiency value of 71 %. In this condition, the directivity gain is 2.06 dBi compared to 2.15 dBi

for more conventional dipoles. These values are considered as good in the literature. The 200 MHz antenna delivers approximately the same values.

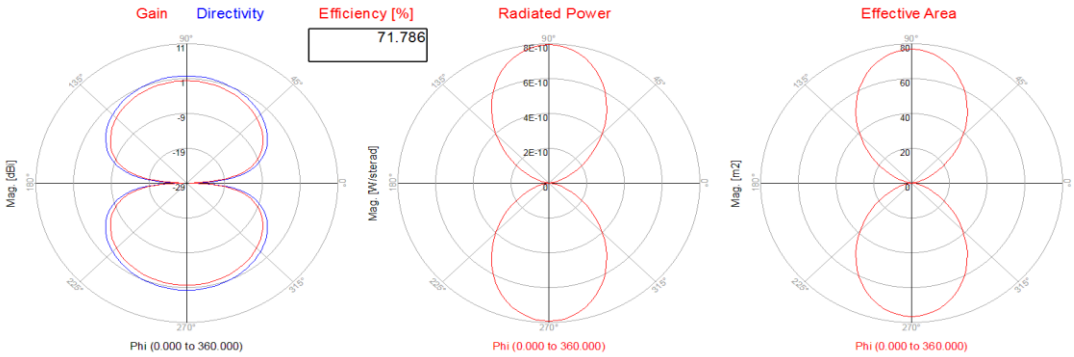

Figure 7-24. Radiation pattern of the proposed antenna at 100 MHz centre frequency.

7.3.3 Experimental Validation

To validate the simulation results and antenna performance, two prototype antennas with extra radiating arms were fabricated using a 1.6 mm thick FR4 dielectric substrate ($\varepsilon_r = 4.4, \tan d = 0.02$). The antenna arms were printed on the substrate using 17 µm thick copper strips. The dimensions of the antennas were 66.5×22×0.2 cm for 100 MHz and 40×20×0.2 cm for 200 MHz respectively. Figure 7-25 shows the fabricated prototype antennas which are fed by a 50 Ω BNC connector.

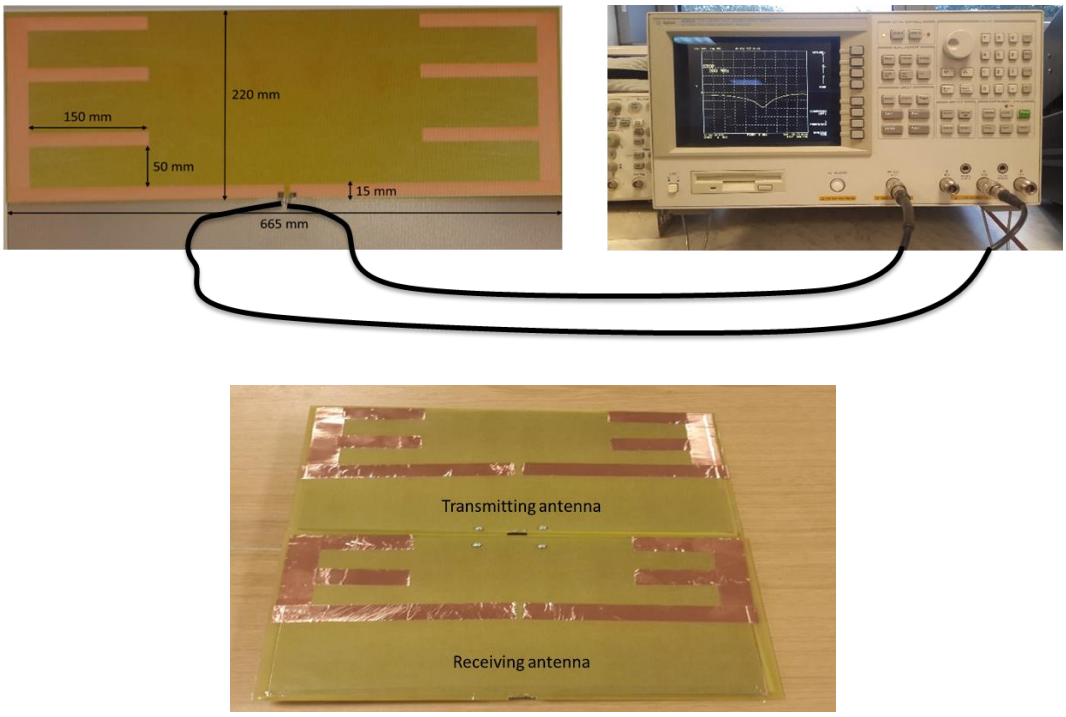

Figure 7-26.Prototype 100 MHz antenna and antenna testing using Agilent 4395A network analyser.

To measure the antenna performance, an Agilent 4395A network analyser was used. This particular analyser can provide 10 Hz – 500 MHz sweep frequency capability. Figure 7-27 shows the reflection coefficient graph of the antenna under test at 75 – 125 MHz frequency sweep with centre frequency being at 104 MHz. The test was carried out for the full 500 MHz frequency sweep and the raw data were saved as comma separated values (csv) format and regenerated using Matlab which is shown in figure 16 along with the radiation pattern graph.

Experiments show that the proposed antenna resonates at centre frequency of 104 MHz compared to 101 MHz obtained by ADS simulation. The measured reflection coefficient value is -15.88 dB, which is fairly in line with the value of -15.2 dB obtained during simulation. Measured radiation pattern graph shows an expected omnidirectional radiation at 1.52 dBi of directional gain with 68 % efficiency compared to 2.06 dBi resulted in simulation. Also, judging from the Figure 7-28, the fabricated antenna delivers a bandwidth of 8 MHz where VSWR $\leq$ 2 compared to 9.5 MHz bandwidth obtained from simulation. This is a reduction of only 2 MHz compared to a conventional dipole antenna.

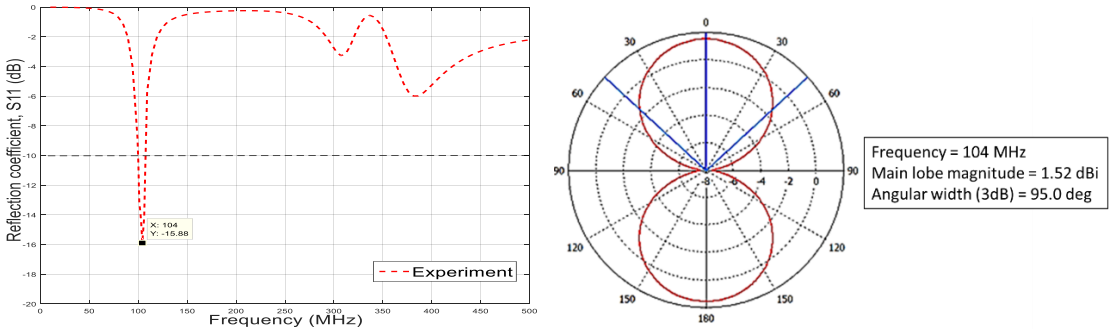

Figure 7-27. Measured S11 of the proposed antenna along with the radiation pattern.

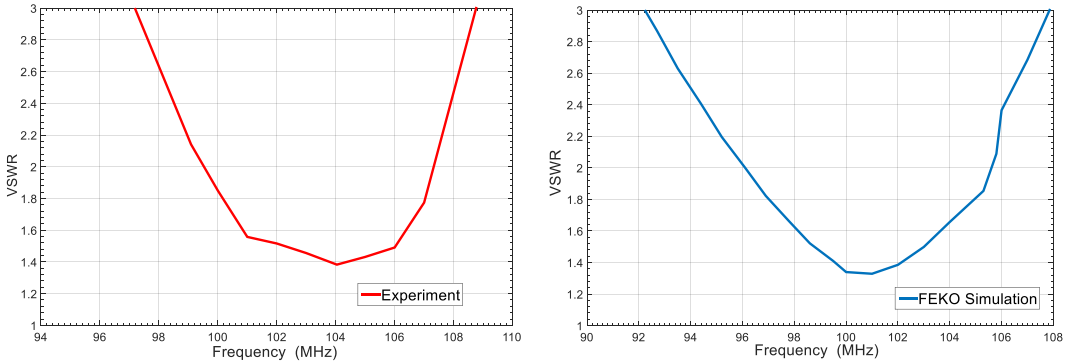

Figure 7-28. VSWR characteristic comparison of measured and simulated values.

In regards to 200 MHz antenna, experiment result shows the antenna resonates at 206.1 MHz centre frequency with -14.8 dB of S11. This is a +6 MHz of variation

compared to simulations, however, the experiment results are acceptable and closely matched with simulations. The measured antenna has 14 MHz -10dB bandwidth and 1.9 dBi of directivity gain. The reflection coefficient graph is given in Figure 7-29.

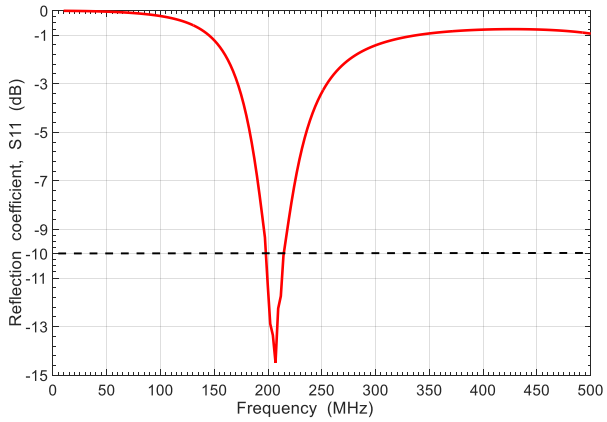

Figure 7-30. Measured S11 from the Agilent 4395A network analyser for 200 MHz modified antenna.

7.4 Design of a wall climbing robotic GPR system

The fabricated 200 MHz transmitting and receiving antenna set was integrated with the mobile climbing robot. The robot was equipped with two infra-red distance measurement sensors at the front end for vertical wall detection and two servo motors were used to fold and unfold the GPR antennas for the robot to execute floor-to-wall and wall-to-floor transition procedure. As a vertical wall is detected by the infra-red sensors while the robot is operating on the floor, the servo mechanism folds the antenna set backward for the front set of robot wheels to make contact with the wall. As the transition is completed and the robot is stabilized on the vertical wall, the servo motor unfolds the antennas back to scanning position. The same procedure is performed in sequence during wall-to-floor transition. The prototype robotic GPR system and its floor-to-wall transition procedure is shown in Figure 7-31.

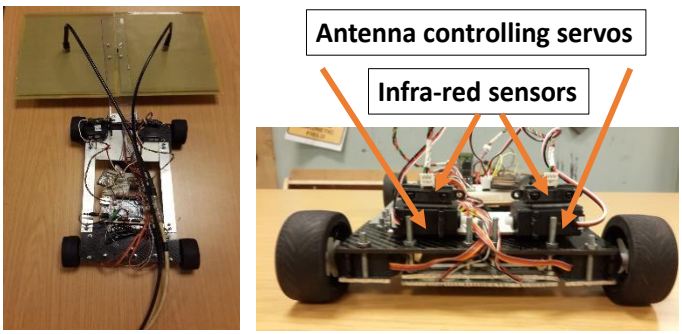

(a)

(b)

Figure 7-31. (a)Top and front view (without the antenna) of the prototype robotic GPR system; (b) Floor-to-wall transition procedure.

7.4.1 Experiments

Experiments were conducted to detect and localize buried objects. The application field of this proposed robotic GPR system is concrete structures inspection. Therefore, to emulate the concrete inspection scenario, a test rig described in chapter 4 using wooden frame was used. Concrete and wood have same dielectric constant of 1 and magnetic permeability of 1. So, a wooden plate can be used as a concrete cover. A 30 cm long and 1.5 mm thick aluminium plate, an aluminium block of 15×8×4 cm dimension and a rebar of 12 mm diameter have been chosen as target buried objects to be detected. The GPR transmitter consists of the developed Gaussian pulse generator that generates a train of 5 ns FWHM Gaussian pulse at -5 V peak-to-peak amplitude at 1 MHz repetition frequency. The GPR receiver consists of a 1 GSa/s Agilent DSO3102A sampling oscilloscope which visualizes the reflected signal captured by the receiving antenna and the Agilent 4395A network analyser for S11 measurement. Figure 7-32 presents the measurement setup and the target objects for the experiments. Each object has been placed under the wooden plate in turns and the GPR scanning is performed separately for each object.

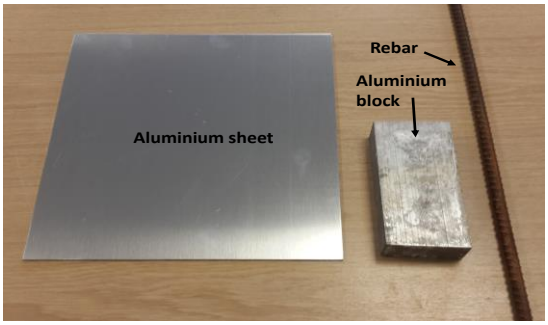

(a)

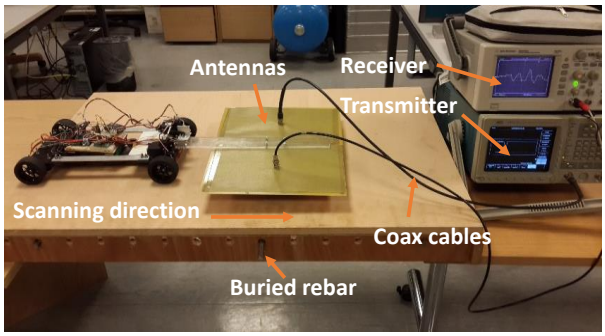

(b)

Figure 7-32. (a) GPR measurement setup using the pulse generator and oscilloscope; (b) Target buried objects.

7.4.2 Time domain analysis

First, the reflected signals were captured for the 30 mm long aluminium sheet located at 40 mm depth. The robot was stopped and the reflected signal was captured at 5 cm step resolution. At the robot's initial position, the initial transmitting pulse and the reflected pulse from the floor can be seen in profile 1 of Figure 7-33. As the robot travels towards the object, another reflected pulse appear in between the initial pulse and floor reflection. This small reflected pulse is from the buried aluminium sheet. The small reflected pulse gains in amplitude as the robot moves more towards the sheet and achieves its maximum amplitude level as seen in profile 4, where the GPR receiving antenna is located right above the sheet. The amplitude of the reflection starts to reduce as the robot travels away from the buried sheet.

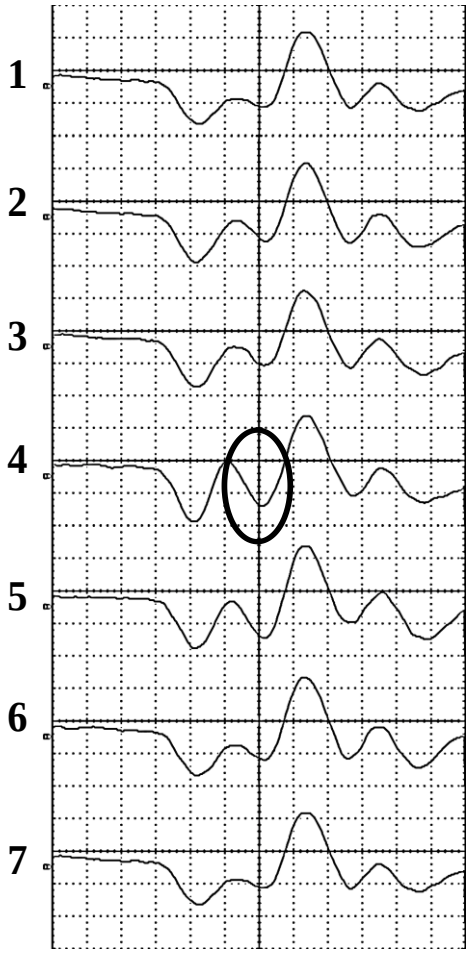

Figure 7-33. Received signal profiles during aluminium sheet detection.

Likewise, to detect the aluminium block, a stepping resolution of 3 cm steps is chosen. The reflection profiles at different antenna positions are found to be the same as previous setup. Profile 3 of Figure 7-34 appears to be the position where the antenna is located right on top of the block.

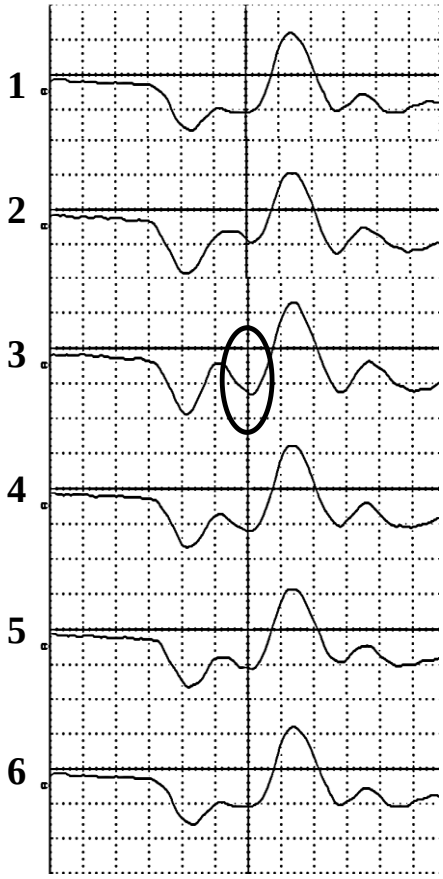

Figure 7-34. Received signal profiles during aluminium block detection.

Same pattern of results was found during the detection of a 12 mm diameter rebar located at 40 mm depth. In this case, profile 3 of Figure 7-35 shows the position of the antenna aligned right on top of the rebar. It shows a low amplitude signal because of the smaller size of the target, however, the peak of the reflection is clearly visible. Moreover, the time difference between the peak of the initial pulse and the reflected pulse is 3.2 ns. By using this two-way travel time, the measured distance is calculated to be 0.51 m. There is an error of 0.11 m between the actual and measured values. A higher resolution GPR with a sharper pulse width can rectify this error. A low frequency GPR has a deeper penetration depth of up to 7 m according to the literature. However, a low pulse amplitude of 5 V has been selected as the transmitting pulse in this work which reduces the penetration depth to about 50 mm and make it suitable for concrete structure environment where the rebars are buried at a maximum depth of 60 mm depending on the structure category.

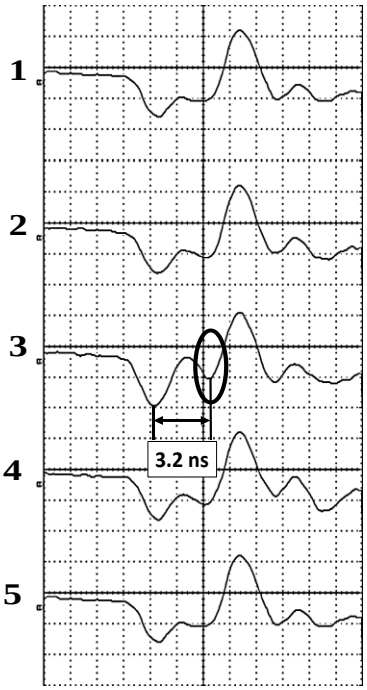

Figure 7-35. Received signal profiles during steel rebar detection.

7.5 Chapter summary

In this chapter, the design and testing of a concrete wall climbing robot for performing GPR surveys in vertical reinforced concrete structure have been presented. A low frequency 200 MHz prototype GPR system has been designed using miniaturized antennas. The rationale of choosing a low frequency system is to keep the development cost down by using off the shelve electronic components. The technique of implementing multiple sets of additional radiating arms has reduced the dipole antenna length by 55% and 44% respectively for 100 MHz and 200 MHz antenna compared to conventional dipoles. This feature improves the portability of the system and provide a methodology for further miniaturization of high frequency system in the future. The assembled prototype robot exhibits good operational efficiency. Experiments demonstrate the capability of the developed GPR to detect and localize an aluminium sheet and a block, a rebar at up to 40 mm depth. Even though there is an experimental error of +0.11 m, the implementation of narrower pulse of 1 ns or lower could improve the result and this is a target for future work. The utilization of low amplitude transmitting pulses ensures the low penetrating capability which is suitable for concrete environment. The aim of this work is to prove the design concept that the deigned robot can be deployed to collect the radar data, allowing operators to safely perform grid or detailed surveys of potentially hazardous locations and allowing them to process data offline from a safe location.

Chapter 8. Conclusion

NDT plays a crucial role in assuring the safety and reliability of safety critical structures. It prevents structural failure and reduces maintenance cost. Automated and robotic NDT can add value by increasing inspection efficiency. This research has achieved significant advancement towards enabling wall climbing robotic NDT of reinforced concrete structures by developing a robust and reliable magnetic adhesion system along with a low cost GPR system.

A literature review was carried out to understand the operation environment and the key design requirements of climbing robots. Robot design review based on locomotion and adhesion principles has revealed the compatibility of arms, wheels or sliding frame locomotion based robots in the civil engineering scenario. Three distinct adhesion principles – magnetic, suction and chemical were evaluated for suitability. This review established limitations of corresponding locomotion and adhesion principles and identified the research gaps in current climbing robot technology. Based on the comparative study, wheel based locomotion has been chosen because of its continuous and smooth motion. Moreover, wheel locomotion can offer multiple DoF at less system complexity. In terms of adhesion, permanent magnet was chosen to develop a novel adhesion mechanism that instead of focusing the magnetic energy on the surface, magnetic coupling is achieved with buried rebars that are located at some distance from the concrete surface. Permanent magnet can deliver reliable and high payload capacity at the cost of zero energy consumption.

Having set the design requirements and the operating conditions, the next research objective was to design the novel adhesion mechanism that can penetrate the concrete surface up to a certain level to establish the magnetic coupling with the rebars. Steel rebars are buried within the concrete surface to provide additional enforcement and durability to the concrete structure. The depth at which the bars are buried depends on the structure category defined in the Eurocode 2 and BS850. According to those regulations, the concrete cover can vary from 25 – 60 mm. In order to design an adhesion module that can penetrate up to 60 mm of concrete and provide sufficient attraction force, research work was divided into simulation and experimental form. Simulation works were initiated by investigating the effect of key design parameters such as the distance between two magnets, magnet dimension, yoke thickness on the adhesion force using the Comsol FEA suite. Investigation of the distance between multiple magnets showed that an optimum distance is vital for a balanced distribution of magnetic flux. Two 50 mm and 100 mm long magnets achieve highest adhesion mechanism of 64.93 N and 151.81 N respectively. The optimum corresponding gaps were found to be 50 mm and 100 mm. This result established that the in-between distance should be equal to the magnet length. Moreover, the implementation of a yoke significantly increases the adhesion force. The optimum yoke thickness was found to be 25 mm that delivers maximum attraction force of 64 N at 35 mm concrete cover. Any increase in yoke thickness did not increase the force significantly, but reduced the force-to-weight ratio instead. The effect of yoke material found to be neutral where increase in material magnetic permeability from 5000 to 200,000 resulted in the adhesion force increase of only 2 N. Furthermore, optimization of the yoke design and magnetic circuit coupling showed that three magnets arranged on a yoke with alternating NSN polarity provides the best adhesion force profile over a range of concrete cover from 10 mm – 40 mm compared to other magnet arrangement configurations. The NSN configuration can generate 64 N of force at a concrete cover of 45 mm. Additionally, if the concrete wall is reinforced with the meshing of rebars, then implementation of multiple yokes with minimum distance between them can ensure a higher adhesion force. During simulation, two yoke modules with an intermitting gap of 5 mm generated 50.6 N higher adhesion force compared to a single yoke unit while a rebar mesh of 50×50 mm is present.

In order to carry out the experimental analysis and design validation, a test rig was used. The rig was built using a wooden plate that can imitate the material properties of concrete with interchangeable rebar grid meshing. The prototype adhesion mechanism

consisting of three N42 grade neodymium magnets mounted on an iron yoke was attached beneath a mobile robot chassis. The performance of the climbing robot was assessed on both ferrous wall and the concrete wall. Experiments on a 10 mm thick ship hull segment showed that the prototype robot can exert an adhesion force of maximum 213.33 N with an additional 1.6 kg of on-board sensor system. As the climbing surface was highly uniform, the variations in adhesion force at different points of the hull segment was marginal. Regarding to the concrete wall scenario, highest adhesion force of 178.5 N was achieved using one yoke unit of NSN configuration at 50×50 mm rebar grid and 35 mm of concrete cover. Furthermore, assessment of the robot's rotational capability demonstrated that the adhesion force falls to a minimum of 118 N at the robot position of 30^0, 60^0, 120^0, 240^0, 300^0, and 330^0 angles. Fine rebar meshing can deliver smooth manoeuvring of the robot due to the influence of closely located rebars. Successful field testing witnessed the robot climbing a residential building column reinforced with rebars located at 35 mm depth. The maximum adhesion force was measured at 127.53 N with an average of 110.16 N. Based on the measured adhesion force, the maximum payload capacity of the robot is determined to be 7 kg. Comparison of the proposed adhesion mechanism with other notable systems for concrete surface climbing found in the literature is given in Table 8-1.

Table 8-1. Comparison of the proposed adhesion system of this research with other notable systems found in the literature.

	Ref [149]	**Ref** [150]	**This work**
Robot weight (kg)	1.2	0.9	2.23
Maximum applicable adhesion force (N)	10	2.94	121.26
Force-to-weight ratio	0.85	0.33	5.54
Adhesion mechanism	Electrostatic	Vortex	Magnetic
Locomotion	Wheel	Wheel	Wheel
Application medium	Any	Concrete wall	Concrete wall

An extensive review of GPR technology and its operating principles were performed. Time-domain impulse radar was selected as the most suitable candidate due to its high resolution feature and simple building blocks. The objective of this stage was to build a prototype GPR using low cost, off the shelve electronics. Firstly, a numerical framework was presented to model a GPR's working principle using Maxwell's electromagnetic equations. A FDTD based model was proposed that can model an inspection scenario with multiple layers of different materials. The model of a concrete wall with a buried rebar was modelled using the proposed framework and the detection

of the rebar at 30 cm depth was carried out with 100% accuracy. This framework can help researchers to model environment with various geometrics and determine the GPR signal responses.

Finally, the thesis discussed the development process of a prototype GPR hardware system mountable on the mobile climbing robot. The first unique feature of this GPR hardware is the design of an enhanced tuneable pulse generator. The application of ECL based high frequency PDL and XOR chips made the Gaussian pulse generator capable of producing 750 ps to 10 ns width pulse train with 5 V of amplitude. This narrow pulse width enabled the wide pulse bandwidth range and high time resolution. The prototype circuit high concentration of frequency components in normalized PSD graph. This tuning capability made this pulse generator suitable for wideband GPR applications where adaptation to different environmental conditions is crucial. Moreover, the implementation of off the shelve components during the development process meant a low cost solution to high resolution pulse generator. A comparative study of this proposed pulse generator with other known works is given in Table 8-2.

Table 8-2. Wideband Gaussian pulse generator circuit output comparison.

	This work	**Ref.** [151]	**Ref.** [152]	**Ref.** [153]	**Ref.** [154]
Pulse width	750 ps shortest	240 ps	800 ps	700 ps	3.2 ns
Adjustable	Yes	Yes	No	No	No
Technology	ECL	CMOS	CMOS	Discrete components	SRD
Ringing	Low	High	High	Moderate	Small

Secondly, the novel technique of additional radiating arms added with a conventional dipole allowed to design a miniaturized low frequency dipole antenna. Investigation of a 100 MHz dipole revealed that adding three extra symmetric radiating arms can reduce the total length of the dipole by 55% compared to a conventional one. The operation bandwidth was found to be 8 MHz at 1.52 dBi gain, offset of only 1.5 MHz from the simulation result. Design of a 200 MHz antenna recoded a reduction of 44% compared to a 200 MHz dipole with higher bandwidth of 14 MHz. Two 200 MHz antennas, one acting as a Tx and another as Rx antenna were mounted on the climbing robot for the purpose of detecting buried objects. Table 8-3 presents a comparative study of the proposed antenna with other notable designs found in the literature.

Table 8-3. Comparison of the fabricated antenna with other models.

Antenna type	Centre frequency (MHz)	Bandwidth (MHz)	Antenna size (cm)	Efficiency	Remark
Dipole	100	10	150×1	-	-
This work	100	8	66.5×22	68%	55 % reduction in length
[155]	1500	2700	32×240	68%	31% reduction in length
[156]	500	600	23×10	75%	46 % reduction in length

Time domain analysis obtained from the robotic GPR system showed successful detection of three buried objects. To carry out the experiments, an aluminium plate, an aluminium block and a steel rebar were placed beneath the wooden frame of a test rig and the reflection data samples were recorded at regular intervals. Time domain profile depicted clear reflected signals from objects buried at 40 mm depth. Further analysis using a buried steel rebar showed that the depth of the rebar could be calculated by measuring the two-way travel time. Given the limited bandwidth of the antennas used, the experimental error was at very nominal level of +0.11 m. However, the operating principles and the design concept proved the feasibility of the developing a low cost, high resolution robotic GPR system with low output error.

8.1 Future work

Several unique design parameters ranging from robot design to antenna fabrication have been proposed and successfully evaluated in this research. Nonetheless, there are many possible areas of future work in this research. Some are related to improving the existing work and some are related to additional research building upon the existing model for enhanced reliability. Here some of the recommendations with high potential impact are discussed.

- Development of high payload prototype based on the experimental results obtained. The number of magnets and their configuration can lead to higher adhesion force. Though 12 mm diameter rebar and N42 grade magnets were used for experimentations, rebars used are much thicker (55 mm) in its target application such as nuclear power plant and bridge column. Therefore, the adhesion force will be much higher in those conditions. Moreover, nearby

rebars in a rebar mesh will also increase the adhesion force. To turn the robot into a practical application, a higher grade (N52) of neodymium magnets could be used that will increase adhesion, while keeping the force to weight ratio as same as N42 grade magnets.

- Further investigation of yoke design could be carried out to reduce the overall flux leakage of the system. This could give way to development of flux concentration technique in which more buried reber could be included in the attraction area thus increasing the adhesion force.
- A permanent magnet and electromagnet based hybrid adhesion module could be investigated and a closed loop control system could be devised. If the buried rebar depth is small enough to generate sufficient adhesion force only by utilizing permanent magnets. Should the concrete cover be big so that the permanent magnets alone cannot generate nominal adhesion force, electromagnetic system will be activated to generate that additional adhesion force. The closed loop system will control the current flow and thus the intensity of the electromagnet.
- As the prototype pulse generator circuit built using adapter on a vero-board, the stray capacitance resulting from that add marginal ringing effect on the pulse output. Therefore, an industry standard printed circuit board of the pulse generator could be fabricated to accommodate high frequency surface mount chips with reduced stray capacitance.
- Implement the antenna loading mechanism in order to increase the antenna bandwidth. A higher system bandwidth ensures higher operating range without using different antenna size. Moreover, introducing a filtering technique for noise reduction and better signal processing ability will drastically improve the system accuracy.

References

[1] T. Sattar, E. Hernando and S. Jianzhong, "Amphibious NDT Robots," *International Journal of Advanced Robotics Systems,* vol. 6, p. 24, 2007.

[2] D. Fanella, "Design of Low-Rise Reinforced Concrete Buildings Based on 2009 IBC," ASCE/SEI 7–05, ACI 318–08, International Code Council, Washington, 2009.

[3] S. Kosmatka, B. Kerkhoff and W. Panarese, "Design and Control of Concrete Mixtures," Portland Cement Association, Skokie, 2008.

[4] F. Bolt and D. Manning, "Detecting Delamination in Concrete Bridge Decks," Concrete Innovation, Illinois, 1980.

[5] Z. Guan, S. Chen, H. Zhu and H. Zhang, "A Miniature Biped Wall-Climbing Robot for Inspection of Magnetic Metal Surfaces," in *IEEE International Conference on Robotics and Biomimetics*, Guangzhou, 2012.

[6] M. Howlader and T. Sattar, "Development of Magnetic Adhesion Based Climbing Robot for Non-Destructive Testing," in *7th Computer Science and Electronic Engineering Conference*, Essex, 2015.

[7] GSSI, Case and Study, "A Tall Order: Scanning a 300-feet Chimney," Geophysical Survey Systems, Inc., Salem, 2009.

[8] D. Longo and G. Muscato, "Adhesion Techniques For Climbing Robots: State Of The Art And Experimental Considerations," in *International Conference on Climbing and Walking Robots (CLAWAR),* Singapore, 2008.

[9] B. Zhiqiang, G. Yisheng, C. Shizhong, Z. Haifei and Z. Hong, "A miniature Biped Wall-Climbing Robot for Inspection of Magnetic Metal Surfaces," in *IEEE International Conference on Robotics and Biomimetics*, Guangzhou, 2012.

[10] R. Bogue, "Robots in The Nuclear Industry: A Review of Technologies and Applications," *Industrial Robot: An Ineternational Journal,* vol. 38, no. 2, pp. 113-118, 2011.

[11] R. David, C. Elisabeth, D. Robert, G. Michael and O. Jacqueline, "Risk of Cancer from Occupational Exposure to Ionising Radiation: Retrospective Cohort Study of Workers in France, the United Kingdom, and the United States (INWORKS)," *British Medical Journal,* vol. 351, p. 5359, 2015.

[12] G. Bayten, "Computerized Ultrasonic Inspection of LPD Vessel Construction Welds," Integrity NDT, Ankara, 2012.

[13] D. McCann and M. Forde, "Review of NDT Methods in the Assessment of Concrete And Masonry Structures," *International Journal of NDT and E,* vol. 34, pp. 71-84, 2001.

[14] C. Colla, P. Das, D. McCann and M. Forde, "Sonic Electromagnetic And Impulse Radar Investigation Of Stone Masonry Bridges," *International Journal of NDT and E,* vol. 30, no. 4, pp. 249-254, 1997.

[15] M. Sansalone and W. Street, Impact–Echo: Non-destructive Evaluation Of Concrete and Masonry, New York: Bullbrier Press, 1997.

[16] J. Martin, M. Hardy, A. Usmani and M. Forde, "Accuracy of NDE In Bridge Assessment," *Journal of Engineering Structures,* vol. 20, no. 11, pp. 979-84, 1998.

[17] D. Anderson and R. Seals, "Pulse Velocity As A Predictor of 28 and 90 Day Strength," *Journal of ACI Structural Journal,* vol. 78, no. 2, pp. 116-122, 1981.

[18] B. Drinkwater and P. Wilcox, “Ultrasonic Arrays For Non-destructive Evaluation: A Review,” *International Journal of NDT and E,* vol. 39, no. 7, pp. 525-541, 2006.

[19] P. Servais and N. Gerlach, “Development Of A NDT Method Using Thermography For Composite Material Inspection On Aircraft Using Military Thermal Imager,” in *International Workshop on Advances in Signal Processing For Non-destructive Evaluation of Materials*, Quebec, 2005.

[20] C. Stanley and R. Balendran, “Developments In Assessing The Structural Integrity Of Applied Surfaces To Concrete Buildings And Structures Using Infra-red Thermography,” in *International Conference On Structural Faults AndRepair,* London, 1995.

[21] A. Mishin, “Portable Linear Electron Accelerators For Electron Beam Curing of Composites, Non-destructive Testing and Other Applications,” in *International Conference on Structural Faults and Repair*, Edinburgh, 1997.

[22] J. Alldred, “Improvements To The Orthogonal Method For Determining Reinforcing Bar Diameter Usin A Cover Meter,” in *International Conference on Structural Faults and Repair*, London, 1995.

[23] E. Pasolli, F. Melgani and M. Donelli, “Automatic Analysis of GPR Images: A Pattern-Recognition Approach,” *IEEE Transaction of Geoscience and Remote Sensing,* vol. 47, no. 7, pp. 2206-2217, 2009.

[24] J. Francke, “Applications of GPR in Mineral Resource Evaluations,” in *International Ground Penetrating Radar Conference*, Lecce, 2010.

[25] G. Grazzini, M. Pieraccini, F. Parrini, A. Spinetti, G. Macaluso, D. Dei and C. Atzeni, “An Ultra-Wideband High-Dynamic Range GPR for Detecting Buried People After Collapse of Building,” in *International Ground Penetrating Radar Conference*, Lecce, 2010.

[26] E. Trautmann, L. Ray and J. Lever, “Development of an Autonomous Robot for Ground Penetrating Radar Surveys of Polar Ice,” in *IEEE/RSJ International Conference on Intelligent Robots and Systems,* St. Louis, 2009.

[27] E. Utsi, “The Shrine of Edward the Confessor: A Study in Multi-Frequency GPR Investigation,” in *International Ground Penetrating Radar Conference*, Lecce, 2010.

[28] J. Irving and R. Knight, “Numerical modeling of ground-penetrating radar in 2-D using MATLAB,” *Journal of Computers & Geosicences,* vol. 33, pp. 1247-1258, 2006.

[29] K. Takahashi, J. Igel, H. Preetz and S. Kuroda, “Basics and Application of Ground-Penetrating Radar as a Tool for Monitoring Irrigation Process,” in *Problems, Perspectives and Challenges of Agricultural Water Management*, InTech, 2012, p. 160.

[30] A. Alongi, T. Cantor, C. Kneeter and A. Alongi, Concrete Evaluation By Radar Theoretical Analysis, ISSN: 0361-1981: Transportation Research Board, 1982.

[31] D. Smith and J. Harry, “Ground Penetrating Radar: Antenna Frequencies and Maximum Probable Depths of Penetration in Quaternary Sediments,” *Journal of Applied Geophysics,* vol. 33, pp. 93-100, 1995.

[32] K. Berns, C. Hillenbrand and T. Luksch, “Climbing Robots for Commercial applications: A Survey,” in *International Conference on Climbing And Walking Robots and the Support Technologies for Mobile Machines (CLAWAR)*, Catania, 2003.

[33] M. Armada, P. Santos, M. Jimenez and M. Prieto, “Application of Clawar Machines,” *International Journal of Robotics Research*, vol. 22, no. 3, pp. 251-259, 2003.

[34] F. Manuel and J. Tenreiro, A Survey of Technologies and Applications for Climbing Robots Locomotion and Adhesion, Miripour: Intech, 2010.

[35] M. Howlader and T. Sattar, “Novel Adhesion Mechanism and Design Parameters for Concrete Wall-Climbing Robot,” in *SAI Intelligent Systems Conference*, London, 2015.

[36] E. Ginzel, Weld Inspection of Ultrasonic Inspection - Training for Nondstuctive Testing, ISBN 1895518148: NDTnet, 1998.

[37] C. Balaguer, A. Gimenez and A. Jardon, "Climbing Robot's Mobility for Inspection and Maintenance of 3D Complex Environments," *International Journal of Autonomous Robots,* vol. 18, no. 2, pp. 157-169, 2005.

[38] T. Wei, R. Quinn and R. Ritzmann, "A CLAWAR That Benefits From Abstracted Cockroach Locomotion Principles," in *International Conference on Climbing and Walking Robots and Support Technologies for Mobile Machines (CLAWAR)*, Berlin, 2005.

[39] M. Minor, Dulimarta, H., G. Danghi, R. Mukherjee, R. Tummala and D. Aslam, "Design, Implementation, and Evaluation of an Under-actuated Miniature Biped Climbing Robot," in *International Conference on Intelligent Robots and Systems*, Takamatsu, 2000.

[40] M. Armada, P. De Santos, E. Garcia, M. Prieto and S. Nabulsi, "Design of Mobile Robots," in *CLAWAR: Introductory Mobile Robotics Workshop*, London, 2005.

[41] J. Resino, A. Jardon, A. Gimenez and C. Balaguer, "Analysis of The Direct and Inverse Kinematics of Roma II Robot," in *Climbing and Walking Robots*, Springer, 2006, pp. 869-874.

[42] M. Armada, M. Prieto, T. Akinfiev, R. Fernandez, P. Gonzalez, E. Garcia, H. Montes, S. Nabulsi, R. Ponticelli and J. Sarria, "On the Design and Development of Climbing and Walking Robots for the Maritime Industries," *Journal on Maritime Research,* vol. 2, no. 1, pp. 9-32, 2005.

[43] V. Gradetsky and M. Knyazkov, "Multi-functional Wall Climbing Robot," in *International Conference on Climbing and Walking Robots (CLAWAR),* Baltimore, 2012.

[44] J. Shang, T. Sattar, S. Chen and B. Bridge, "Design of A Climbing Robot for Inspecting Aircraft Wings and Fuselage," in *International Conference on Climbing and Walking Robots (CLAWAR),* Brussels, 2006.

[45] B. Luk, T. White, D. Cooke, N. Hewer, G. Hazel and S. Chen, "Climbing Service Robot for Duct Inspection and Maintenance Applications in a Nuclear Reactor," in *International Symposium on Robotics,* Munich, 2001.

[46] "Cleaning Robots for Large Area Glass Facades on Buildings," Serbot AG, Buochs, Switzerland, 2015.

[47] L. Guido, M. Michele, M. Giovanni and R. Sinatrac, "A Low-cost Lightweight Climbing Robot for the Inspection of Vertical Surfaces," *Journal of Mechatronics,* vol. 12, no. 1, pp. 71-96, 2002.

[48] C. Hyoukryeol, P. Jaejun and K. Taehun, "A Self-contained Wall Climbing Robot With Closed Link Mechanism," *Journal of Mechanical Science and Technology,* vol. 18, no. 4, pp. 573-581, 2004.

[49] S. Ryu, J. Park, S. Ryew and H. Choi, "A Self-contained Wall Climbing Robot With Closed Link Mechanism," in *International Conference on Intelligent Robots and Systems,* Miami, 2001.

[50] D. Longo and G. Muscato, "Design and Control Methodologies for the Climbing Robot Alicia II," in *International conference on Climbing and Walking Robots (CLAWAR)*, Paris, 2002.

[51] H. Schempf, "Neptune: Above Ground Storage Tank Inspection Robot System," in *IEEE International Conference on Robotics and Automation*, San Diego, 1994.

[52] Y. Yoshida and S. Ma, "Design of A Wall-climbing Robot with Passive Suction Cups," in *International Conference on Robotics and Biomimetics*, Tianjin, 2010.

[53] S. Tso, J. Zhu and B. Luk, "Prototype Design of A Light-weight Climbing Robot Capable of Continuous Motion," in *International Conference on Mechatronics and Machine Vision*, Hong Kong, 2001.

[54] W. Fischer, G. Caprari, R. Siegwart and R. Moser, "Compact Climbing Robot Rolling on Flexible Magnetic Rollers, for Generator Inspection With The Rotor Still Installed," in *International Conference on Climbing and Walking Robots (CLAWAR)*, Paris, 2011.

[55] J. Zhu, D. Sun and S. Tso, "Development of A Tracked Climbing Robot," *Journal of Intelligent and Robotic Systems,* vol. 34, no. 4, pp. 427-443, 2002.

[56] H. Kim, D. Kim, H. Yang, K. Lee, K. Seo, D. Chang and J. Kim, "A Wall Climbing Robot with Vacuum Caterpillar Wheel System Operated by Mechanical Valve," in *International Conference on Climbing and Walking Robots (CLAWAR),* Brussels, 2006.

[57] S. Tso and T. Feng, "Robot Assisted Wall Inspection for Improved Maintenance of High-Rise Buildings," in *International Symposium on Automation and Robotics in Construction*, Eindhoven, 2003.

[58] W. Wang, B. Tang, H. Zhang and G. Zong, "Robotic Cleaning System for Glass Facade of High-rise Airport Control Tower," *Industrial Robot: An International Journal,* vol. 37, no. 5, pp. 469-478, 2010.

[59] Z. Qian, Y. Zhao and Z. Fu, "Development of Wall-Climbing Robots With Sliding Suction Cups," in *IEEE/RSJ International Conference on Intelligent Robots and Systems*, Beijing, 2006.

[60] D. Longo and G. Muscato, "A Modular Approach for the Design of the Alicia3 Climbing Robot for Industrial Inspection," *Industrial Robot: An International Journal,* vol. 31, no. 2, pp. 148-158, 2004.

[61] F. Bonaccorso, C. Bruno, D. Longo and G. Muscato, "Structure and Model Identification of A Vortex Based Suction Cup," in *International Conference on Climbing and Walking Robots and the Support Technologies for Mobile Machines (CLAWAR),* Coimbra, 2008.

[62] N. Elkmann, D. Kunst, T. Krueger, M. Lucke, T. Bohme, T. Felsch and T. Sturze, "SIRIUSc: Facade Cleaning Robot for A High-Rise Building in Munich, Germany," in *International Conference on Climbing and Walking Robots (CLAWAR),* Madrid, 2004.

[63] X. Zelihang and M. Peisun, "A Wall Climbing Robot for Labeling Scale of Oil Tank's Volume," *Robotica: Cambridge Journals,* vol. 20, no. 2, pp. 209-212, 2002.

[64] J. Shang, B. Bridge, T. Sattar, S. Mondal and A. Brenner, "Development of a climbing robot for inspection of long weld lines," *Industrial Robots: An International Journal,* vol. 35, no. 3, pp. 217-223, 2008.

[65] P. Kalra, G. Jason and M. Max, "A Wall Climbing Robot for Oil Tank Inspection," in *IEEE International Conference on Robotics and Biomimetics*, Kunming, 2006.

[66] Y. Zhang and T. Dodd, "Design and Optimization of Magnetic Wheel for Wall and Ceiling Climbing Robot," in *International Conference on Mechatronics and Automation*, Xi'an, 2010.

[67] F. Tache, F. Pomerleau, W. Fischer and G. Caprari, "MagneBike: Compact Magnetic Wheeled Robot for Power Plant Inspection," in *International Conference on Applied Robotics for the Power Industry (CARPI),* Montreal, 2010.

[68] M. Wu, G. Pan, T. Zhang, S. Chen, F. Zhuang and Z. Yan, "Design and Optimal Research of a Non Contact Adjustable Magnetc Adhesion Mechanism for a Wall Climbing Welding Robot," *International Journal of Advanced Robotic Systems,* vol. 10, no. 1, 2013.

[69] D. Longo, D. Elettrico and M. Giovanni, "SCID: A Non-Actuated Robot for Wall Exploration," in *IEEE/ASME International Conference on Advanced Intelligent Mechatronics*, Como, 2001.

[70] T. Akinfiev, M. Armada, M. Prieto and M. Uquillas, "Concerning a Technique for Increasing Stability of Climbing Robots," *Journal of Intelligent and Robotic Systems,* vol. 27, no. 1, pp. 195-209, 2000.

[71] B. Luk, A. Collie, D. Cooke and S. Chen, "Walking and Climbing Service Robots for Safety Inspection of Nuclear Reactor Pressure Vessels," in *Asia Pacific Conference on Risk Management and Safety*, Hong Kong, 2005.

[72] H. Kim, D. Kim, H. Yang, K. Lee, K. Seo, D. Chang and J. Kim, "Development of A Wall-Climbing Robot Using A Tracked Wheel Mechanism," *Journal of Mechanical Science and Technology*, vol. 22, no. 8, pp. 1940-1948, 2008.

[73] A. Albagul, A. Asseni1 and O. Khalifa, "Wall Climbing Robot: Mechanical Design and Implementation," in *WSEAS International Conference on Circuits, Systems, Signal and Telecommunications*, Mexico City, 2011.

[74] T. Miyake, H. Ishihara and M. Yoshimura, "Basic Studies on Wet Adhesion System for Wall Climbing Robots," in *International Conference on Intelligent Robots and Systems (IROS)*, San Diego, 2007.

[75] J. Li, G. Xueshan, N. Fan, K. Li and Z. Jiang, "BIT Climber: A Centrifugal Impeller-Based Wall Climbing Robot," in *International Conference on Mechatronics and Automation*, Changchun, 2009.

[76] F. Manuel and T. J., A Survey of Technologies and Applications for Climbing Robots Locomotion and Adhesion, ISBN: 978-953-307-030-8: InTech, 2010.

[77] M. Elliot, W. Morris and J. Xiao, "City-climber: A New Generation of Wall-Climbing Robots," in *IEEE International Conference on Robotics and Automation*, Florida, 2006.

[78] T. Bretl, S. Rock, J. Latombe, B. Kennedy and H. Aghazarian, "Free-Climbing With A Multi-Use Robot," in *International Symposium on Experimental Robotics*, Singapore City, 2004.

[79] M. Spenko, G. Haynes, J. Saunders, M. Cutkosky and A. Rizzi, "Biologically inspired climbing with hexapedal Robot," *Journal of Field Robotics*, vol. 25, p. 4, 2008.

[80] S. Avishi, A. Tomer and S. Amir, "Design and Motion Planning of An Autonomous Climbing Robot With Claws," *Journal of Robotics and Autonomous System*, vol. 59, pp. 1008-1019, 2011.

[81] S. Jensen-Segal, W. Virost and R. Provancher, "ROCR: Energy Efficient Vertical Wall Climbing With A Pendular Two-Link Mass-Shifting Robot," in *International Conference on Robotics and Automation*, California, 2008.

[82] H. Prahlad, M. John, S. Scott, R. Pelrine and R. Kornbluh, "Electroadhesive Robots— Wall Climbing Robots Enabled by a Novel, Robust, and Electrically Controllable Adhesion Technology," in *International Conference on Robotics and Automation (ICRA)*, Pasadena, 2008.

[83] G. Cui, K. Liang, J. Guo, H. Li and D. Gu, "Design of a Climbing Robot Based on Electrically Controllable Adhesion Technology," in *International Conference on Solid State and Materials (ICSSM)*, Kyoto, 2012.

[84] D. Fanella, "Design of Low-Rise Reinforced Concrete Buildings Based on 2009 IBC," in *ASCE/SEI 7–05, ACI 318–08. International Code Council*, Washington DC, 2009.

[85] R. Charles, C. James and T. Anthony, Reinforced Concrete Designer's Handbook, Eleventh Edition, ISBN: 9780419258308: Taylor and Francis Group, 2007.

[86] M. Khan, "Detecting Corrosion Induced Delaminations," *Concrete International*, vol. 7, pp. 73-78, 2003.

[87] "Design of Concrete Structures, General Rules," Eurocode 2, European Standard, 2004.

[88] R. Clarke, "Magnetic Properties of Materials," University of Surrey, Surrey, 2008.

[89] E. Trautmann, L. Ray and J. Lever, "Development of An Autonomou Robot for Ground Penetrating Radar Surveys of Polar Ice," in *International Conference on Intelligent Robots and Systems*, St. Louis, 2009.

[90] M. Nakhkash and R. Mohammad, "Water Leak Detection Using Ground Penetrating Radar," in *International Conference on Ground Penetrating Radal*, Delft, 2004.

[91] "IDS RIS Hi-Bright Ground Penetrating Radar for bridge condition assessment in Washington DC," The National Academies of Sciences, Engineering, and Medicine, Washington DC, 2013.

[92] C. Ekes and B. Neducza, “Robot Mounted GPR for Pipe Inspection,” in *International Conference on Ground Penetrating Radar (GPR)*, Shanghai, 2012.

[93] M. W. Rebecca, R. E. Laura, L. H. James and B. M. Amy, “Crevasse Detection in Ice Sheets Using Ground Penetrating Radar and Machine Learning,” *IEEE Journal of Selected Topics in Applied Earth Observations and Remote Sensing,* vol. 7, no. 12, pp. 4836-4848, 2014.

[94] B. Zhiqiang, G. Yisheng, C. Shizhong, Z. Haifei and Z. Hong, “A Miniature Biped Wall-Climbing Robot for Inspection of Magnetic Metal Surfaces,” in *IEEE International Conference on Robotics and Biomimetics*, Guangzhou, 2012.

[95] A. Annan, Ground Penetrating Radar Principles, Procedures and Applications, Canada: Sensors & Software Inc, 2003.

[96] M. Lambert, M. Surhone and S. Timpledon, Snell's Law: Optics, Physics, Angle of Incidence, Refraction, Isotropy, Metamaterial, Refractive Index, Willebrord Snellius, Velocity, Ptolemy, Thebaid, ISBN - 6130315171: Betascript Publishing, 2010.

[97] D. Wright, S. Hodge, J. Bradley, T. Grover and R. Jacobel, “Instruments and Methods; A Digital Low-frequency Surface-profiling Ice Radar System,” *Journal of Glaciology,* vol. 36, no. 122, pp. 112-121, 1990.

[98] Y. Xuelin, D. Zhenjie, H. Qingsong, Y. Jianguo, Z. Bo and H. Long, “High-Repetition and -Stability All-Solid State Pulsers Based on Avalanche Transistor Marx Circuit,” in *International Conference on Microwave and Millimeter Wave Technology*, Chengdu, 2010.

[99] P. W. Smith, Transient Electronics: Pulsed Circuit Technology, New York: John Wiley & Sons, 2002.

[100] X. Xinfan, L. Lihua, Y. Shengbo, G. Hongfei and F. Guangyou, “A Novel Sub-nanosecond Monocycle Pulse Generator for UWB Radar Applications,” *Journal of Sensors,* vol. 2014, p. 4, 2014.

[101] W. Qing, T. Xiaojian, L. Yang, L. B. Li and G. Bo, “Design of an Ultra-Wideband Pulse Generator Based on Avalanche Transistor,” in *International Conference on Wireless Communications, Networking and Mobile Computing*, Dalian, 2008.

[102] I. Merrill, “An Introduction To Impulse Radar,” Naval Research Laboratory, Washington, 1990.

[103] A. Yarovoy and L. Lighart, “Ultra-Wideband Antennas for Ground Penetrating Radar,” International Research Center for Telecommunications-Transmision and Radar, Delft University of Technology, 2003.

[104] A. Yarovoy, P. Aubrey and L. Lighart, “GPR Antenna Measurements in Time Domain,” nternational Research Center for Telecommunications-Transmision and Radar, Delft University of Technology, 2003.

[105] T. Wu and R. King, “The Cylindrical Antenna With Nonreflecting Resistive Antenna,” *IEEE Transactions on Antennas and Propagation,* vol. 13, no. 3, pp. 369-373, 1995.

[106] L. Roger and D. Jeffrey, “Modeling Near-field GPR in Three Dimensions Using The FDTD Method,” *Journal of Geophysics,* vol. 62, no. 4, pp. 1114-1126, 1997.

[107] L. Andrian, A. Yarovoy and L. Ligthart, “RC-loaded Bow-tie Antenna for Improved Pulse Radiation,” *IEEE Transactions on Antennas and Propagation,* vol. 52, no. 10, pp. 2555-2563, 2004.

[108] M. Ghuang and J. Kang, “A Printed Dipole Antenna With Tapered Slot Feed For Ultrawideband Applications,” *IEEE Transactions on Antennas and Propagation,* vol. 53, no. 11, pp. 3833-3836, 2005.

[109] T. Ahmet, A. Keskin, M. Senturk, A. Magat, M. Ozakin and S. Aksoy, “Ultra Wide Band TEM Horn and Reflector Antenna Designs for Down and Forward Looking Ground Penetrating Radars,” in *International Workshop on Advanced Ground Penetrating Radar*, Nantes, 2013.

[110] M. Nagatoshi, H. Morishita and S. Tanaka, "A Study on an Improvement of Folded Bow-Tie Antenna by Adding Aditional Elements," in *IEEE International Symposium on Antennas and Propagation (APSURSI)*, Washington, 2011.

[111] J. Choi, F. Dagefu, B. Sadler and K. Sarabandi, "Electrically Small Folded Dipole Antenna for HF and Low-VHF Bands," *IEEE Antennas and Wireless Propagation Letters,* vol. 15, no. 99, p. 1, 2015.

[112] P. Patel, K. Dwibedi, R. Poonkhuzhali and D. Thiripurasundari, "Miniaturized Dipole Antenna using Koch Fractal Technique for Wearable Application," in *International Conference on Communication and Signal Processing*, Melmaruvathur, 2013.

[113] J. Kim, M. Nagatoshi and H. Morishita, "Study on Miniaturization of A Strip Folded Dipole Antenna with Two Linear Conductors," in *European Conference on Antennas and Propagation (EUCAP)*, Rome, 2001.

[114] M. Nagatoshi, S. Tanaka, S. Horiuchi and H. Morishita, "A Study on Wider Bandwidth of Bow-Tie Antenna with Folded Elements," in *IEEE Antennas and Propagation Society International Symposium (APSURSI)*, Toronto, 2010.

[115] H. Morishita and N. T. Hung, "Characteristics of Antennas with Folded Structure," in *International Symposium on Antennas and Propagation (ISAP)*, Nagoys, 2012.

[116] W. S. Yeoh, K. L. Wong and W. S. T. Rowe, "Wideband Miniaturized Half Bowtie Printed Dipole Antenna with Integrated Balun for Wireless Applications," *IEEE Transactions on Antennas AND Propagation,* vol. 59, no. 1, pp. 339-342, 2011.

[117] Y. Liu, H. Yi, W. Wang and X. Gong, "A Novel Miniaturized Broadband Dual-Polarized Dipole Antenna for Base Station," *IEEE Antennas and Wireless Propagation Letters,* vol. 12, pp. 1335-1338, 2013.

[118] A. Hamani, R. Touhami and M. Yagoub, "Novel Tag Antenna Design for UHF RFID Applications," in *13th Mediterranean Microwave Symposium (MMS)*, Saida, 2013.

[119] Y. Lin, C. Lin, H. Chen and J. Peng, "Compact Dipole Antenna for Implantable Devices," in *International Symposium on Antennas and Propagation (ISAP)*, Kaohsiung, 2014.

[120] M. Riahi and A. Tavangar, "Prognosis of the Effects of Soil Characteristics on the Performance of Landmine Detection in Ground-Penetrating Radar System - A Case Study," in *International Conference on Technical Inspection and NDT*, Tehran, 2008.

[121] C. Colla, D. McCann and M. Forde, "Radar testing of a masonry composite structure with sand and water backfill," *Journal of Bridge Engineering,* vol. 6, no. 4, pp. 262-270, 2001.

[122] N. Diamanti, A. Giannopoulos and M. C. Forde, "Numerical modelling and experimental verification of GPR to investigate ring separation in brick masonry arch bridges," *NDT & E International,* vol. 41, no. 5, pp. 354-363, 2008.

[123] T. Bergmann and K. Holliger, "Numerical modeling of borehole georadar data," *Journal of Geophysics,* vol. 67, no. 4, pp. 1249-1257, 2002.

[124] A. Benedetto, "Water content evaluation in unsaturated soil using GPR signal analysis in the frequency domain," *Journal of Applied Geophysics,* vol. 71, no. 1, pp. 26-35, 2010.

[125] C. Balanis, Antenna theory: analysis and design, New York: John Wiley and Sons, Inc., 2005.

[126] J. Jin, The Finite Element Method in Electromagnetics, 2 ed., Wiley-IEEE Press, 2002.

[127] L. Seyfi and E. Yaldz, "A simulator based on energy-efficient GPR algorithm modified for the scanning of all types of regions," *Turkish Journal of Electrical Engineering and Computer Sciences,* vol. 20, no. 3, pp. 381-389, 2010.

[128] A. Sawitzki, "Electromagnetic modelling of surfaces using method of moments with calculated phase mesh," *IET Journal of Microwaves, Antennas & Propagation,* vol. 9, no. 12, p. 1354–1362, 2015.

[129] K. Aberegg and A. Peterson, “Application of the integral equation-asymptotic phase method to two-dimensional scattering,” *IEEE Transactions on Antennas and Propagations,* vol. 43, no. 5, p. 534–537, 1995.

[130] K. Chandrashekar and V. Girish, “Analysis of Electromagnetic Wave Propagation at Discontinuities for Different Dielectric Waveguide Geometries Using Two-Dimensional FEM,” in *International Conference on Trends in Automation, Communications and Computing Technology,* Bangalore, 2015.

[131] A. Lamecki, L. Balewski and M. Mrozowski, “Effect of mesh deformation on the accuracy of 3D FEM electromagnetic analysis,” in *IEEE MTT-S International Conference on Numerical Electromagnetic and Multiphysics Modeling and Optimization*, Beijng, 2016.

[132] D. Uduwawala, M. Norgren and P. Fuks, “A Complete Fdtd Simulation Of A Real Gpr Antenna System Operating Above Lossy And Dispersive Grounds,” *Progress In Electromagnetics Research,* vol. 50, p. 209–229, 2005.

[133] J. Hebert, T. Holzer and T. Eveleigh, “Computer Modeling and Simulation of Ground Penetrating Radar using Finite Difference Time Domain Code,” in *International Conference on Modeling, Simulation and Visualization Methods (MSV),* Athens, 2012.

[134] N. Nanthini and V. Ramanathan, “Electromagnetic Field Propagation Analysis in Free Space Using Finite Difference Time Domain Method (FDTD),” *International Journal of Innovative Research in Computer and Communication Engineering,* vol. 3, no. 1, pp. 144-151, 2015.

[135] Y. Vives, C. Arcambal, A. Louis, F. Daran, P. Eudeline and B. Mazari, “Modeling magnetic radiations of electronic circuits using near-field scanning method,” *IEEE Transactions on Electromagnetic Compatibility,* vol. 49, no. 2, pp. 391-399, 2007.

[136] Y. Liang and E. Li, “A systematic coupled approach for EM susceptibility analysis of a shielded device with multilayer circuits,” *IEEE Transactions on Electromagnetic Compatibility,* vol. 47, no. 4, 2005.

[137] Y. Gotoh and Y. Ishida, “Evaluation of Electromagnetic Inspection of Outer Side Defect on Small Diameter and Thick Steel Tube With Steel Support Using 3-D Nonlinear FEM,” *IEEE Transactions on Magnetics,* vol. 50, no. 11, pp. 1-6, 2014.

[138] S. Mohammad and N. Daniel, “Design of Linearly Polarized Rectangular Patch Antenna Using MoM, FDTD and FEM,” in *International Symposium of Antennas and Propagation Society*, Honolulu, 2007.

[139] M. Lai-Ching, “Implementation of Parallelized Finite Difference Time Domain (FDTD) Algorithm and Its Application To The Modeling of Metamaterials,” The Pennsylvania State University, Pennsylvania, 2008.

[140] K. Yee, “Numerical Solution of Initial Boundary Value Problems Involving Maxwell's Equations in Isotropic Media,” *IEEE Transactions on Microwave Theory and Techniques,* vol. 44, no. 3, pp. 61-69, 1998.

[141] D. M. Sullivan, Electromagnetic simulation using the FDTD method, New Jersey: John Wiley & Sons, 2013.

[142] G. Fang and P. Michele, “Designing of A Low Frequency Ultra Wideband(UWB) Antenna And Its Application In Ground Penetrating Radar(GPR) System,” in *10th International Conference on Ground Penetrating Radar,* The Netherlands, 2004.

[143] I. Trinks, P. Tsourlos, K. Löcker, G. Vargemezis, G. Tsokas, A. Vlachopoulos, C. Doumas, M. Kucera and G. Verhoeven, “Near Surface Geophysical Archaeological Prospection at the Prehistoric Site of Akrotiri on Santorini/Thera,” in *20th European Meeting of Environmental and Engineering Geophysics* , Athens, 2014.

[144] T. Xia, A. Venkatachalam and D. Huston, "A High Performance Low-ringing Ultra-wideband Monocycle Pulse Generator," *IEEE Transactions on Instrumentation and Measurement,* vol. 61, no. 1, pp. 216-266, 2012.

[145] D. Rao, G. Singh, A. De and B. Sahoo, "A Tuneable CMOS Pulse Generator for Detecting The Cracks in Concrete Walls," in *IEEE Computer Society Annual Symposium on VLSI*, Massachusetts, 2012.

[146] W. Liu and W. Hao, "The Research of Ultra-wideband Narrow Pulse Circuit Based On Avalanche Effect Theory," in *Chinese Control Conference*, Beijing, 2010.

[147] L. Xiao-han, S. Guo-bin, L. Jian-sheng and L. Zheng, "Research On High-peak and Narrow-width Pulsed Driving Circuit of LD," *Journal of Piezoelectrics & Acoustooptics,* vol. 22, no. 6, pp. 414-417, 2000.

[148] A. Saleh and R. Valenzuela, "A Statistical Model for Indoor Multipath Propagation," *IEEE Journal on Selected Areas in Communications,* vol. 5, no. 2, pp. 128-137, 2003.

[149] S. International, "Electroadhesive Robots for Robust Vertical Mobility," California, 2011.

[150] P. Sekhar and R. Bhooshan, "Duct Fan Based Wall Climbing Robot for Concrete Surface Crack Inspection," in *IEEE India Conference,* Pune, 2014.

[151] X. Haolu, W. Xin, A.Wang, Z. Bin and Z. Yumei, "A Varying Pulse Width 5th-Derivative Gaussian Pulse Generator for UWB Transceivers in CMOS," in *IEEE Radio and Wireless Symposium*, Orlando, 2008.

[152] P. Tuan-Anh, V. Krizhanovskii, H. Seok and L. Sang, "4.7pJ/pulse 7th Derivative Gaussian Pulse Generator for Impulse Radio UWB," in *IEEE International Symposium on Circuits and Systems*, California, 2007.

[153] Z. Low, J. Cheong and C. Law, "Novel Low Cost Higher Order Derivitive Gaussian Pulse Generator Circuit," in *International Conference on Communications Systems,* Singapore, 2004.

[154] X. Xinfan, L. Lihua, Y. Shengbo, G. Hongfei and F. Guangyou, "A Novel Sub-Nanosecond Monocycle Pulse Generator for UWB Radar Applications," *Journal of Sensors,* vol. 2014, no. 149, pp. 22-31, 2014.

[155] M. Nagatoshi, H. Morishita and S. Tanaka, "A Study on an Improvement of Folded Bow-Tie Antenna by Adding Aditional Elements," in *IEEE International Symposium on Antennas and Propagation (APSURSI)*, Washington, 2011.

[156] S. Radiom, A. Enayati, G. Vandenbosch, W. Raedt and G. Gielen, "Miniaturization of a Bow-Tie Antenna for A PulsedUWB Transceiver in The 300–960 MHz Band," in *3rd European Conference on Antennas and Propagation*, Berlin, 2009.